Microfluidic Engineering of Water Purification

by

Siwon Choi

B.S. & MChE Chemical Engineering
Carnegie Mellon University

SUBMITTED TO THE DEPARTMENT OF CHEMICAL ENGINEERING IN PARTIAL FULFILLMENT OF THE REQUIREMENTS FOR THE DEGREE OF

Doctor of Philosophy

AT THE
MASSACHUSETTS INSTITUTE OF TECHNOLOGY

June 2017

Signature redacted

Signature of Author: .....
Department of Chemical Engineering
May 23rd, 2017

Signature redacted

Certified by: .....
Jongyoon Han
Professor of Electrical Engineering and Computer Science
Professor of Biological Engineering
Thesis Supervisor

Signature redacted

Certified by: .....
Karen K. Gleason
Professor of Chemical Engineering
Thesis Supervisor

Signature redacted

Accepted by: .....
Daniel Blankschtein
Professor of Chemical Engineering
Chairman, Committee for Graduate Students

Microfluidic Engineering of Water Purification

by

Siwon Choi

SUBMITTED TO THE DEPARTMENT OF CHEMICAL ENGINEERING
ON MAY 23rd, 2017 IN PARTIAL FULFILLMENT OF THE REQUIREMENTS FOR THE DEGREE OF

Doctor of Philosophy in Chemical Engineering

ABSTRACT

The demand for clean water has been increasing for several reasons, such as rapid industrialization of developing countries, environmental pollution and climate change, and development of biofuels and the resulting irrigation growth. To meet the needs for this growing demand for clean water, desalination has become an appealing solution as saline water (brackish water, seawater and brine) are the most abundant water source for most of the world. However, desalination is energy and capital intensive compared to other water treatment processes, and oftentimes it is not economically feasible. Current desalination technologies require further engineering and development to become more sustainable in the long term. My Ph.D thesis is focused on engineering of electromembrane desalination, which is a set of electrically driven desalination technologies that utilize ion transport through ion exchange membranes. We employed microfluidic platforms and numerical modeling tools for the study, for they help reveal novel insights regarding the micro-scale details that are difficult to be discovered from the conventional large-scale systems.

In this thesis, we consider three topics: i) engineering of structures that enhance mass transport in electrodialyis (ED), ii) techno-economic analysis of ion concentration polarization (ICP) desalination for high salinity brine treatment, and iii) development of electrocoagulation (EC) – ion concentration polarization (ICP) desalination hybrid that removes dissolved ions and non-ionic contaminants from water in a single device.

First, we employed an electrodialysis (ED) system as a model to investigate the mass transport effects of embedded microstructures, also known as spacers, in electromembrane desalination systems. The spacer engineering is especially critical for low salinity (*i.e.*, brackish water) desalination, where the mass transport in the solution is a dominant contributor to the electrical energy consumption in the system. Parametric studies of the spacer design revealed that small cylindrical structures effectively re-distribute the local flow velocity and enhance mass transport in the system. Furthermore, we found that relative diffusivities of cation and anion in the solution should be considered in designing the spacer and that the optimal design should

maximize the mass transport while keeping the effect on the hydrodynamic resistance small. Next, we built an empirical model to estimate an electrical energy consumption of ICP desalination and utilized it to obtain the water cost and optimal operating parameters for high salinity applications. We performed cost analyses on two specific cases (*i.e.*, partial desalination of high salinity brine to the seawater level, and brine concentration for salt production) and compared the performance with mainstream desalination technologies for each application. Lastly, we combined two electrical water treatment technologies and created an EC-ICP hybrid for total water treatment, which removes dissolved ions and non-ionic contaminants from the feed solution. We demonstrated a continuous EC-ICP operation that successfully removed salt and suspended solids. Our system is flexible in terms of the system size, and the type and concentration of contaminants it can handle, and thus it can find applications as a portable water treatment system.

Thesis Supervisor: Jongyoon Han
Title: Professor of Electrical Engineering and Computer Science and Professor of Biological Engineering

Thesis Supervisor: Karen K. Gleason
Title: Alexander and I. Michael Kasser Professor of Chemical Engineering

Acknowledgements

I would like to thank my mentors, colleagues, friends, and family. This doctoral thesis is and will be a milestone in my life that would not have been completed without their support.

First of all, I would like to thank my thesis advisors, Professor Jongyoon "Jay" Han and Professor Karen K. Gleason. Professor Han introduced me into this interesting field of desalination and microfluidics. He encouraged and inspired me to study various topics, which helped me broaden my research experience and knowledge in the field of water purification. I greatly appreciate that he has always been supportive of my study, as well as my decisions regarding the career and future plans, and shared his insightful thoughts. Professor Gleason helped me to fully utilize my chemical engineering knowledge in my research. She has always been genuinely interested in my academic and personal well-being and my plans for the next step. Professor Han and Professor Gleason have become my role models for a mentor, a leader, and a researcher. I sincerely appreciate all their support and guidance throughout my study.

I would like to thank my committee members, Professor Fikile R. Brushett and Professor Bader Al-Anzi. Professor Brushett challenged me with very interesting questions and helped me to relate my study in a larger context. Professor Al-Anzi helped me understand the field of desalination and ensured that my research is applicable and beneficial to the actual desalination practice. Professor Brushett and Professor Al-Anzi's expertise in the different fields enriched my thesis.

I thank the current and past Han and Gleason group members. I would like to express special thanks to Dr. Bumjoo Kim, Prof. Van Sang Pham, Prof. Yong-Ak Song, Dr. Rhokyun Kwak, Dr. Aniruddh Sarker, Dr. Sha Huang, Dr. Lidan Wu, Dr. Han Wei Hou, Dr. Sung Hee Ko,

Prof. Majid Ebrahimi Warkiani, Taehong Kwon, Debbie Yu, Hyuckjin Kwon, Rho Jun Toh, Dr. Tengyang Jing, Wei Ouyang, Dr. Israel Martinez, Kyungyong Choi, Matt Flavin, Dr. Minseok Kim, Dr. Hyunryul Ryu, Dr. Chenhui Peng, and Dr. Junghyo Yoon from Han Group and Prof. Rong Yang, Priya Moni, Dr. Minghui Wang, Dr. Do Han Kim, Dr. Hossein Sojoudi, Dr. Nan Chen, Dr. Amelia Servi, Andong Liu, Xioxue Wang, Dr. Won Jun Jo, Prof. Reeja Jayan, and Prof. Sunghwan Lee from Gleason Group for the intellectually stimulating discussions and the friendship.

I am also thankful for my classmates and friends who have supported me through my study and made my life here at MIT so much enjoyable. In particular, I thank my friends in KSACE, especially Jiyoung Ahn, Jae Jung Kim, Dr. Jinyoung Baek, Prof. Hyomin Lee, Dr. Yongwoo Son, Dr. Jouha Min, Juhyun Song, Myung Sun Kang, and Minkyung Park, and my chemical engineering classmates, especially Dr. Nop Weeranoppanant, Dr. Lisi Xie, and Lionel Lam. I thank my friends Dr. Minae Ouk, Dr. Sohyun Park, Nam Joo Kim, Dr. Han Kyul Joo, Dr. Alan Gyehyun Kim, Joohyun Seo, Anna Lee, Dongkwan Kim, Junghyun Lee, Sucheol Shin, Jaehwan Kim, Ingon Lee, Dr. Donghun Kim, Jongwoo Lee, and Sangjun Lee.

Lastly, I am grateful for the unconditional love and support and prayer from my parents Hyeon Gwon Choi and Jin Sook Shin, my brother Seong Won Choi, and my aunt Hyunjoo Choi. I especially thank my grandfather who always prayed for me and had looked forward to coming to my graduation but passed away in 2016, and I dedicate this thesis to the memory of my grandfather. And I thank God for looking over me in every step of my life.

This thesis is dedicated to the memory of my beloved grandfarther,
Bok Sool Choi (1927-2016).

TABLE OF CONTENTS

LIST OF FIGURES

LIST OF TABLES

1. INTRODUCTION

1.1 Overview of desalination

1.1.1 Growing need for clean water

Securing supply of clean water is progressively becoming challenging for several reasons. Emerging economy in many countries increases water use per person as a result of rapid industrialization without appropriate wastewater treatment system[1]. According to World Health Organization, more than 2.5 billion people (about 40% of the population) do not have a proper sewer sanitation system[2]. Growing pollution and the climate change also reduce fresh water availability[1,3]. As the energy paradigm shifts to biofuels, demand for irrigation water for crops may increase[4]. To resolve this growing demand for clean water, desalination is an appealing solution as saline water (brackish water, seawater and brine) are the most abundant water source for most of the world, composing 97.5% of the total water on earth[5]. It is projected that by 2050, the required desalination capacity would reach one billion cubic meter per day[6] as the newly contracted capacity of desalination plants is forecasted to grow over the next few decades [7].

However, the challenge is the high cost for desalination, which often renders it economically infeasible. With this growing demand for clean water, the current desalination methods are not sustainable in the long term. Therefore, it is imperative to develop an alternative desalination technology, with improved energy and cost efficiency, simple deployment and operation, and environmental sustainability.

1.1.2 Desalination performance indicators

There are several performance indicators to consider when assessing desalination technologies. Here, we explain the salt removal ratio, recovery ratio, specific energy consumption, and specific water cost. These terms will be used throughout the thesis to discuss the performance of various desalination technologies.

Salt removal ratio (SRR), or "salt removal" for short, represents how much salt is removed from the diluate stream (*i.e.*, product). A higher SRR indicates a purer product stream for a given feed.

$$SRR = \frac{C_{feed} - C_{diluate}}{C_{feed}}$$

where C_{feed} and $C_{diluate}$ represent the feed and the diluate concentrations, respectively.

Recovery ratio (RR), or "recovery" for short, represents the ratio of the product volume to the feed volume. RR is expressed with volumetric flowrate for a continuous process and with solution volume for a batch process. The product is usually desalinated water, but it can be the concentrated stream in some cases, such as a brine concentration process. A high recovery is favorable because it indicates more useful water is produced for a given feed.

$$RR = \frac{Q_{product}}{Q_{feed}} = \frac{V_{product}}{V_{feed}}$$

where Q_{feed} and $Q_{diluate}$ represent the volumetric flowrate of the feed and the product, respectively, and V_{feed} and $V_{product}$ represent the volume of the feed and the product, respectively.

Specific energy consumption, or "energy consumption" for short, is the energy required to obtain a unit volume of product water. The energy here can be in the form of thermal or electrical energy or both, depending on the desalination technology. In this thesis, the energy consumption will be expressed as kilo-Watt-hour per cubic meter of product water (kWh/m^3).

Specific water cost, or "water cost" for short, is the cost to produce a unit volume of product water. The total water cost accounts for the capital and the operating costs. Since choice of desalination technology is mainly a cost-driven decision, specific water cost is the most important metric to evaluate the economic feasibility of a desalination technology. In this thesis, the water cost will be expressed as U.S. dollar per cubic meter of product water ($\$/m^3$).

1.1.3 Current desalination technologies

Water treatment process is divided into desalination and pre/post-treatment of desalination to remove particles, chemicals, and other potential contaminants that can potentially hinder the desalination process. In this section, well-established desalination technologies that are currently used in the desalination market are briefly reviewed. Desalination technologies are largely categorized into two types: thermal and membrane technologies.

The basic principle of thermal desalination is vaporization of water from a saline solution by the use of thermal energy and condensation to obtain freshwater. The main thermal desalination technologies are multi-stage flash (MSF) and multi-effect distillation (MED). The thermal technologies were developed before membrane desalination, and they dominated the desalination market until 2000, after which membrane desalination, namely reverse osmosis, had surpassed their capacity[8]. The advantages of thermal desalination are that its energy consumption is relatively insensitive to the feed water salinity and the product water contains

very low amount of TDS. In addition, it requires less rigorous pretreatment, compared to membrane desalination, although the process suffers from scaling. However, thermal desalination is generally energy-intensive (18 – 30 kWh/m^3 for MSF and 8 – 12 kWh/m^3 for MED[9,10]), and requires high-grade thermal energy. Because thermal desalination requires low-pressure steam, the plants are usually built adjacent to power plants[11]. The technology has significant economy of scale, therefore the plants are generally large and thus immobile, and the capital investment is high.

Membrane desalination uses membrane as a physical barrier to separate dissolved ions from saline water under various driving forces, such as pressure difference and electrical/chemical potential. Reverse osmosis and electrodialysis are two commercially available membrane desalination technologies. Electrodialysis is an electrically driven membrane desalination technology and will be discussed in detail in Section 1.2. Reverse osmosis (RO), in which pressure is applied to drive water transport from the saline feed to the fresh permeate, is the state-of-the-art technology for desalination of brackish and seawater and constitutes over 60% of the current desalination industry[12]. RO enjoys low energy consumption (0.13 – 0.79 kWh/m^3 for brackish water RO[11] and >1.8 kWh/m^3 for seawater RO[13]), compared to thermal desalination. Although it is an energy and cost efficient process, RO desalination is limited to the feed salinity around the seawater level because a large concentration difference between the feed and the product leads to a large pressure drop that cannot be tolerated by the membrane[8,14]. RO systems are modular in design and thus scalable and can be mobile[11]. Because a large pressure is applied across the RO membrane, the membrane is prone to fouling, so an extensive pretreatment must precede RO, raising the total water cost.

The technologies discussed above are plotted together in

Figure 1.1. The different desalination technologies have their unique characteristics, which can become advantageous or disadvantageous depending on the situation. There are numerous factors that can affect the water management decision and the choice of desalination technology, including economic, technological, infrastructure, and environmental/regulatory considerations. Therefore, there is not a single best desalination technology; instead, ideal desalination technology will be specific to each case.

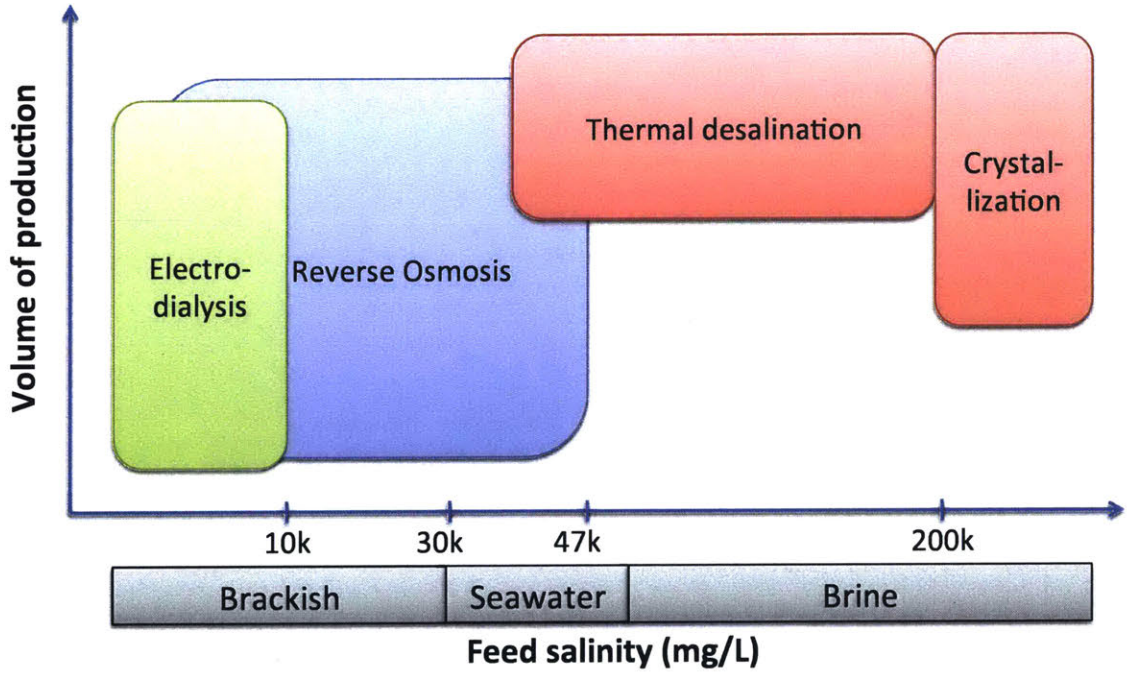

Figure 1.1 Current desalination technologies plotted with their typical feed salinity and system size.

1.2 Electromembrane desalination

Electromembrane desalination is a membrane desalination technology that utilizes selective ion transport through ion exchange membranes with electric potential as the driving force. Unlike typical membrane desalination processes, such as reverse osmosis, in which water molecules are transported through the membranes and dissolved ions are screened,

electromembrane desalination relies on transport of ions through the ion exchange membranes while water mostly remains in its original compartment. There are various types of electromembrane desalination: electrodialysis, electrodeionization, membrane capacitive deionization, and ion concentration polarization desalination. In this thesis, we will focus on electrodialysis, which is the most well-established and commercialized electromembrane technology, and ion concentration polarization desalination, which is similar to electrodialysis in construction, materials and operation.

1.2.1 Ion transport around ion exchange membranes

To explain how electromembrane desalination works, it is important to understand the ion transport around ion exchange membranes (IEMs). Ion exchange membrane is a functional material that allows selective transport of ions. IEMs are largely categorized into anion exchange membranes (AEMs) and cation exchange membranes (CEMs). Cation (anion) exchange membrane is composed of a polymer matrix with fixed negatively (positively) charged groups. As shown in Figure 1.2, mobile cations, which are referred as counter-ions, are in equilibrium with the fixed anion; mobile anions, referred as co-ions, are excluded from the membrane matrix because they have the same charge as the fixed anions. Similarly, the anion exchange membranes are preferentially permeable to anions and exclude cations. This charge-based exclusion, known as Donnan exclusion, results in the permselectivity of the ion exchange membranes[15,16].

The ion transport around the IEMs can be described mathematically with a set of governing equations. The following model assumes dilute electrolyte and no chemical reactions.

Nernst-Planck equation describes the ion transport in the electrolyte solution. The equation describes three modes for ion transport: diffusion, electro-migration, and convection.

$$\frac{\partial c_i}{\partial t} = \nabla \cdot \left(D_i \nabla c_i + M_i z_i F c_i \nabla \varphi \right) - u \cdot \nabla c_i$$

where c_i, D_i, M_i, and z_i are the concentration, diffusivity, mobility and charge number of species i, respectively, F is the Faraday's constant, φ is the electric potential, and u is the flow velocity. Poisson's equation relates the electric potential to the charge distribution in the electrolyte.

$$\nabla \cdot \left(\varepsilon \nabla \varphi \right) = \sum_i z_i F c_i = \rho_e$$

where ε is the permittivity and ρ_e is the free charge density. Navier-Stokes equation is used to describe the flow velocity profile.

$$\rho \left(\frac{\partial u}{\partial t} + u \cdot \nabla u \right) = -\nabla P + \eta \nabla^2 u - \rho_e \nabla \varphi$$

$$\nabla \cdot u = 0$$

where ρ is the fluid density, η is the fluid viscosity, and P is the static pressure. Poisson-Nernst-Planck (PNP) equations describe an electro-diffusion model in electrolyte, and the Navier-Stokes (NS) equation describes the fluid velocity profile. Combined, these equations describe an electrokinetic system. With appropriate boundary conditions, they can describe the ion transport around the ion exchange membranes as well as the bulk electrolyte[16–18].

Ion concentration polarization

The counter-ion concentration around the IEM is much different from the bulk solution due to the difference in counter-ion conductance between the bulk and the membrane. The co-ion is not conducted through the IEM, but the co-ion concentration profile follows that of the

counter-ion in order to satisfy electroneutrality. Figure 1.3 shows the concentration profile around a CEM. Because the cation (counter-ion) conductance inside the CEM is much faster than that in the bulk solution, the cation concentration on the left side (anode side) of the CEM is lower than the bulk, and the cation concentration on the right side (cathode side) is higher than the bulk. This uneven distribution of ion concentration near the interface between bulk solution and a membrane or electrode is known as concentration polarization (CP). Concentration polarization creates an ion depletion region, which has ion concentration much lower than the bulk value and thus a high electrical resistance, and results in a large electric potential drop in the system. Therefore, CP imposes a limit on ion transport; it is a major challenge in electromembrane desalination systems[16,17,19].

Current-voltage response

Current-voltage response is a characteristic of electromembrane desalination systems, such as electrodialysis and ICP desalination, and an indicator of mass transport efficiency. A typical current-voltage response has three regimes (see Figure 1.4). The first of the three is commonly known as 'Ohmic regime'[18, 28], in which the ion flux increases linearly with an increasing driving force (electric potential). As the applied voltage increases, the ions in the boundary layers are depleted faster than they are supplied from the bulk by diffusion (*i.e.*, concentration polarization); a further increase in the potential can no longer increase the ion flux, shown by the plateau region in Figure 1.4. This plateau of current due to the diffusion limit is known as the limiting regime, and the current at the transition between the Ohmic and the limiting regimes is termed limiting current. Because this limiting current indicates the limit of ion transport rate, it is used as a metric for how efficient mass transport is in electromembrane desalination systems. After the limiting regime, a further increase in the potential drop leads to a

new mode of ion transport, termed overlimiting regime, which resulted from various types of instability in the system and is evidenced by the positive slope after the plateau in the current-voltage response [15].

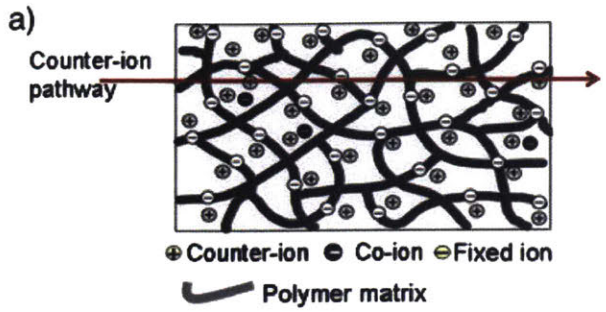

Figure 1.2 Pathway for cation (counter-ion) in cation exchange membrane (reprinted with permission from [15])

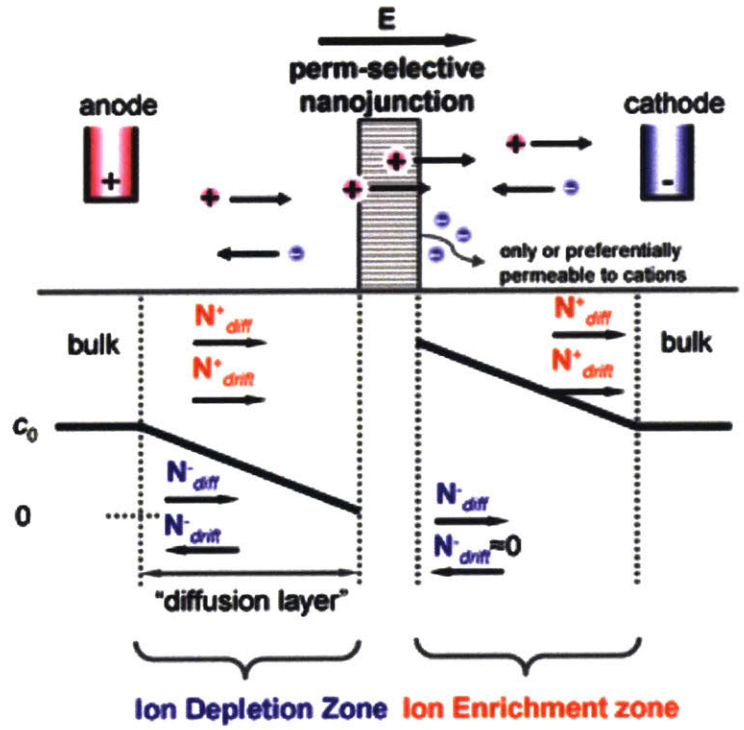

Figure 1.3 Ion concentration polarization around a cation exchange membrane (reprinted with permission from [19])

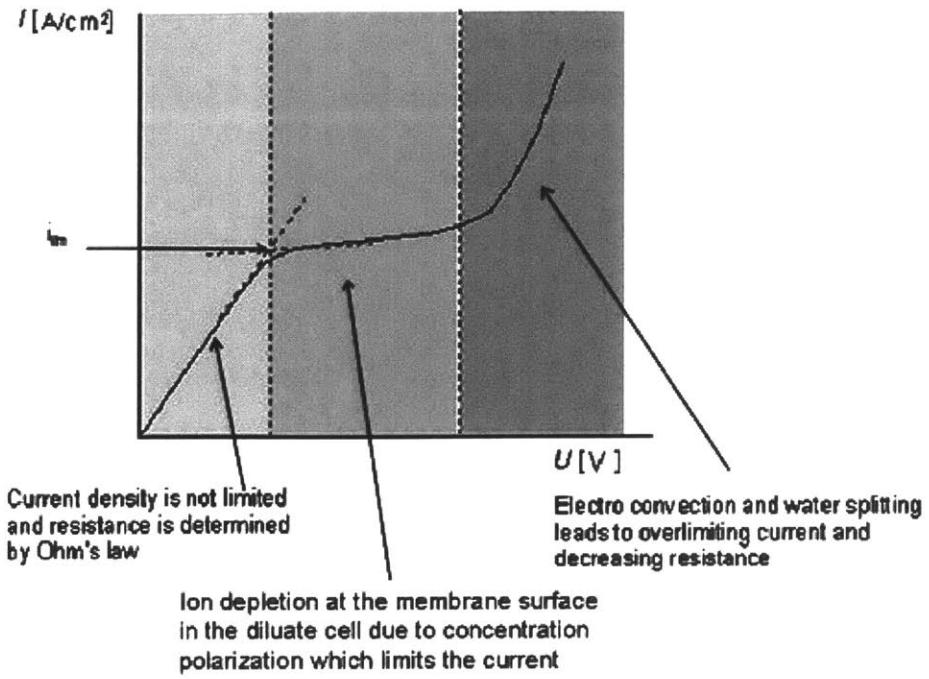

Figure 1.4 Typical current-voltage response in a system with an ion exchange membrane (reprinted with permission from [15])

1.2.2 Electrodialysis and ion concentration polarization (ICP) desalination

In electrodialysis (ED), an electrolytic cell is divided by alternating cation and anion exchange membranes, and an electric current is applied perpendicular to the flow, selective ion transport create alternating concentrate and diluate channels (Figure 1.5a). ED is a bipolar conducting system, where anions and cations both conduct the current by passing through the AEM and CEM, respectively; ion depletion zones are created on both sides of the diluate channel, reducing the total salt concentration in the channel. In ion concentration polarization (ICP) desalination, the channels are divided with identical IEMs (CEMs in Figure 1.5b). Here, we will consider an ICP desalination system with the CEMs for the following discussion. ICP desalination is a unipolar conducting system, where only cations migrate across the membranes. Because anions migrate towards the anode but cannot cross the CEM while cations travel

towards the cathode across the CEM, an ion enrichment zone forms near the CEM on the anode side (top CEM in the figure), and an ion depletion zone near the CEM on the cathode side (bottom CEM in the figure). The channels are bifurcated at the outlet to extract the desalted and concentrate streams that are recovered from the ion depletion and enrichment zones, separately [20,21].

Compared to ED, ICP desalination with CEMs inherently has a higher current efficiency, owing to the different electrical mobility of sodium and chloride ions, which are the major contributors of salinity in water. Current efficiency (CE) is defined as the ratio of the current used to remove ions to the total current applied; it can be written as

$$\mathrm{CE} = \frac{salt\ removal\ flux}{flux\ through\ membrane}$$

Since sodium and chloride ions are both monovalent, the current can be represented by flux of the ions. In ED, because the system is bipolar conducting, the flux through the membranes is the sum of the flux of Na^+ and Cl^-, which is also equal to the salt removal flux (Figure 1.5a). Therefore, the CE of the system is 1.

$$J_{CEM} = J_{AEM} = J_{Na} + J_{Cl}$$

$$CE = \frac{J_{salt\ removal}}{J_{membrane}} = \frac{J_{Na} + J_{Cl}}{J_{Na} + J_{Cl}} = 1$$

In ICP desalination, the flux through the membrane (CEM) is still the sum of the flux of Na^+ and Cl^-. However, ICP desalination is based on unipolar conduction of Na^+; it allows Cl^-, which has a higher electrical mobility, to relocate to the other side of the membrane more efficiently, thus enhancing the salt removal (Figure 1.5b).

$$J_{CEM} = J_{Na} + J_{Cl}$$

$$CE = \frac{J_{salt\ removal}}{J_{membrane}} = \frac{2J_{Cl}}{J_{Na} + J_{Cl}} > \sim 1.2$$

Therefore, the CE is higher for ICP desalination with CEMs. By the same principle, ICP desalination with AEMs has a CE less than 1; consequently, the salt removal ratio is also lower compared to ED or ICP desalination with CEMs. In this thesis, we will only consider ICP desalination with CEMs, for it has an advantage over ED in terms of current efficiency[16,20].

The bifurcating outlet in ICP desalination provides another benefit of particle removal along with salt removal. In most cases, the saline water contains pollutants other than salt ions. Since most particles have some sort of charge on the surface, they are also repelled from the ion depletion zone and can be removed through the concentrate stream. The particulate removal capability is valuable because it makes ICP desalination more robust against fouling, which is a challenge for membrane-based systems [21,22].

Electrodialysis is commonly known to efficiently desalinate brackish water, in the range of 1,000 to 8,000 mg/L[11,15]. However, electromembrane desalination technologies, such as ED and ICP desalination, may have favorable operation for high salinity applications because the high salinity enhances electrical conductance of the solution and leads to a lower electrical resistance and energy consumption. Several works have investigated and demonstrated potential of ED [23–25] and ICP desalination[21,26] for high salinity brine treatment. Electromembrane desalination at very low salinity is limited because the low limiting current at low salinity requires a large membrane area and hence a high capital cost.

Electromembrane desalination has several advantages over other desalination technologies. Electrodialysis can achieve a high recovery (up to 90%) since, unlike RO, there are no osmotic pressure limitations to the salinity of the concentrate stream[15]. On the other hand, the recovery of ICP desalination is inherently limited to 50% due to its bifurcated outlet design. In general, the pretreatment requirement for ED and ICP desalination is less strict than it is for RO due to the high mechanical and chemical stability of the IEMs and the reverse polarity operation [11,15]. Similar to other membrane desalination systems, ED and ICP desalination are modular systems and hence scalable. Since electromembrane desalination relies on transport of ions, rather than transport of water, it has a unique capability of partial desalination, in which the product water concentration can be adjusted. A combination of these features provides electromembrane desalination with potential in various niche applications, including partial desalination for surface water discharge and salt concentration for zero-liquid discharge.

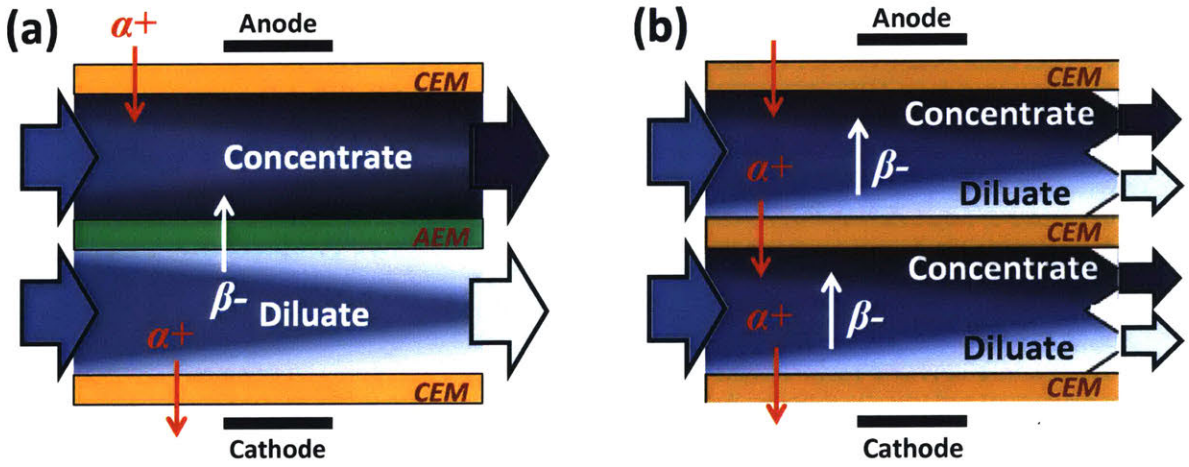

Figure 1.5 Schematic of (a) electrodialysis and (b) ion concentration polarization desalination (modified from Kim *et al.* [21])

1.3 Microfluidic engineering of electromembrane desalination

Eletrodialysis, which is the most well-established electromembrane desalination technology, is often considered a mature technology. However, the system parameters in ED are not fully optimized or characterized mainly due to the scientific complexity of the ion transport phenomenon in ED. In an industrial scale ED system, the engineering of the process has been done through a "black box" approach, in which the input parameters (*e.g.*, current or voltage, flowrate, channel geometry) are varied, and the performance is evaluated based on the output (*e.g.*, voltage or current, product concentration). A systematic engineering of the process requires detailed, microscopic system characterization [27]. Microfluidic platforms allow such characterization as they enable in situ visualization of ion concentration and flow velocity profiles. In fact, electrodialysis is essentially a massively parallelized microfluidic system, for it is a scaled-up two-dimensional system with channel dimensions in the range of microfluidics (channel width is 0.5mm – 2mm). Therefore, microfluidic engineering of ED, and other electromembrane processes, can provide scientific insights that were previously undiscovered and facilitate systematic engineering for better performance.

1.4 Thesis objectives

The overarching objective of this thesis was to study various aspects of engineering electro-membrane desalination technologies to achieve overall improvements, namely expand their use to a wider range of applications. I employed microfluidic platforms in these studies to gain scientific understanding of the micro-scale details of the processes, which can be utilized for their systematic engineering and optimization. By incorporating the findings from these studies,

and integrating them into a process, this thesis contributes to overall improvement of electromembrane desalination technologies.

To achieve the objective of improving the electro-membrane desalination, the thesis is divided into three parts. First, I aimed to expand the use of brackish water electrodialysis to a wider range of salinity by enhancing mass transport via structures in the diluate channels. In Chapter 2, I employed microfluidic experiments and numerical modeling to design the optimal structures that accounts for the asymmetry of cation and anion diffusivities. In Chapter 3, I continued the design of the structures with numerical modeling and optimized the size and the horizontal location. Secondly, I evaluated the techno-economic feasibility of electromembrane desalination in new applications of high salinity brine treatment. Specifically, I performed techno-economic analyses of ICP desalination, a relatively new electro-membrane technology, for partial desalination and brine concentration in Chapter 4. Lastly, in Chapter 5, I developed a total water purification system, named EC-ICP hybrid, that integrates an electrochemical pretreatment technology (electrocoagulation) and an electromembrane desalination technology (ICP desalination) into a single device.

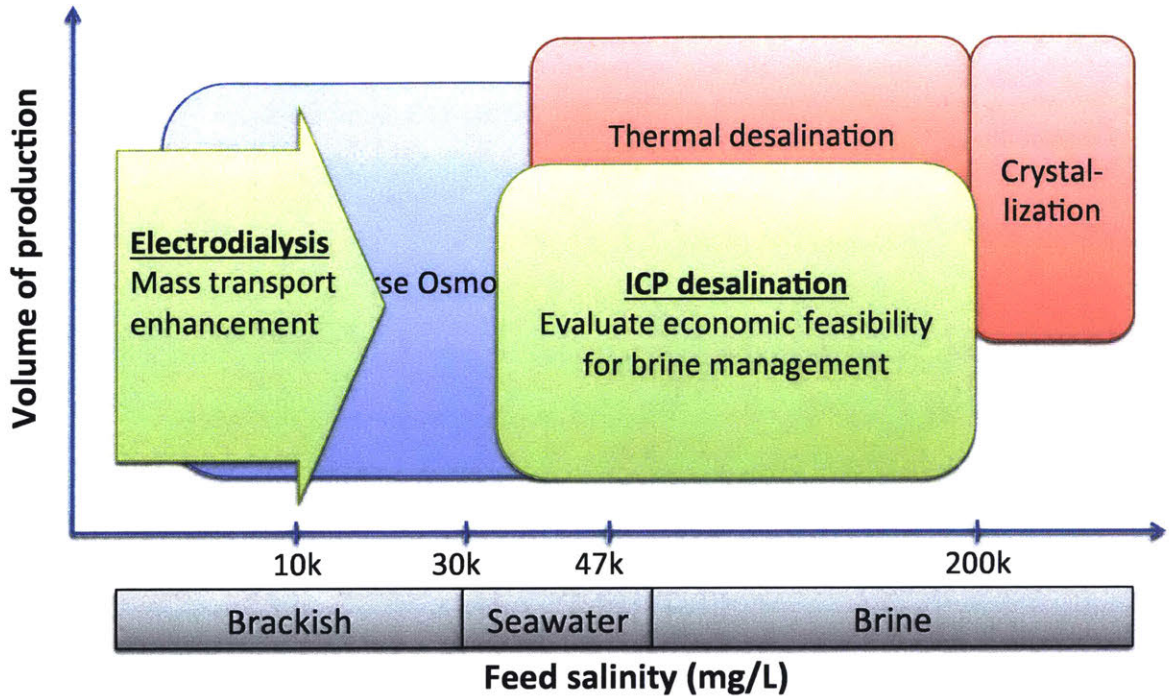

Figure 1.6 Desalination technologies plotted with their typical feed salinity and system size, with electromembrane desalination applications expanded based on this thesis.

1.5 References

[1] World Health Organization. Office of Global and Integrated Environmental Health, Health and environment in sustainable development : five years after the Earth Summit, 1997.

[2] JMP, Progress on drinking water and sanitation Programme – special focus on sanitation., 2008. http://www.wssinfo.org/documents-links/documents/?tx_displaycontroller%5Bcategory%5D=&tx_displaycontroller%5Byear%5D=2008&tx_displaycontroller%5Bsearch_word%5D=&tx_displaycontroller%5Btype%5D=.

[3] K.P. Lee, T.C. Arnot, D. Mattia, A review of reverse osmosis membrane materials for desalination—Development to date and future potential, J. Memb. Sci. 370 (2011) 1–22. doi:10.1016/j.memsci.2010.12.036.

[4] M.A. Shannon, P.W. Bohn, M. Elimelech, J.G. Georgiadis, B.J. Mariñas, A.M. Mayes, Science and technology for water purification in the coming decades, Nature. 452 (2008) 301–310. doi:10.1038/nature06599.

[5] Where is Earth's water? USGS Water-Science School, (n.d.). https://water.usgs.gov/edu/earthwherewater.html (accessed April 19, 2017).

[6] Global Water Intelligence, (n.d.). http://www.globalwaterintel.com/.

[7] B. Wang, Desalination water world | NextBigFuture.com, (2013). http://www.nextbigfuture.com/2013/10/desalination-water-world.html (accessed April 19, 2017).

[8] L.F. Greenlee, D.F. Lawler, B.D. Freeman, B. Marrot, P. Moulin, Reverse osmosis desalination: Water sources, technology, and today's challenges, Water Res. 43 (2009) 2317–2348. doi:10.1016/j.watres.2009.03.010.

[9] M.A. Darwish, F. Al Asfour, N. Al-Najem, Energy consumption in equivalent work by different desalting methods: case study for Kuwait, Desalination. 152 (2003) 83–92. doi:10.1016/S0011-9164(02)01051-2.

[10] N. Ghaffour, T.M. Missimer, G.L. Amy, Technical review and evaluation of the economics of water desalination: Current and future challenges for better water supply sustainability, Desalination. 309 (2013) 197–207. doi:10.1016/j.desal.2012.10.015.

[11] J. Drewes, T. Cath, J. Debroux, J. Veil, An Integrated Framework for Treatment and Management of Produced Water - Technical Assessment of Produced Water Treatment Technologies, Golden, CO, 2009.

[12] V.G. Gude, Desalination and sustainability – An appraisal and current perspective, Water Res. 89 (2016) 87–106. doi:10.1016/j.watres.2015.11.012.

[13] M. Elimelech, W.A. Phillip, The Future of Seawater Desalination: Energy, Technology, and the Environment, Science (80-.). 333 (2011). http://science.sciencemag.org/content/333/6043/712 (accessed April 13, 2017).

[14] C. Fritzmann, J. Löwenberg, T. Wintgens, T. Melin, State-of-the-art of reverse osmosis desalination, Desalination. 216 (2007) 1–76. doi:10.1016/j.desal.2006.12.009.

[15] H. Strathmann, Electrodialysis, a mature technology with a multitude of new applications, Desalination. 264 (2010) 268–288. doi:10.1016/j.desal.2010.04.069.

[16] R. Kwak, Nonlinear Ion Concentration Polarization: Fundamentals and Applications, Massachusetts Institute of Technology, 2013.

[17] R.F. Probstein, Physicochemical Hydrodynamics: An Introduction (Google eBook), John Wiley & Sons, 2005.

http://books.google.com/books?hl=en&lr=&id=Drm_YDcuv0MC&pgis=1 (accessed April 20, 2014).
[18] V.S. Pham, Nonlinear Electrokinetic Flow Near Permselective Membrane, National University of Singapore, 2012. http://scholarbank.nus.edu.sg/bitstream/handle/10635/35859/PhamVS.pdf?sequence=1 (accessed April 22, 2017).
[19] S.J. Kim, Y.-A. Song, J. Han, Nanofluidic concentration devices for biomolecules utilizing ion concentration polarization: theory, fabrication, and applications., Chem. Soc. Rev. 39 (2010) 912–922. doi:10.1039/b822556g.
[20] R. Kwak, V.S. Pham, B. Kim, L. Chen, J. Han, Enhanced Salt Removal by Unipolar Ion Conduction in Ion Concentration Polarization Desalination., Sci. Rep. 6 (2016) 25349. doi:10.1038/srep25349.
[21] B. Kim, R. Kwak, H.J. Kwon, V.S. Pham, M. Kim, B. Al-Anzi, G. Lim, J. Han, Purification of High Salinity Brine by Multi-Stage Ion Concentration Polarization Desalination., Sci. Rep. 6 (2016) 31850. doi:10.1038/srep31850.
[22] R. Kwak, V.S. Pham, B. Kim, L. Chen, J. Han, Enhanced Salt Removal by Unipolar Ion Conduction in Ion Concentration Polarization Desalination., Sci. Rep. 6 (2016) 25349. doi:10.1038/srep25349.
[23] Y. Oren, E. Korngold, N. Daltrophe, R. Messalem, Y. Volkman, L. Aronov, M. Weismann, N. Bouriakov, P. Glueckstern, J. Gilron, Pilot studies on high recovery BWRO-EDR for near zero liquid discharge approach, Desalination. 261 (2010) 321–330. doi:10.1016/j.desal.2010.06.010.
[24] R.K. McGovern, A.M. Weiner, L. Sun, C.G. Chambers, S.M. Zubair, J.H. Lienhard V, On the cost of electrodialysis for the desalination of high salinity feeds, Appl. Energy. 136 (2014) 649–661. doi:10.1016/j.apenergy.2014.09.050.
[25] T. Sirivedhin, J. McCue, L. Dallbauman, Reclaiming produced water for beneficial use: salt removal by electrodialysis, J. Memb. Sci. 243 (2004) 335–343. doi:10.1016/j.memsci.2004.06.038.
[26] B. Kim, H. Kwon, S.H. Ko, G. Lim, J. Han, Partial desalination of hypersaline brine by lab-scale ion concentration polarization device, Desalination. 412 (2017) 20–31. doi:10.1016/j.desal.2017.02.018.
[27] R. Kwak, G. Guan, W.K. Peng, J. Han, Microscale electrodialysis: Concentration profiling and vortex visualization, Desalination. 308 (2013) 138–146. doi:10.1016/j.desal.2012.07.017.

2. MASS TRANSPORT ENHANCEMENT USING MICROSTRUCTURES IN ELECTRODIALYSIS

*The published journal paper (B. Kim, S. Choi, V.S. Pham, R. Kwak, and J. Han, Journal of Membrane Science **524**, 280 (2017)) was used in its entirety for Chapter 2,with minor updates and modifications. S. C., B. K., and J. H. conceived the idea and designed the study, wrote the manuscript. B. K. carried out the experiments and analyzed the data. S. C. and V. S. P. carried out the simulations and analyzed the data. J. H. supervised the study.*

2.1 Introduction

Currently, reverse osmosis (RO) is considered the leading technology in the field of desalination, and the operation efficiency of RO has been significantly improved over the last two decades, mainly by energy recovery and other optimization. On the other hand, electromembrane desalination can be more advantageous in certain applications due to the flexibility of allowed feed conditions and the low capital cost needed (size of system is generally small). Modeling and optimization of electromembrane desalination systems, such as electrodialysis (ED), have been challenging, largely due to the multiphysics nature of its ion transport process. Despite these challenges, much progress has been achieved in understanding the transport process around ion exchange membranes (IEMs) through experiments and modeling. [1-11] The scientific knowledge obtained from these studies can be solid stepping-stones to be utilized in engineering of electrodialysis and other electromembrane processes, specifically in optimization of spacers in ED.

In an electrochemical system, ion transport near ion exchange membranes and electrodes induces inevitable concentration polarization [12] (*i.e.*, formation of diffusion boundaries) due to the difference in ion transport number between the solution and the IEMs. The resulting

diffusion boundary layer (also known as ion depletion region) on the surface of membrane/electrode increases the electrical resistance [13], and hence concentration polarization (CP) is a limiting factor for improving the efficiency of electrodialysis, as well as other electro-membrane processes, including reverse electrodialysis (RED) [14, 15] and membrane capacitive deionization [16, 17]. Concentration polarization impedes mass transport by creating a high electrical resistance in depletion zones (*e.g.*, diluate channels of ED; see Figure 2.1a) and increases the overall energy consumption [14, 18]. The effect of concentration polarization will be diminished with an increased intake flowrate [19, 20] (Figure 2.1b), but only at the cost of a lower salt removal ratio in spite of higher amount of salt removed from the feed solution. Given the fixed intake flowrate, mass transport can be enhanced via "mixing promoters", such as spacers [14, 18, 21, 22], corrugated membrane and electrode surfaces [23-27], ion conducting spacer [28, 29], pulsating flow [30], and air bubbling [31]. Yet, these methods to reduce the electrical energy consumption are accompanied by a significantly larger pressure drop due to an increased hydrodynamic resistance. Moreover, non-conductive mesh spacers, which are the most common means of mass transport enhancement in the ED and RED practice, have "shadow effect" [28], meaning that parts of membrane/electrode area are "shadowed" by the mixing promoter structures and reduce the effective surface area. The ion conducting spacers do not suffer from the shadow effect, but they are much more costly. An ideal spacer should be able to enhance the mass transport with a minimal increase in hydrodynamic resistance and is made of low cost material. More importantly, the aforementioned methods were developed without considering the asymmetric nature of cation/anion transport although different thicknesses of concentration boundary layers have been observed [32, 33].

In this work, we aimed to carry out a systematic analysis of mass transport enhancement in ED processes, by considering the difference in the anion and the cation transport, which arises from their difference in diffusivity. We demonstrated mass transport enhancement in an ED system by employing simple structures (with a relatively small increase in hydrodynamic resistance) inside the diluate channel, which perturb the flow profile locally, as shown in Figure 2.1c. These structures re-direct the flow to suppress (or expand) the concentration boundary layers and thus decrease (or increase) the electrical resistance. Our strategy is to maximize the flow velocity near the walls, which results in a relatively reduced flow in the center, to enhance mass transport. While it is in line with the previous studies that reduced resistance with an enhanced flow [19, 34], we examined the relation between the overall electrical resistance and the different diffusion boundaries on anion and cation exchange membranes (AEMs and CEMs), via experiments and multiphysics numerical modeling. We reveal novel insights on how to engineer optimal spacers given the asymmetric diffusivity of anions and cations in the feed. This is, to the best of our knowledge, the first study to consider the asymmetry of ion pair diffusivity into enhancing mass transport in electromembrane processes.

We demonstrated our ideas in a microfluidic model ED system [32], which can correlate the electrical response of the system with visualization of the flow and the ion concentration profiles. In addition, a direct numerical modeling of the system [35, 36] was used in order to elucidate the underlying mechanism behind the observed trends. Combined, the methodologies used in this study provide a well-defined, generally applicable strategy for model-based engineering and optimization of various electromembrane systems such as ED.

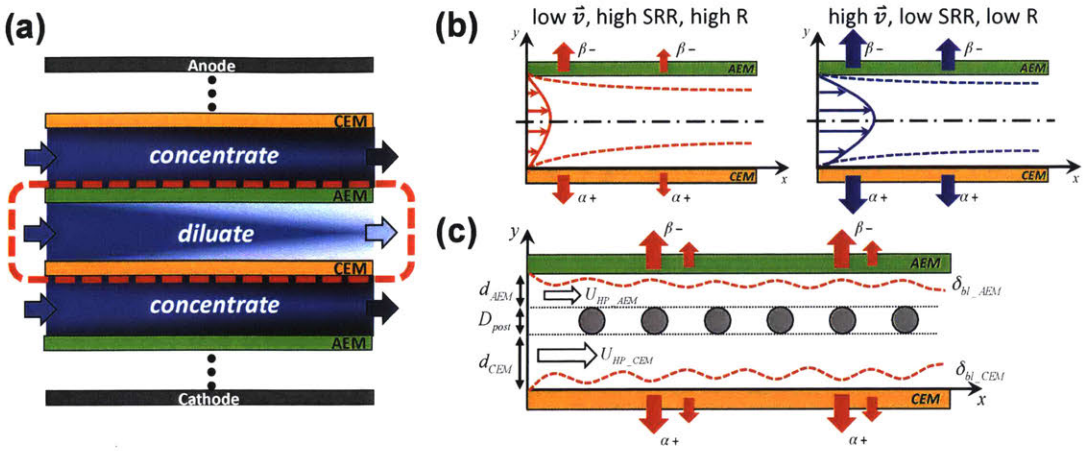

Figure 2.1 a) Schematic view of electrodialysis (ED). Color gradient indicates ion concentration profile. Electrical currents and constant forced flow are applied. Post structures are introduced in the red-boxed area whose details are described in b) and c). b) Velocity profile of the solution is drawn with a solid line, and the corresponding diffusion boundary layer for the solution of NaCl (α=Na, β=Cl) is drawn with a dotted line. The arrows represent the flux through the membrane. Blue on the right indicates a higher average velocity, compared to red on the left. A higher velocity results in lower salt removal ratio (SRR) but also a lower electrical resistance (R). C) Description of post geometry. D_{post} represents the diameter of posts; d_{CEM} and d_{AEM} are the minimum distance from the post to the CEM and the AEM, respectively. The average velocities above and below the posts are defined as U_{HP_AEM} and U_{HP_CEM}, respectively. The thickness of the diffusion boundary layers on the AEM and the CEM are termed as δ_{bl_AEM} and δ_{bl_CEM}.

2.2 Design of study

2.2.1 Definition of post-to-membrane distance

The post structures (intended to be representatives of typical "mixing promoters" or spacers, used in previous studies) were only considered inside the diluate channel since the ion depletion boundary and the consequent amplification of electrical resistance is only found in diluate channels. As illustrated in Figure 2.1c, D_{post} represents the diameter of posts; d_{CEM} and d_{AEM} are the minimum distance from the post to the CEM and to the AEM, respectively. The distance d' is defined as the ratio of d_{CEM} to the sum of d_{CEM} and d_{AEM}, *i.e.*, $d' = d_{CEM}/(d_{CEM}+d_{AEM})$. The cylindrical posts were placed in a symmetrical manner around the center

(d'=0.5). For example, d'=0.11 and d'=0.89 are equidistant from the CEM and from the AEM, respectively. The average velocities above and below the posts are defined as U_{HP_AEM} and U_{HP_CEM}, respectively. The thickness of the diffusion boundary layers on the AEM and the CEM are termed δ_{bl_AEM} and δ_{bl_CEM}. We only considered the effect of d' on the boundary layer modification, and hence the size and the frequency of the posts were kept constant.

2.2.2 Microfluidic electrodialysis platform

The fabrication of a microfluidic ED device has been developed in our group previously, and the detailed fabrication process is found elsewhere [32]. In the microfluidic experiment, a charged fluorescent dye (Alexa 488 Fluor®, Invitrogen) was added to track the ion concentration profile within the channel, which can be observed under a microscope. The fluorescent dye concentration is relatively low (~1μM), compared to the total ion concentration (10mM), and thus the dye does not affect the current flow. This method of ion concentration tracking with fluorescent dye has been used in previous studies to observe ion concentration polarization. [37, 38] In order to accurately measure the voltage drop across a unit ED cell pair, Ag/AgCl electrodes were inserted at the center of two concentrate channels, as shown in Figure 2.2a, while a constant current was applied from the anode to the cathode. (Detailed experimental setup is described in Section 2.7.1.)

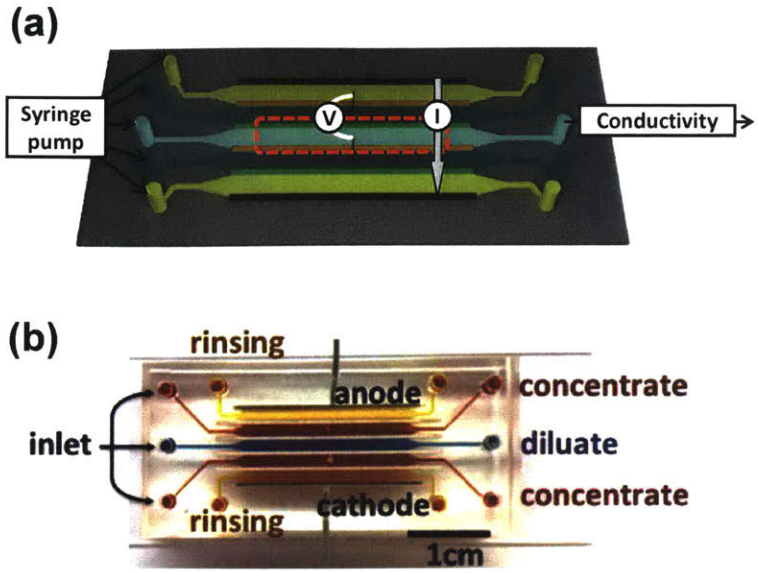

Figure 2.2 a) Schematic of ED device used in the experiments. The solutions were introduced by syringe pumps. The flowrates were 50μL/min for brine and dilute channels and 250μL/min for rinsing channels. The concentration of the solutions was 10mM (of NaCl or KCl). A constant current was applied, and the voltage was measured for a single cell pair (from the center of a brine channel to the center of the other brine channel). The process was visualized in the red-boxed area. The conductivity of the desalinated solution was measured at the outlet. b) Actual microfluidic ED device. Colored dye was introduced to visualize the channels. Blue represents diluate; red represents concentrate; yellow represent rinsing channel.

2.2.3 Numerical modeling

Simulation results were obtained by a direct numerical simulation, which was developed by Pham *et al.* [35] The simulation relies on the direct, coupled solution of the full set of Poisson-Nernst-Planck and Navier-Stokes equations. In this work, we used a 2D modeling of ED systems, while a full 3D modeling of electromembrane systems have been reported recently. [36] (Detailed method and simulation setup are described in Section2.7.2.)

2.3 Characterization of ion concentration profile and current-voltage response

The concentration of sodium chloride (NaCl) inside the diluate channels with different post-to-membrane distances (d') was visualized with charged fluorescent dye molecules in Figure 2.3a. It should be noted that the dye was used only for the qualitative comparison of the relative depletion layer thicknesses among the different post designs. The dark zones near the membranes roughly represent the ion depletion boundary layers. The three microscopic images for each structure design correspond to the three ion transport regimes of the current-voltage response shown in Figure 2.3b. The first of the three is commonly known as 'Ohmic regime'[18, 28], in which the ion flux increases linearly with an increasing driving force (electric potential). It should be noted that the potential in this regime is contributed by Donnan potential, in addition to the Ohmic resistance of the membranes and the solution [39]; following the conventional nomenclature in the field, this regime will be referred as 'Ohmic regime'. In Figure 2.3a, the concentration profile in the Ohmic regime is characterized by a thin layer of depletion on the membranes. As the applied voltage increases, the ions in the boundary layers are depleted faster than they are supplied from the bulk by diffusion; a further increase in the potential can no longer increase the ion flux, shown by the plateau region in Figure 2.3b. This plateau of current due to the diffusion limit is known as the limiting regime, and the current at the transition between the Ohmic and the limiting regimes is termed limiting current. The concentration profile in the limiting regime in Figure 2.3a shows a dark and thick boundary layer, compared to the Ohmic regime. With a further increase in the potential drop, a new mode of ion transport sets in, termed overlimiting regime, which is evidenced by the positive slope after the plateau in the current-voltage response. An electroconvective flow is behind the overlimiting current behavior

[5, 40] in planar membrane systems such as ED and can be observed with the vortices on the IEM in the overlimiting regime, as shown in Figure 2.3a.

In order to quantify the effect of structure location on the overall ion transport, we studied an ED system with cylindrical posts placed at a varying d', which represents the relative distance from the posts to the membranes. A channel with no post structures was also studied as a control case. Under a constant flowrate, each post position, defined with d', provides unequal average flow velocities (U_{HP_AEM} and U_{HP_CEM}) from two sides of the posts by allocating different hydrodynamic resistances. The concentration gradients in Figure 2.3a show that when the posts are closer to a membrane, the depletion layer becomes thicker, suggesting a slower local velocity near that membrane. Depending on the location of the posts, the boundary layer can be made either thinner or thicker, compared to the channel with no structures. Since the depletion layer thickness is directly related to the efficiency of mass transport, we can expect that mass transport can be either facilitated or inhibited by the position of the posts. The current-voltage responses both in the experiment and in the simulation (Figure 2.3b and c) show that the current-voltage curve (IV curve) for posts near the center (or near the IEMs) is above (or below) that for the control. Our results clearly indicate that simple and small post structures can enhance the mass transport even in a laminar flow ($Re < 1$; Values of Re are specified in Section 2.7.1), in the absence of turbulent mixing.

It is noteworthy that the depletion layer thickness near the CEM and the AEM (*i.e.*, δ_{bl_AEM} and δ_{bl_CEM}) could be different, even in the absence of flow modification by structures (*i.e.*, control design). Zabolotskii *et al* [41] and Shaposhnik *et al* [42] have reported different concentration profiles adjacent to the CEM / AEM based on their numerical and experimental studies, respectively. In case of NaCl solution, the difference in diffusion boundary layer arises

from the different diffusivity of sodium (D_{Na+} =1.33x10^{-9}m^2/s) and chloride ions (D_{Cl-}= 2.03x10^{-9}m^2/s), as explained in Kwak *et al.* [33, 43] The asymmetry of cation/anion diffusivity leads to asymmetry in the IV responses in relation to the post location d'. In Figure 2.3b and c, the experiments and simulation both show that the maximum mass transport is achieved when posts are located slightly closer to the AEM side. This trend is in agreement with the visualization results that the structures on the AEM side generally provide a thinner depletion layer thickness (see the enlarged images in Figure 2.3a).

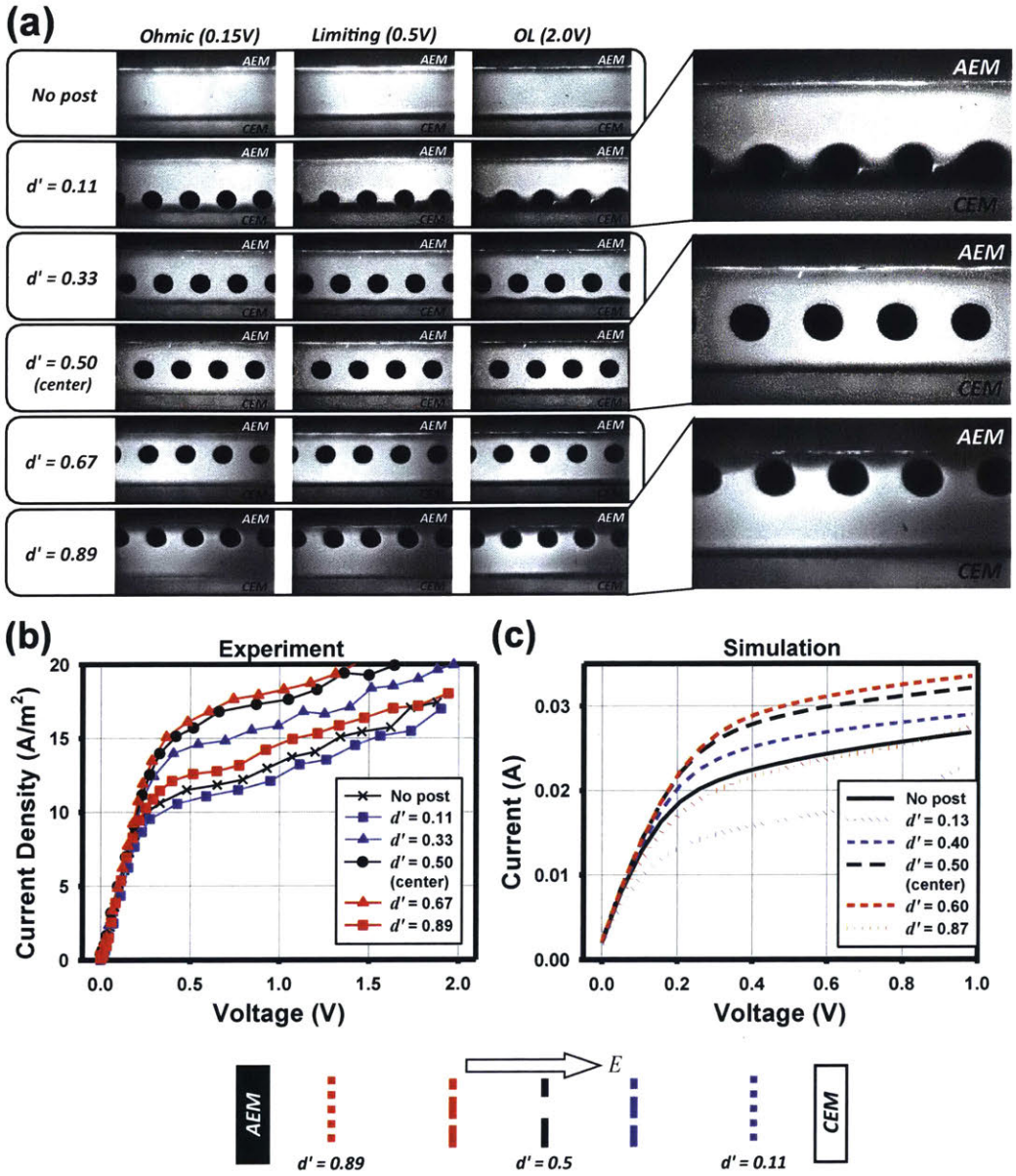

Figure 2.3 a) Fluorescent images of dilute stream in Ohmic, limiting and overlimiting regime for different d'. Charged fluorescent dye was used to visualize local ion concentration and especially the depletion boundary layers. On the right are enlarged images of three channel designs in the overlimiting regime to show the asymmetric boundary layers on the membranes. b) Current-voltage response from experiments. c) Current-voltage response from simulation. In current-voltage curve, electrical resistance is represented by the slope. The location of the posts and the corresponding d' are indicated below the plots.

2.4 Effect of asymmetry in cation/anion diffusivity

We also carried out a detailed quantitative analysis on the asymmetry in mass transport with respect to the post-to-membrane distance (d') by plotting the limiting current density. As it is a common practice to operate ED at the current level of 80% of the limiting current [28], the improvement on the limiting current should be an appropriate metric for mass transport enhancement. Plotted in Figure 2.4a is the limiting current corresponding to the experimental and simulation results from Figure 2.3, as a function of the post-to-membrane distance (d'). In general, the limiting current increases as the post location varies from the membranes towards the center of the channel. However, the plot is shifted towards the AEM side with the maximum current measured off the center when the posts are located around d' = 0.6 (d'=0.67 for experiment and d'=0.6 for simulation). We postulated that this trend is due to the asymmetry in ion diffusivity, as discussed with Figure 2.3. In order to verify our hypothesis regarding the asymmetrical distribution of the depletion region, further experiments and simulation were conducted with potassium chloride (KCl), whose cation and anion diffusivities are close to each other. The results for the potassium chloride solution support our explanation, as can be seen by the maximum limiting current density observed at d'=0.5 (posts at center) and the symmetrical shape of the plot for both simulation and experiments (Figure 2.4b).

In order to examine the correlation between the formation of diffusion boundary layer and the enhancement of the limiting current density observed in Figure 2.4a and b, we visually explored the ion concentration gradient for sodium chloride and potassium chloride and the flow velocity profile through numerical analysis (Figure 2.4c). We only considered the Ohmic and the limiting regimes, in which the electroconvection is absent. Comparing the data for the control case (no post), the concentration gradient near the AEM and CEM is symmetrical for KCl; for

NaCl, the concentration gradient near the CEM is larger (*i.e.*, depletion region is thicker) than that near the AEM due to the faster escaping velocity of co-ion (Cl^-) on the CEM side. Observing the cases of NaCl at d'=0.6 and KCl at d'=0.5, we can conclude that the mass transport is maximized when the depletion boundary layers from both membranes are similar in size, as can be seen by Figure 2.4c. On the contrary, a thick depletion layer near either of the IEMs determines the extent of mass transport reduction since a strong depletion layer is a major contributor to the overall electrical resistance in the system. Therefore, one can achieve a maximum mass transport at a given flowrate by matching the diffusion boundary layers on the IEMs, which can be achieved by properly positioning the post structures that reflects the asymmetry in ion diffusivity.

It is true that the posts near the center direct more flow (increasing actual flow velocity) towards the membranes, reduce the thickness of the diffusion boundary layers, and thus enhance the mass transport in a macroscopic perspective. While post arrays play a role in increasing the flow velocity near the membrane, it should be noted that they generate larger periodic flow velocity gradient near the membrane, which results in the additional mass transport. [23, 25] In order to verify the relationship between the local mass transport and the flow velocity gradient when using NaCl solution, we examined a local Sherwood number [23] and flow velocity gradient along the membrane. (y=0, on the CEM) As shown in Figure 2.4d, the overall Sherwood number increases as the post arrays placed close to the center (d'=0.5). It is because the post arrays in close proximity to the membrane considerably limit the mass transport through the near side membrane (CEM or AEM) in spite of much enhanced flow velocity/gradient near the another side membrane (AEM or CEM). As a result, the more limited mass transport in the narrow side dominates the overall mass transport in the system. Interestingly, this general

tendency with the position of the post arrays is always kept only except when we observe that the Sherwood number at d'=0.6 (red) shows slightly higher values than d'=0.5 (red, center) while those at d'=0.4 (brown, symmetric position to d'=0.6) shows less values than d'=0.5. As we already discussed, it should be originated from intrinsic asymmetry of NaCl transport near CEM/AEM in such a way that the mass transport near CEM dominates the overall transport rate due to its thicker depletion zone. As shown in Figure 2.4c and e, the velocity and the velocity gradient of d'=0.6 are always higher than those of d'=0.5 (center) which should result in the mass transport enhancement on the CEM and improvement of the overall mass transport in the ED system in spite of transport decrement on the AEM. Nevertheless, if the post arrays are placed closer to the membrane (d'=0.13 close to CEM, or d'=0.87 close to AEM), a degree of mass transport reduction in the narrow zone (between the membrane and the post arrays) should overwhelm a degree of mass transport enhancement in the wide zone, thereby leading to decrement of overall mass transport. (See orange and purple lines in Figure 2.4d) The another interesting observation is that, in the case of d'=0.13, there is a discordance between place with local maximum value of Sherwood number and post structures (Figure 2.4d), while in all the other cases local maximum value of velocity gradient match the locations of post structures (Figure 2.4e). It is presumably because post structures very near to the membrane could obstruct local mass transport by 'shadowing' ion conducting path in addition to decreasing the local flow velocity.

It is worthwhile examining whether our method of mass transport enhancement by flow redistribution is more efficient, compared to other previously recognized scenarios such as increasing the velocity of the flow intake, or decreasing the intermembrane distance. To show the efficacy of flow redistribution by posts, we compared the center post design (d'=0.5) with two

cases of increased bulk flow in simulation (Figure 2.5). First, the feed flow was increased to match the average velocity with the post design, while keeping the channel dimensions unchanged. Second, in addition to the increased feed flow, the width of the channel was reduced to match the channel volume available to the fluid in the post design, in order to maintain the same flowrate. As shown in Figure 2.5, the mass transport in the post arrays is significantly greater than that in both cases of matching bulk flow. Therefore, it is reasonable to assume that the post arrays contribute to not only the increasing flow velocity near the membrane, but also generating periodic velocity gradient, which enhances local mass transport (*Sherwood* number in Figure 2.4d) periodically. Additionally, it should be emphasized that applying flow redistribution (asymmetrically) enables to match the diffusion boundary layers on the CEM/AEM in order to maximize overall mass transport from the given channel configuration. Therefore, we can deduce that the localized flow perturbations near the membranes, rather than an increase in the bulk flow or decrease in the intermembrane distance, contribute to the observed mass transport enhancement.

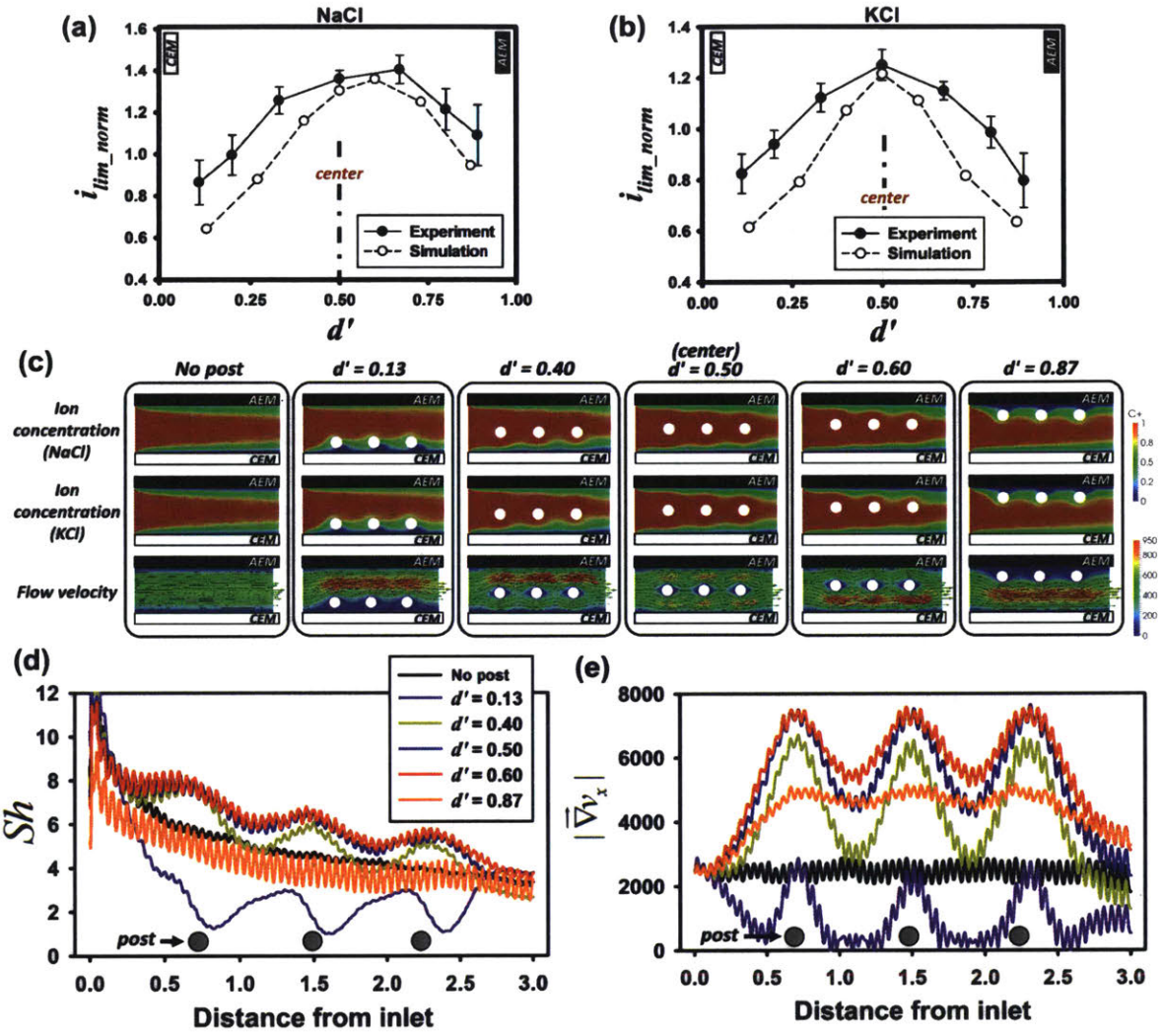

Figure 2.4 Normalized limiting current density vs. d' for a) NaCl and b) KCl. The current density was normalized with that of the control. The solid dots and hallow dots represent the experimental and simulation results, respectively. The error bars represent the standard deviations. c) Ion concentration profiles for NaCl and KCl and flow velocity for various d' from the simulation. The color scale bars are shown on the right end. d) Local Sherwood number (*Sh*) distribution and e) magnitude of local flow velocity gradient along the CEM (y=0) from the simulation. The fluctuations in the plots (d) and (e) are numerical artifacts.

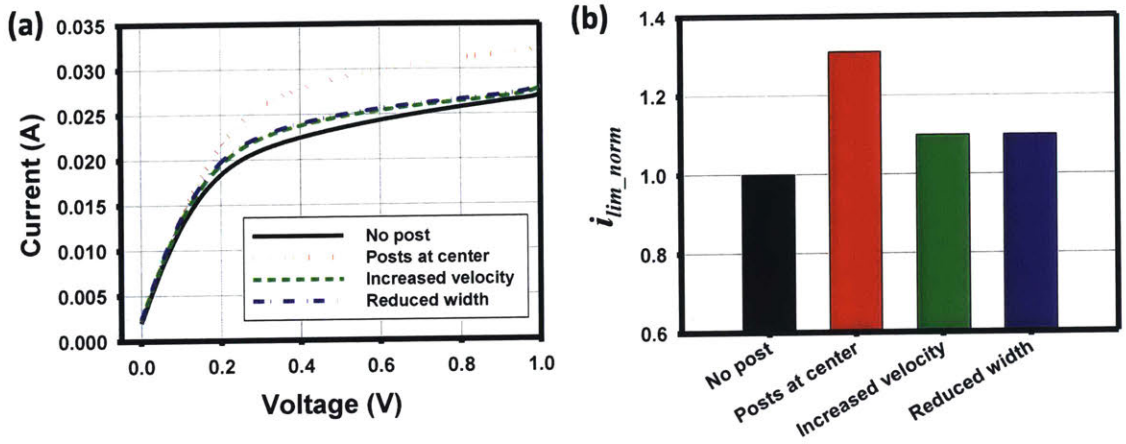

Figure 2.5 Comparison of local vs. bulk flow modification. "No post" and "posts at center" represent the simulation results for "no post" and "d'=0.5" from Figure 3(c), respectively. "Increased velocity" represents the result for the same channel as "no post" and the same average velocity as "d'=0.5". "Reduced width" represents the result for a reduced channel width, an increased velocity, and the same flowrate as "no post" and "d'=0.5". All results are generated with NaCl as the salt used. a) Current-voltage responses. b) Limiting currents, normalized to the limiting current of "no post".

2.5 Implication to electrical energy efficiency

Based on the analysis on optimal d', we related the mass transport to the electrical energy efficiency by introducing the definition of the energy per ion removal (EPIR) [44]. The EPIR and the current efficiency (CE) are defined below.

$$\text{EPIR} = \frac{IV/Q_{diluate}}{zk_BT(C_0 - C_{diluate})} \propto \frac{V}{CE}$$

$$\text{CE} = \frac{zFQ_{diluate}(C_0 - C_{diluate})}{I}$$

where z, F, k_BT indicate the ion valence, or the charge of ions, Faraday's constant ($=9.65\text{x}10^4 \text{C}\cdot\text{mol}^{-1}$), and the thermal energy (=2.479kJ/mol, k_B and T are Boltzmann constant and temperature), respectively. V is the voltage drop across a single cell pair, I is the current, C_0

is the ion concentration in the feed, $C_{diluate}$ is the ion concentration exiting the diluate channel, and $Q_{diluate}$ is the flowrate of a single diluate stream.

The EPIR is an appropriate metric to evaluate the electrical energy efficiency in electromembrane desalination systems, for it contains information about the current, voltage, and salt removal and recovery. The CE represents the fraction of the total applied current that is utilized for ion removal [45, 46]. In our study, the CE is defined as the ratio of the amount of salt molecules removed over the total current, and thus the maximum achievable CE is 1. As can be inferred by the definition above, reduction in EPIR can be achieved with an enhanced mass transport (*i.e.*, lower electrical resistance) and a high current efficiency. In the experiment, we measured the conductivity drop in the diluate channel to calculate the current efficiency and the EPIR values. In the complete energy analysis of electrical desalination system, the pumping power to drive the flow needs to be accounted as well as the electrical energy consumption. However, in typical ED systems and our system, the energy required for the pressure driven flow is much lower (typically ~1000x) than the electrical energy required [47] (see Sections 2.7.4 and 0). In addition, the viscous dissipation is expected to be very small based on other studies in similar systems [8]. The EPIR and the CE based on the experimental results with the NaCl solution is plotted as a function of d' in Figure 2.6a. The results show that the EPIR is minimized at d' = 0.67, which coincides with the greatest mass transport enhancement in terms of the limiting current density and with the maximum CE. Less concentration polarization leads not only to a lower electrical resistance in the boundary layer but also to a higher CE across the IEMs (see Section 2.7.3), which ultimately results in a lower EPIR.

In Figure 2.6, the salt removal ratio and EPIR for various d' are plotted from the experimental (Figure 2.6b) and simulation (Figure 2.6c) results. It is insightful, and practically

important, to appreciate the effect of d' on the overall relation between the salt removal and the EPIR. For a typical ED system with a given channel design, the EPIR should increase with an increasing salt removal ratio, as shown with the gray line in Figure 2.6b. In other words, lower EPIR (*i.e.*, higher energy efficiency) can be achieved by operating at a lower current, but this leads to a lower salt removal and therefore an (undesirable) increase in capital cost (*i.e.* amount of membrane used, or channel length). While such a tradeoff between energy and membrane area efficiency is rather ubiquitous in any electromembrane processes, one can independently improve this relationship by modulating d' in our post-embedded ED system (Figure 2.6b and c). When the posts are closer to the center, the data points in Figure 2.6b lie below the 'energy – salt removal ratio' line for the control case, and hence a lower energy and a higher salt removal can be achieved simultaneously. Moreover, the simulation results in Figure 2.6c show that when the posts are near the center, the maximum achievable salt removal is higher. This is shown with the shift of the vertical slope that indicates the limiting current regime. Interestingly, the 'energy – salt removal ratio' relationship for the post-embedded system can in fact become worse than that for the control case, when the posts are closer to the IEMs, which is shown with the data below the gray line in Figure 2.6b. This is a clear demonstration that a design of the spacer in ED system may indeed be detrimental to the overall efficiency, instead of the intended 'promoted mixing', and signifies the critical importance of proper, model-based engineering of spacer structures inside the ED channels.

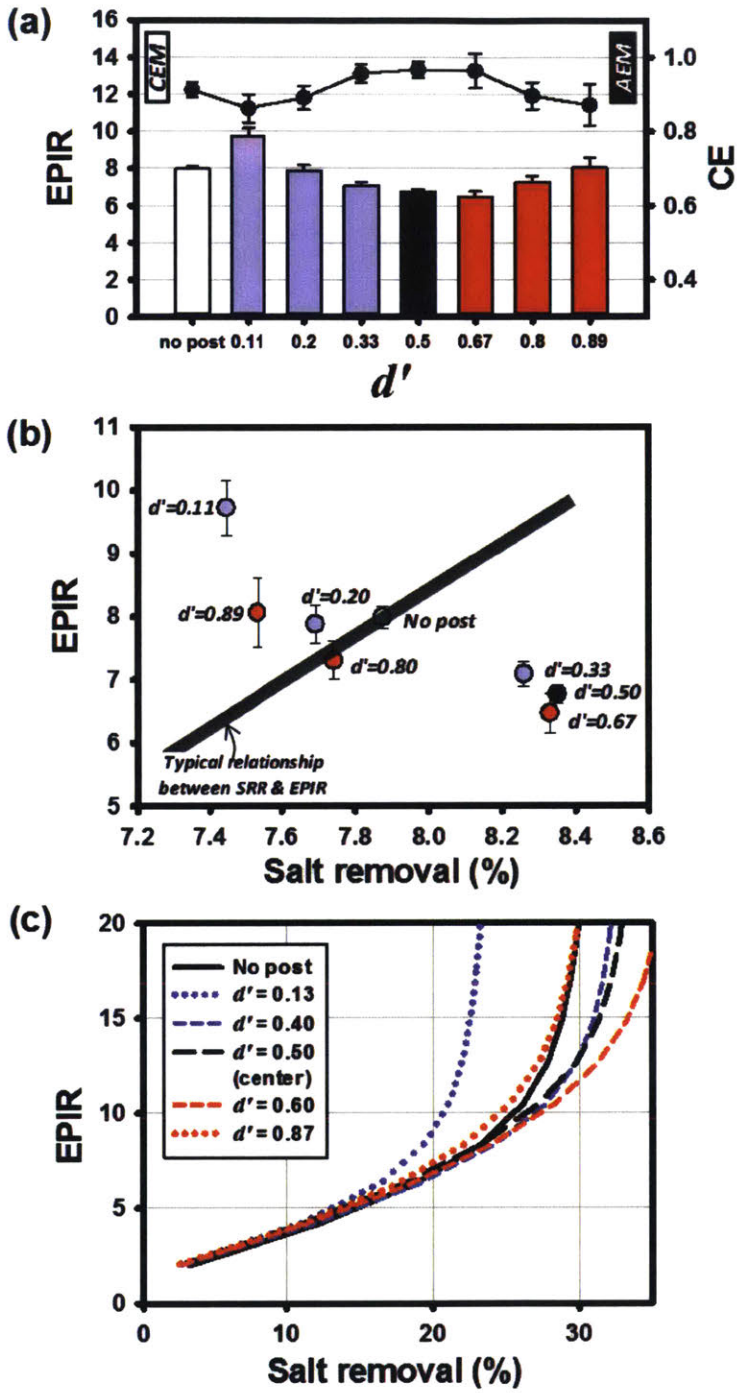

Figure 2.6 a) The energy per ion removal and current efficiency from experiments are represented by bars and dots, respectively. b) EPIR vs. salt removal ratio for various d', obtained from experiments. The black line indicates a typical relation between EPIR and SRR. c) EPIR vs. salt removal ratio for various d', obtained from simulation. Blue and red lines indicate structures are on the CEM and the AEM sides, respectively.

2.6 Conclusion

In this work, we demonstrated that the mass transport in electromembrane systems can be enhanced by increasing the local flow velocity in the concentration polarization region. Modulating the local flow near the membranes (AEM or CEM) was realized by placing a row of post structures with a varying distance to the membrane (*d'*), which results in a redistribution of the hydrodynamic resistance inside the diluate channel. Differentiated from previous efforts for the ED spacer, our study reveals that ion transport can be enhanced or reduced not only by an average flow velocity, but also by an asymmetric distribution of flow velocity inside a diluate channel. Based on the fact that the thickness of CP boundary near the membranes (AEM or CEM) should be differentiated by the relative difference of co-ion diffusivities (D_{Na+} =1.33x10^{-9}m^2/s: co-ion in the AEM side, D_{Cl-} =Z2.03x10^{-9}m^2/s: co-ion in the CEM side), applying a slightly higher local flow velocity near the CEM side than the AEM side results in the maximum enhancement of mass transport at a given flow rate, showing almost comparable thickness of CP boundary near AEM and CEM. As a result, the optimal mass transport in an electromembrane system with sodium chloride feed can be obtained when the post structures are placed slightly closer to the AEM than to the CEM. By optimizing the position of the post structures in our experimental and numerical studies, the electrical energy was enhanced up to 30 – 40%, while the effect of increased hydrodynamic resistance to the total energy was negligible. The findings from the experiments and the numerical modeling support this previously unexplored effect of asymmetric diffusivity. The concentration and flow profiling through the simulation was used to corroborate the reasoning.

It should be mentioned that our study was done in the laminar flow regime, and no turbulent flow was observed throughout the study. However, asymmetry of cation/anion

diffusivity is a property of ions in the solution and independent of flow characteristics. Hence, the diffusivity-based engineering of the structures can be applied to designing of conventional spacers and mixing promoters in a system with a higher flow. Furthermore, following up on our findings, the effect of similar structures in a system with a high Reynolds number can be a subject of future studies. Our work employed electrodialysis as a model system, but the findings from this study is pertinent to a larger field of study in many other electromembrane systems, such as reverse electrodialysis and (membrane) capacitive deionization.

2.7 Supplementary information

2.7.1 Experimental setup

Device fabrication

The fabrication of a microfluidic electrodialysis (ED) device has been developed in Han group, and the detailed fabrication process is described in Kwak *et al*[27]. Briefly, the microfluidic ED device consists of two rinsing channels adjacent to the electrodes, two concentrate channels, and a diluate channel in the center. The device is fabricated by assembling the top and bottom parts, each with matching slots for membranes and electrodes and gaps between the two parts, which become the channels. The slots for the membranes and the electrodes are much deeper than the channels, in order to prevent inter-channel leakages. Polydimethylsiloxane (PDMS) was selected as the device material for its optical transparency and flexibility. The negative features of the device were fabricated through stereolithography (Accura SL 5530, 3D systems Inc., USA), and the PDMS device parts were casted from this mold. The two parts were bonded by air plasma treatment of the bonding surfaces. The membranes were assembled dry as they came, and swelled in deionized (DI) water for 24 hours

after the boding, during which any gaps between the structure and the membranes were sealed to prevent from inter-channel ion leakage. Preceding the experiments, Ag/AgCl electrodes were inserted at center of two concentrate channels to measure the voltage drop across a single cell pair.

The dimensions of each channel in the device were 1.5mm in width (distance between adjacent membrane/electrode), 300μm in depth, and 20mm in length. The diameter of the posts (D_{post}) was 400μm. The electrode material was carbon paper (Spectracarb 2050A, FuelCellStore©, USA). Fumasep® FTAM-E and FTCM-E (FuMa-Tech GmbH, Germany) were used for cation and anion exchange membrane (CEM and AEM) materials. PDMS used as the device material was Sylgard 184 from Dow Corning Corporation, Michigan. Ag/AgCl electrodes were obtained from (Ag/AgCl Sintered, 0.015" diameter, A-M Systems, USA).

Device operation

The assembled device was connected to the feed solution and the outlet with tubing and a source-measurement unit and placed under the microscope for the experiment. The feed solution was introduced to the device with syringe pumps (PHD 2200, Harvard apparatus). Charged fluorescent dye (Alexa 488 Fluor®, Invitrogen) was added to track the ion concentration profile within the channel, which can be observed using an optical microscope (IX-71, Olympus). The fluorescent dye concentration is relatively low (~1uM), compared to the total ion concentration (10mM), and thus the dye does not affect the current flow. Moreover, Alexa 488 is known to be pH-insensitive over a wide range (pH= 4 – 9) and highly photostable[28] A constant current was applied using Keithley 236 current-voltage source measurement unit (Keithley Instruments, Inc., USA) across the entire ED device, and the corresponding voltage drop across a single ED cell pair was measured with Multimeter (Fluke 45, Fluke Inc., USA). The bulk concentration of the

product stream is monitored with a conductivity meter (VWR symphony conductivity meter, VWR International, LLC, USA) connected to a flow-through conductivity microelectrode (Microelectrode, Inc., USA).

The solution was composed of either 10mM NaCl or 10mM KCl in DI water. The salts were obtained from Sigma Aldrich. Throughout the experiments, the flowrates were 36uL/min for desalination (concentrate and diluate) channels and 300uL/min for rinsing channels, corresponding to the linear velocity of 80mm/min (Re = 0.73) and 667mm/min, respectively. The operating voltage drop across the device ranges from 0 to 20V.

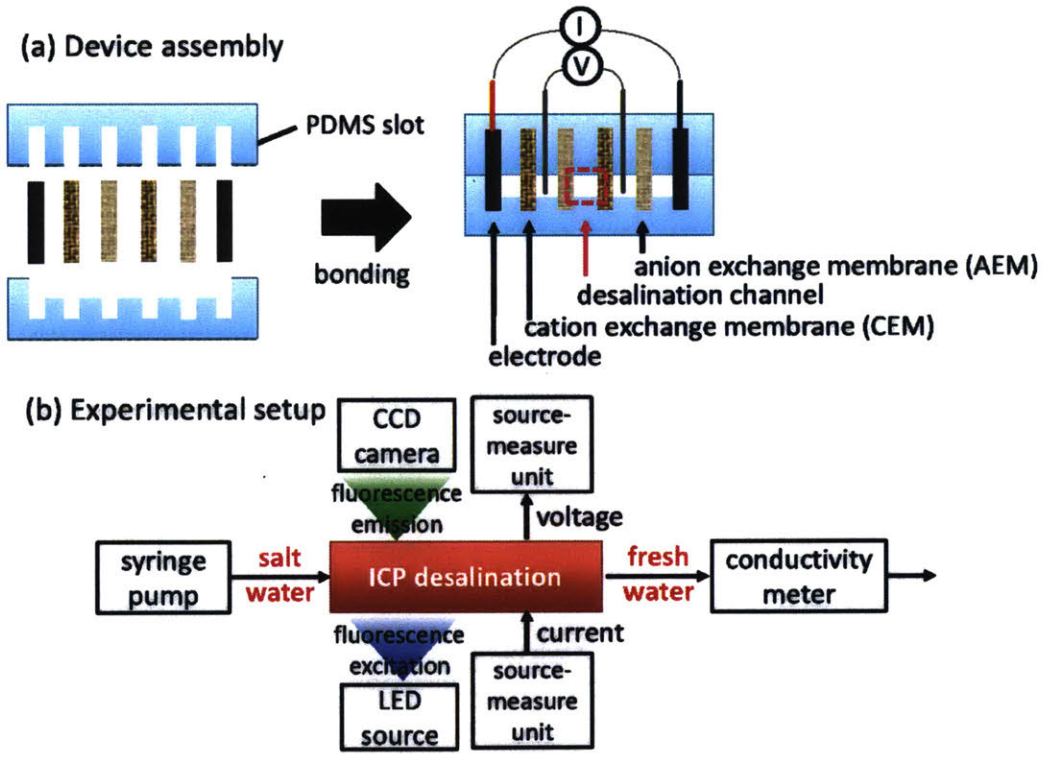

Figure 2.7 (a) Schematic view of device fabrication and (b) the experimental setup

2.7.2 Simulation method

Multiphysics modeling used in this paper was done by numerically solving the full set of governing equations without simplifications in a model system, which is illustrated in Figure 2.8. Here, we briefly describe the simulation method; the detailed method can be found in a previous work from Han Group[29].

The set of governing equations to describe the system includes Poisson-Nernst-Planck and Navier-Stokes equations. Nondimensional forms of the equations are written below:

$$\text{Nernst-Planck: } \frac{1}{\tilde{\lambda}_D}\frac{\partial \tilde{C}_\pm}{\partial \tilde{t}} = -\nabla\cdot\tilde{J}$$

$$\tilde{J}_\pm = -\tilde{D}_\pm\left(\nabla\tilde{C}_\pm + Z_\pm\tilde{C}_\pm\nabla\tilde{\Phi}\right) + Pe\tilde{U}\tilde{C}_\pm$$

$$\text{Poisson: } \tilde{\lambda}_D^2\nabla\cdot\left(\nabla\tilde{\Phi}\right) = -\tilde{\rho}_e$$

$$\tilde{\rho}_e = Z_+\tilde{C}_+ + Z_-\tilde{C}_-$$

$$\text{Navier-Stokes: } \frac{1}{Sc}\frac{1}{\tilde{\lambda}_D}\frac{\partial\tilde{U}}{\partial\tilde{t}} = -\nabla\tilde{P} + \nabla^2\tilde{U} - \mathrm{Re}\left(\tilde{U}\cdot\nabla\right)\tilde{U} - \tilde{\rho}_e\nabla\tilde{\Phi} = 0$$

$$\nabla\cdot\tilde{U} = 0$$

where $\tilde{t} = t/\tau_0$, $\tilde{C}_\pm = C_\pm/C_0$, $\tilde{\Phi} = \Phi/\Phi_0$, $\tilde{U} = U/U_0$, $\tilde{P} = P/P_0$ are the normalized time, concentration, electric potential, fluid velocity, and pressure, respectively. The reference constants are defined below:

$$\tau_0 = \frac{l_0^2}{D_0};\ C_0 = C_{\text{bulk}};\ \Phi_0 = \frac{k_BT}{Ze};\ U_0 = \frac{\varepsilon\Phi_0^2}{\eta l_0};\ P_0 = \frac{\eta U_0}{l_0}$$

where C_{bulk} is the bulk concentration, l_0=w is the characteristic length scale, $D_0 = (D_+ + D_-)/2$ is the average diffusivity, k_B is the Boltzmann constant, T is the absolute temperature, e is the

elementary charge, Z is the ion valence, η is the dynamic viscosity of solution, and ε is the permittivity.

Normalized diffusion coefficient, Debye length ($\lambda_D = \sqrt{\varepsilon k_B T / 2C_{bulk} Z^2 e^2}$) and space charge are defined $\tilde{D}_{\pm} = D_{\pm}/D_0$, $\tilde{\lambda}_D = \lambda_D / l_0$, and $\tilde{\rho}_e = \rho_e / C_{bulk}$, respectively.

The dimensionless numbers (Peclet, Schmidt, and Reynolds numbers) are defined below:

$$Pe = U_0 l_0 / D;\ Sc = \eta / \rho D_0;\ \mathrm{Re} = \rho U_0 l_0 / \eta$$

The governing equations above were solved numerically. The finite volume method was used for discretization of the governing equations, and the Newton-Raphson method was used for the nonlinear discretization of the Poisson-Nernst-Planck equations.

The parameters used in the numerical modeling are listed in the Table below.

Table 2.1 Parameters for simulation

Symbol	Description	Value
T	Absolute temperature	300 K
λ_D	Debye length	4.36 nm
D_+	Diffusivity of cations	1.33×10^{-9} m^2/s for Na^+ 1.95×10^{-9} m^2/s for K^+
D_-	Diffusivity of anions	1.33×10^{-9} m^2/s for Cl^-
C_0	Bulk concentration	5 mM
Φ_0	Thermal voltage	25.7 mV
U_0	Velocity scale	29.66 μm/s
U_{HP}	Average velocity at inlet	1.19 cm/s
l_0	Length scale	20 μm
Re	Reynolds number	0.28

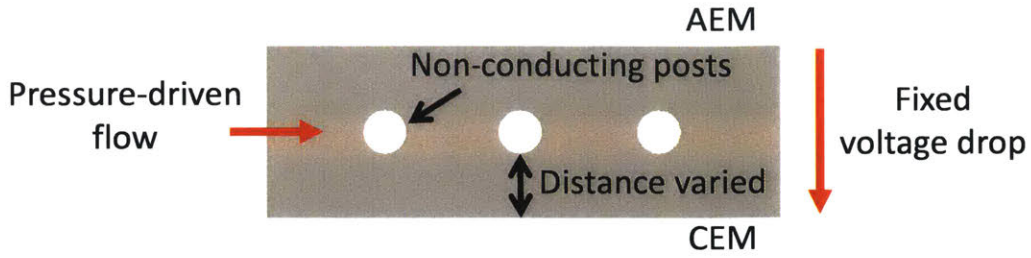

Figure 2.8 System setup for numerical simulation. Two red arrows indicate the directions of pressure-driven flow and of current at a fixed voltage drop. The dimensions of the channel are (width=1)×(length=3).

2.7.3 Explanation on enhancement of current efficiency (CE)

In general, lower current efficiency (CE) in electrodialysis results from 1) loss of permselectivity of ion exchange membrane (IEM), 2) water splitting in the diluate or concentrate streams, 3) shunt currents between electrodes, and 4) back diffusion of ions from the concentrate to the diluate streams. While the different CE values in our experiments may be difficult to be explained with the first three reasons listed above, back diffusion across the IEMs is a probable cause for the variation in CE.

Figure 2.9 shows the local concentration distribution of diffusion boundary layer near the IEM. For simplicity, we take two assumptions: 1) concentration distribution of diffusion boundary layer is linear, and 2) change in flowrate makes linearly proportional change to all the streamlines without considering wall effect (no slip condition).

Thickness of boundary layer (δ_{bl}) is a function of flow velocity (U_{HP}), current density (J), inter-membrane distance (D), and horizontal displacement (x). If only flow velocity is changed, the thickness of boundary layer can be expressed as,

$$\delta_{bl} = f(U_{HP}, I, D, x) \propto \frac{1}{U_{HP}^{1/3}}$$

Assume $U_{HP2} = 2U_{HP1}$, then

$$\delta_{bl\_HP2} = 0.79\delta_{bl\_HP1}$$

For conservation of salt removed in both cases,

$$\delta_{bl\_HP1} C_{w\_d\_HP1} U_{HP1} = \delta_{bl\_HP2} C_{w\_d\_HP2} U_{HP2}$$
$$C_{w\_d\_HP2} = 0.63 C_{w\_d\_HP1}$$

As a results, we finally approximate the concentration difference across the IEM,

$$\nabla C_{w\_HP2} < \nabla C_{w\_HP1}$$

It shows that a higher local flow velocity can reduce concentration difference across the IEM, thereby resulting in a higher CE (lowering back diffusion). This analysis also helps us to explain the limiting current enhancement for different local flow velocity in our results if limiting current density is decided not by maximum current flux through IEM, but by IEM wall concentration (C_{w_d}). (In another words, there should be a certain limit of concentration change on the IEM wall that can allow.)

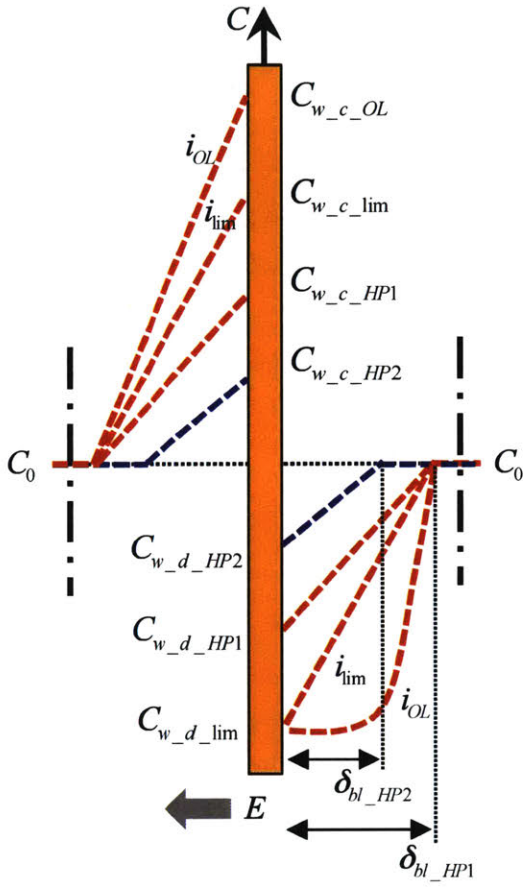

Figure 2.9 Local concentration distribution of diffusion boundary layer based on conventional model of ICP[17]. Three different regimes are presented: Ohmic ($i < i_{lim}$), limiting ($i \sim i_{lim}$), and overlimiting ($i_{OL} > i_{lim}$). C_0, C_{w_d}, and C_{w_c} indicate the bulk concentration, wall concentration of diluate and concentrate streams, respectively. We assume the average local flow velocity as U_{HP2} (blue dotted) ~ $2U_{HP1}$ (red dotted). We do not consider extended space charge layer or electric double layer to simply approximate the concentration difference across the membrane.

2.7.4 Pumping power calculation

The pumping power needed for a pressure-driven flow was calculated with the simulation data, to ensure that the benefits of mass transport enhancement from the spacers outweighs the increase in hydraulic resistance. The pumping power was calculated using the equation:

$$P_{pump} = Q\Delta P = A_{cross} v_{avg} \Delta P$$

where Q is the flowrate, ΔP is the pressure drop in the channel, A_{cross} is the cross-sectional area of the channel, and v_{avg} is the average velocity.

The pumping power was calculated for four cases presented in Figure 5 in the main manuscript, and the values are listed in Table 2.2 Pumping power calculation. The channel with posts requires much larger (~ 4x) pumping power than the other cases do. Next, we compare the pumping power to the electrical power required for desalination. A typical electrical power can be calculated using the data for "no post" case in the early limiting regime:

$$P_{elec} = IV = (0.018A)(0.2V) = 3.6\times10^{-3}W$$

where I is the current and V is the voltage across the channel. The electrical power is about 100 times greater than the pumping power required. Therefore, the contribution of pumping power to the total energy required is insignificant, and major improvement in total energy will be made through reduction in electrical energy consumption.

Table 2.2 Pumping power calculation

Case	A_{cross} (m^2)	v_{avg} (cm/s)	ΔP (Pascals)	P_{pump} (Watts)
No post	$2x10^{-5}$	1.19	17.7	$4.27x10^{-6}$
Posts at center (d'=0.5)	$2x10^{-5}$	1.19	84.0	$1.99x10^{-5}$
Posts near wall (d'=0.13)	$2x10^{-5}$	1.19	43.8	$1.04x10^{-5}$
Increased velocity	$2x10^{-5}$	1.25	19.0	$4.76x10^{-6}$
Reduced width	$1.9x10^{-5}$	1.25	20.5	$4.88x10^{-6}$

2.7.5 Overall energy efficiency (electricity & pumping)

Based on the calculation of pumping power in the previous section 2.7.4, the overall energy efficiencies were calculated by considering both electricity (to desalinate given feed water) and pumping power requirement (to generate hydraulic pressure). For fair comparison, we adopted EPIR (Energy Per Ion Removal), rather than overall power consumption in order to compare the effective energy uses for desalination since final salt removal ratio varies depending on the position of post structures. As shown in Figure 2.10, overall EPIR ranges roughly from 9 to 11.5 for different types of the channel configuration while the sole EPIR for pumping ranges less than 0.1 at most. As we showed the huge difference in the order of magnitude between electricity and pumping power, pumping power could be negligible even though the relative changing ratio of the pumping power exceed that of the electricity for different channels with post structures. Additionally, since the channel configuration that we present here is just placing lateral post arrays (apart from the membrane) to slightly redistribute the flow velocity near AEM/CEM, the incremental pressure drop should be much less than the other electrodialysis system with various obstacles, which dramatically alter flow streamlines for the purpose of generating turbulence. Therefore, we can conclude that local flow redistribution near AEM/CEM by placing post structure arrays facilitate the ion transport and thus enhance the overall energy efficiency for desalination much outweighing the penalties from additional pumping power requirement.

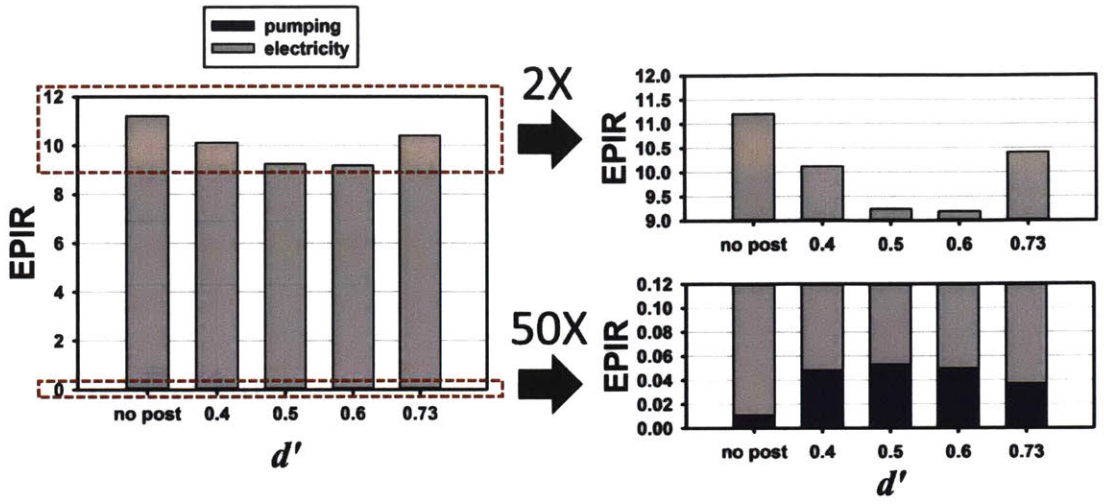

Figure 2.10 Evaluation of overall EPIR (Energy Per Ion Removal) for different channel configurations with various *d'*. Overall EPIR is calculated by summation of specific electricity (to desalinate feed) and pumping power (to generate hydraulic pressure). Constant current (I=0.02A) is applied, and the cases having less overall EPIR than the control (no post) are considered.

2.8 References

[1] A.A. Sonin, R.F. Probstein, A hydrodynamic theory of desalination by electrodialysis, Desalination, 5 (1968) 293-329.

[2] R.F. Probstein, Physicochemical hydrodynamics: an introduction, John Wiley & Sons, 2005.

[3] A.E. Yaroshchuk, Dielectric exclusion of ions from membranes, Advances in colloid and interface science, 85 (2000) 193-230.

[4] S.J. Kim, Y.-C. Wang, J.H. Lee, H. Jang, J. Han, Concentration polarization and nonlinear electrokinetic flow near a nanofluidic channel, Physical review letters, 99 (2007) 044501.

[5] R. Kwak, V.S. Pham, K.M. Lim, J. Han, Shear flow of an electrically charged fluid by ion concentration polarization: Scaling laws for electroconvective vortices, Physical Review Letters, 110 (2013) 114501.

[6] V. Chinaryan, M.Z. Bazant, I. Rubinstein, B. Zaltzman, Effect of concentration polarization on permselectivity, Physical Review E, 89 (2014) 012302.

[7] L.H. Olesen, M.Z. Bazant, H. Bruus, Strongly nonlinear dynamics of electrolytes in large ac voltages, Physical Review E, 82 (2010) 011501.

[8] C. Druzgalski, M. Andersen, A. Mani, Direct numerical simulation of electroconvective instability and hydrodynamic chaos near an ion-selective surface, Physics of Fluids (1994-present), 25 (2013) 110804.

[9] V.V. Nikonenko, N.D. Pismenskaya, E.I. Belova, P. Sistat, P. Huguet, G. Pourcelly, C. Larchet, Intensive current transfer in membrane systems: Modelling, mechanisms and application in electrodialysis, Advances in colloid and interface science, 160 (2010) 101-123.

[10] H. Strathmann, Preface, Membrane Science and Technology, 9 (2004) v-vi.

[11] M. Tedesco, H. Hamelers, P. Biesheuvel, Nernst-Planck transport theory for (reverse) electrodialysis: I. Effect of co-ion transport through the membranes, Journal of Membrane Science, 510 (2016) 370-381.

[12] K. Spiegler, Polarization at ion exchange membrane-solution interfaces, Desalination, 9 (1971) 367-385.

[13] P. Długołęcki, P. Ogonowski, S.J. Metz, M. Saakes, K. Nijmeijer, M. Wessling, On the resistances of membrane, diffusion boundary layer and double layer in ion exchange membrane transport, Journal of Membrane Science, 349 (2010) 369-379.

[14] P. Długołęcki, A. Gambier, K. Nijmeijer, M. Wessling, Practical potential of reverse electrodialysis as process for sustainable energy generation, Environmental science & technology, 43 (2009) 6888-6894.

[15] P. Długołęcki, B. Anet, S.J. Metz, K. Nijmeijer, M. Wessling, Transport limitations in ion exchange membranes at low salt concentrations, Journal of Membrane Science, 346 (2010) 163-171.

[16] M. Suss, S. Porada, X. Sun, P. Biesheuvel, J. Yoon, V. Presser, Water desalination via capacitive deionization: what is it and what can we expect from it?, Energy & Environmental Science, 8 (2015) 2296-2319.

[17] P. Biesheuvel, A. Van der Wal, Membrane capacitive deionization, Journal of Membrane Science, 346 (2010) 256-262.

[18] H. Strathmann, Electrodialysis, a mature technology with a multitude of new applications, Desalination, 264 (2010) 268-288.
[19] D.A. Vermaas, M. Saakes, K. Nijmeijer, Enhanced mixing in the diffusive boundary layer for energy generation in reverse electrodialysis, Journal of Membrane Science, 453 (2014) 312-319.
[20] S. Pawlowski, P. Sistat, J.G. Crespo, S. Velizarov, Mass transfer in reverse electrodialysis: flow entrance effects and diffusion boundary layer thickness, Journal of Membrane Science, 471 (2014) 72-83.
[21] A.A. Sonin, M.S. Isaacson, Optimization of flow design in forced flow electrochemical systems, with special application to electrodialysis, Industrial & Engineering Chemistry Process Design and Development, 13 (1974) 241-248.
[22] J. Balster, I. Pünt, D. Stamatialis, M. Wessling, Multi-layer spacer geometries with improved mass transport, Journal of Membrane Science, 282 (2006) 351-361.
[23] I.S. Kang, H.N. Chang, The effect of turbulence promoters on mass transfer—numerical analysis and flow visualization, International Journal of Heat and Mass Transfer, 25 (1982) 1167-1181.
[24] V. Vasil'eva, V. Shaposhnik, O. Grigorchuk, Local mass transfer during electrodialysis with ion-exchange membranes and spacers, Russian journal of electrochemistry, 37 (2001) 1164-1171.
[25] J.G.D. Tadimeti, V. Kurian, A. Chandra, S. Chattopadhyay, Corrugated membrane surfaces for effective ion transport in electrodialysis, Journal of Membrane Science, 499 (2016) 418-428.
[26] I.H. Kim, H.N. Chang, Experimental study of mass transfer around a turbulence promoter by the limiting current method, International Journal of Heat and Mass Transfer, 26 (1983) 1007-1016.
[27] D. Fischl, K. Hanson, R. Muller, C. Tobias, Mass transfer enhancement by small flow obstacles in electrochemical cells, Chemical engineering communications, 38 (1985) 191-207.
[28] J. Balster, D. Stamatialis, M. Wessling, Membrane with integrated spacer, Journal of Membrane Science, 360 (2010) 185-189.
[29] O. Grigorchuk, V. Vasil'eva, V. Shaposhnik, Local characteristics of mass transfer under electrodialysis demineralization, Desalination, 184 (2005) 431-438.
[30] V. Pérez-Herranz, J. Guiñón, J. García-Antón, Analysis of mass and momentum transfer in an annular electrodialysis cell in pulsed flow, Chemical engineering science, 54 (1999) 1667-1675.
[31] J. Balster, D. Stamatialis, M. Wessling, Towards spacer free electrodialysis, Journal of Membrane Science, 341 (2009) 131-138.
[32] R. Kwak, G. Guan, W.K. Peng, J. Han, Microscale electrodialysis: Concentration profiling and vortex visualization, Desalination, 308 (2013) 138-146.
[33] R. Kwak, V.S. Pham, B. Kim, L. Chen, J. Han, Enhanced Salt Removal by Unipolar Ion Conduction in Ion Concentration Polarization Desalination, Scientific Reports, 6 (2016) 25349.
[34] Y. Kim, W.S. Walker, D.F. Lawler, Electrodialysis with spacers: effects of variation and correlation of boundary layer thickness, Desalination, 274 (2011) 54-63.

[35] V.S. Pham, Z. Li, K.M. Lim, J.K. White, J. Han, Direct numerical simulation of electroconvective instability and hysteretic current-voltage response of a permselective membrane, Physical Review E, 86 (2012) 046310.
[36] S.V. Pham, H. Kwon, B. Kim, J.K. White, G. Lim, J. Han, Helical vortex formation in three-dimensional electrochemical systems with ion-selective membranes, Physical Review E, 93 (2016) 033114.
[37] B. Kim, R. Kwak, H.J. Kwon, V.S. Pham, M. Kim, B. Al-Anzi, G. Lim, J. Han, Purification of High Salinity Brine by Multi-Stage Ion Concentration Polarization Desalination, Scientific Reports, 6 (2016) 31850.
[38] R.D. Chambers, J.G. Santiago, Imaging and quantification of isotachophoresis zones using nonfocusing fluorescent tracers, Analytical chemistry, 81 (2009) 3022-3028.
[39] E.I. Belova, G.Y. Lopatkova, N.D. Pismenskaya, V.V. Nikonenko, C. Larchet, G. Pourcelly, Effect of anion-exchange membrane surface properties on mechanisms of overlimiting mass transfer, The Journal of Physical Chemistry B, 110 (2006) 13458-13469.
[40] V.V. Nikonenko, A.V. Kovalenko, M.K. Urtenov, N.D. Pismenskaya, J. Han, P. Sistat, G. Pourcelly, Desalination at overlimiting currents: State-of-the-art and perspectives, Desalination, 342 (2014) 85-106.
[41] V. Zabolotskii, N. Gnusin, V. Nikonenko, M.K. Urtenov, CONVECTIVE-DIFFUSION MODEL OF ELECTRODIALYTIC DESALINATION-DISTRIBUTION OF THE CONCENTRATION AND CURRENT-DENSITY, Soviet Electrochemistry, 21 (1985) 269-275.
[42] V. Shaposhnik, V. Vasil'eva, D. Praslov, Concentration fields of solutions under electrodialysis with ion-exchange membranes, Journal of Membrane Science, 101 (1995) 23-30.
[43] R. Kwak, Nonlinear ion concentration polarization: fundamentals and applications, in, Massachusetts Institute of Technology, 2013.
[44] R. Zhao, P. Biesheuvel, A. Van der Wal, Energy consumption and constant current operation in membrane capacitive deionization, Energy & Environmental Science, 5 (2012) 9520-9527.
[45] J.D. Seader, E.J. Henley, Separation process principles, (2011).
[46] M. Sadrzadeh, T. Mohammadi, Treatment of sea water using electrodialysis: Current efficiency evaluation, Desalination, 249 (2009) 279-285.
[47] K.N. Knust, D. Hlushkou, R.K. Anand, U. Tallarek, R.M. Crooks, Electrochemically mediated seawater desalination, Angewandte Chemie International Edition, 52 (2013) 8107-8110.

3. OPTIMIZATION OF SPACER DESIGN IN ELECTRODIALYSIS

3.1 Introduction

As described in Chapter 2, concentration polarization (CP) impedes mass transport by creating diffusion boundary layer (also known as ion depletion region) on the surface of membrane/electrode (*e.g.*, diluate channels of ED; see Figure 3.1a), which results in high electrical resistance [2], and thus increasing the overall electrical energy consumption [3,4]. Hence, concentration polarization (CP) is one of the main challenges in improving the efficiency of electrodialysis. There have been various efforts to reduce the CP effect and improve mass transport via "mixing promoters", such as spacers[3–6], corrugated membrane and electrode surfaces[7–11], ion conducting spacer[12,13], pulsating flow[14,15], and air bubbling[16]. Among these, spacers, such as the embedded microstructures in Chapter 2, are most commonly employed in practice to enhance the ED operation. The spacers reduce the electrical energy consumption by reducing the CP effect, but they also create additional hydrodynamic resistance and increase the pressure drop, requiring a larger pumping energy for a given flowrate. Therefore, an ideal spacer should be able to enhance the mass transport with a minimal increase in hydrodynamic resistance.

In this chapter, we continued our study of mass transport enhancement in an electrodialysis (ED) system by employing simple structures inside the diluate channel to spatially vary the local flow profile. These structures re-direct the flow to suppress (or expand) the diffusion boundary layers by having a fast (or slow) flow near the membranes and thus decrease (or increase) the electrical resistance (see Figure 3.1b). We performed a parametric study on the location and the size of the cylindrical posts, which are the structures of our choice, inside the diluate channel and studied its effect on the mass transport in microscopic detail. The study was

done through a direct numerical simulation by solving the coupled Navier-Stokes and Poisson-Nernst-Planck equations. The simulation enables a detailed analysis of ion concentration profile and flow velocity distribution as well as calculation of operating parameters; it also helps optimization of the structure design, which considers both enhanced electrical energy efficiency and increased hydrodynamic resistance by the spacers. This study presents a systematic model-based engineering approach for spacers in ED and other elecromembrane systems.

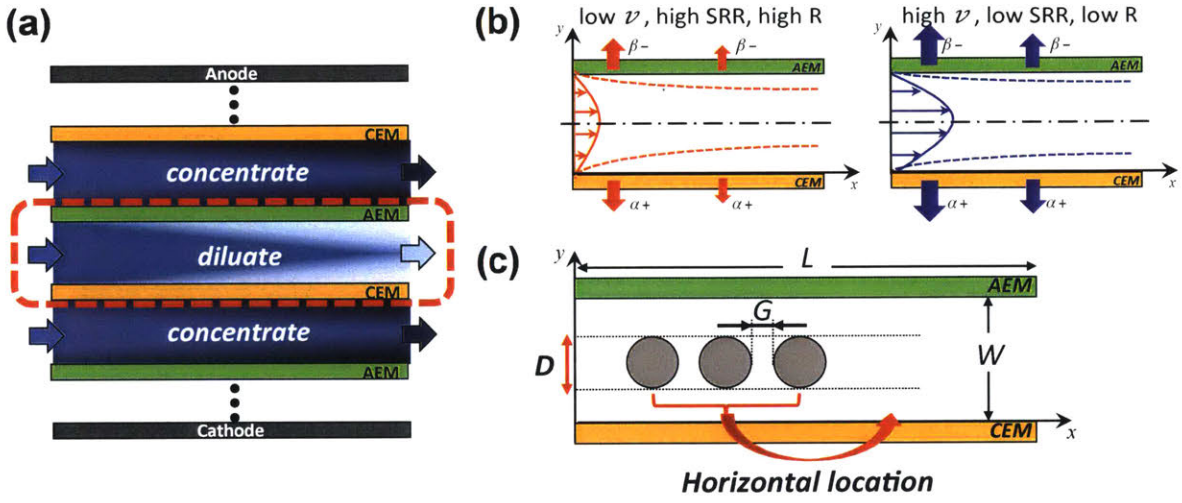

Figure 3.1 a) Schematic view of electrodialysis (ED). Color gradient indicates ion concentration profile. Electrical currents and constant forced flow are applied. Post structures are introduced in the red-boxed area whose details are described in b) and c). b) Velocity profile of the solution is drawn with a solid line, and the corresponding diffusion boundary layer for the solution of NaCl (α=Na, β=Cl) is drawn with a dotted line. The arrows represent the flux through the membrane. Blue on the right indicates a higher average velocity, compared to red on the left. A higher velocity results in lower salt removal ratio (SRR) but also a lower electrical resistance (R). C) Description of parameters in study. The first parameter studied was D, which represents the diameter of posts. G represents the shortest distance (or gap) between two adjacent posts. The ratio of D to G is kept constant for a set of study. The second parameter of study was horizontal location. This parameter was not quantified; instead, it was labeled as "location x", where x increases as the posts start farther from the inlet. L and represent the length and the width of the channel, respectively.

3.2 Design of study

3.2.1 System setup

The post structures (intended to be representatives of typical "mixing promoters" or spacers, used in previous studies and Chapter 2 of this thesis) were only considered inside the diluate channel since the ion depletion boundary and the consequent amplification of electrical resistance is only found in diluate channels. The two parameters studied in this Chapter are the post diameter and the horizontal location of partial posts. As illustrated in Figure 3.1c. D represents the diameter of posts, and G represents the shortest distance (or gap) between two adjacent posts. The ratio of D to G is kept constant for a set of study. For the partial post study, the horizontal location of posts was not quantified; instead, it was labeled with the coverage and a number "x", where x increases as the posts start farther from the inlet (*i.e.*, "Third 1" indicates a channel where the posts were placed in the first third of the channel; "half 2" indicates a channel where the posts were placed in the second half of the channel).

In the post size study, the ratio of the channel width to the length is 1:6. The solution consisted of 10mM potassium chloride. The D to G ratio was fixed to 0.5 for all post sizes. The feed velocity was kept constant for all cases, thus keeping the flowrate constant.

In the location of partial post study, the ratio of the channel width to the length is 1:20. The solution consisted of 1mM sodium chloride. The post diameter was 25% of the channel width, and the D to G ratio was fixed to 0.5 for all post sizes.

3.2.2 Numerical modeling

Simulation results were obtained by a direct numerical simulation, which was developed by Pham *et al.* [35] The simulation relies on the direct, coupled solution of the full set of Poisson-Nernst-Planck and Navier-Stokes equations. In this work, we used a 2D modeling of ED systems, while a full 3D modeling of electromembrane systems have been reported recently[36]. Detailed method and simulation setup are the same as described in Chapter 2.

3.3 Optimization of post location

This part of the study is to optimize the design of cylindrical posts to achieve the minimum energy consumption. Structures (or spacers) inside ED channels affect the energy consumption of the process in two ways. First, they modulate, and often enhance, the degree of mass transport by modifying the local flow distribution and the resulting ion concentration profile; as a result, they reduce the electrical energy required to achieve the same salt removal. On the other hand, structures inside the channel create additional fluidic resistance and thus increase the pumping energy required for a given flowrate. Figure 3.2a shows that larger posts result in a greater current enhancement by creating a faster flow near the membranes and further suppressing the depletion boundary layer. However, the larger posts also create more hydrodynamic resistance, indicated by the higher pressure drop in Figure 3.2b.

In order to quantify the effects on mass transport and fluidic resistance, the electrical ($EPIR_e$) and pumping ($EPIR_p$) energy per each ion removal was calculated, as described below:

$$EPIR_e = \frac{IV}{Q_{diluate}\left(C_0 - C_{diluate}\right)}$$

$$EPIR_p = \frac{v_{avg} A_{cross} \Delta P}{Q_{diluate}(C_0 - C_{diluate})}$$

The total energy per ion removal ($EPIR_{total}$), which can be obtained by summing these two energy terms, is used to find the optimal post size. In general, as the post diameter increases, the electrical energy is enhanced, and the maximum achievable salt removal increases. However, for very large posts (D = 0.9), the electrical energy efficiency is worsened (Figure 3.3a). For total energy in Figure 3.3c, similar trend is observed with a worse energy efficiency for very large posts (D = 0.9) due to the large pumping power required. Therefore, the optimal post size should be around 0.5, depending on the target salt removal. The next step is to study the effect of post frequency, or post-to-post distance, and combine the results from the two parameters to determine the most energy efficient post design.

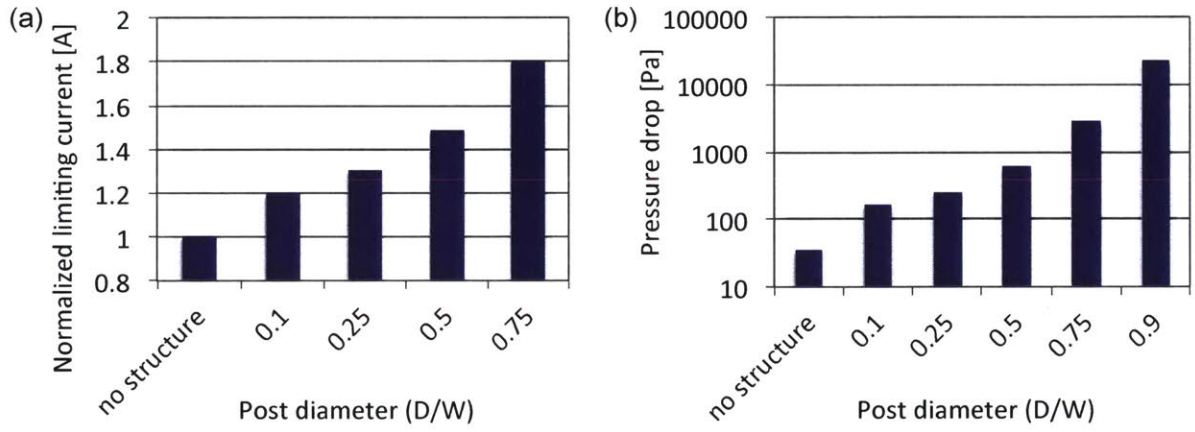

Figure 3.2 Effect of post diameter on mass transport and hydrodynamic resistance. The post size is expressed with the ratio of post diameter to channel width. The average velocity was kept constant for all cases. (a) Comparison of limiting current for various post sizes. The limiting current is normalized to the limiting current value of "no structure" design. In the results for the diameter of 0.9, there was no clear limiting regime and thus the limiting current was not calculated. (b) Pressure drop for various post sizes.

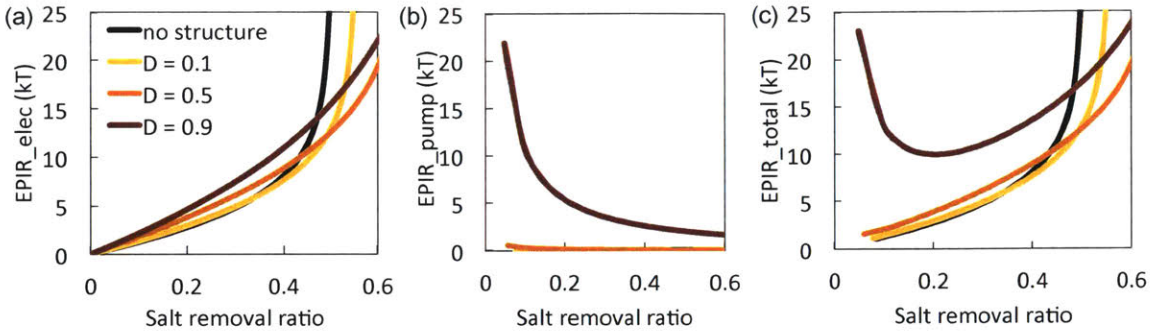

Figure 3.3 Energy per ion removal (EPIR) calculated for (a) electrical energy and (b) pumping energy, and (c) total energy as a function of salt removal ratio (SRR). D is the post diameter and is expressed as a fraction of the channel width

3.4 Optimization of post location

In most ED systems in practice, the spacers are placed throughout the entire length of the channel in order to enhance the mass transport. However, as the local concentration of ions and the resulting current distribution vary along the length of the channel, the optimal location or frequency of the structures may vary. This study was conducted to find whether posts at specific locations (along the channel length) enhance the mass transport more efficiently than those placed in other locations. The current voltage response was generated and the limiting current density was calculated for channels with no posts ("no structure"), posts throughout the entire channel ("full structure"), posts in a third of channel ("third x"), and posts in a half of channel ("half x"). Figure 3.4 shows that partial posts at certain locations result in a higher current enhancement, indicated by the higher limiting current density, than other designs.

To understand the reason for the different degree of current enhancement, the current distribution along the channel length was plotted, as shown in Figure 3.5. In general, the peaks in the current for the channel with structures coincides with the location of the posts as the posts

suppress the depletion boundary layer, reduce the electrical resistance, and thus enhance the local mass transport. In Figure 3.5a, "full structure" design provides great current enhancement in the beginning of the channel, but the current towards the channel outlet seems to return to the level of "no structure" design. However, this comparable level of current towards the outlet still indicates enhancement since the ion concentration for "full structure" is lower, which resulted from the increased mass transport in the earlier part of the channel. Figure 3.5b and c, the partial post in the beginning of the channel exhibits the same current enhancement as the earlier part of the "full structure" design, but this enhancement is counterbalanced by a reduced mass transport in the later part of the channel. When the partial posts are located at the end of the channel, the earlier part has the same current profile as "no structure" and the post region has a significant current enhancement, resulting in overall the highest current enhancement among the partial post designs.

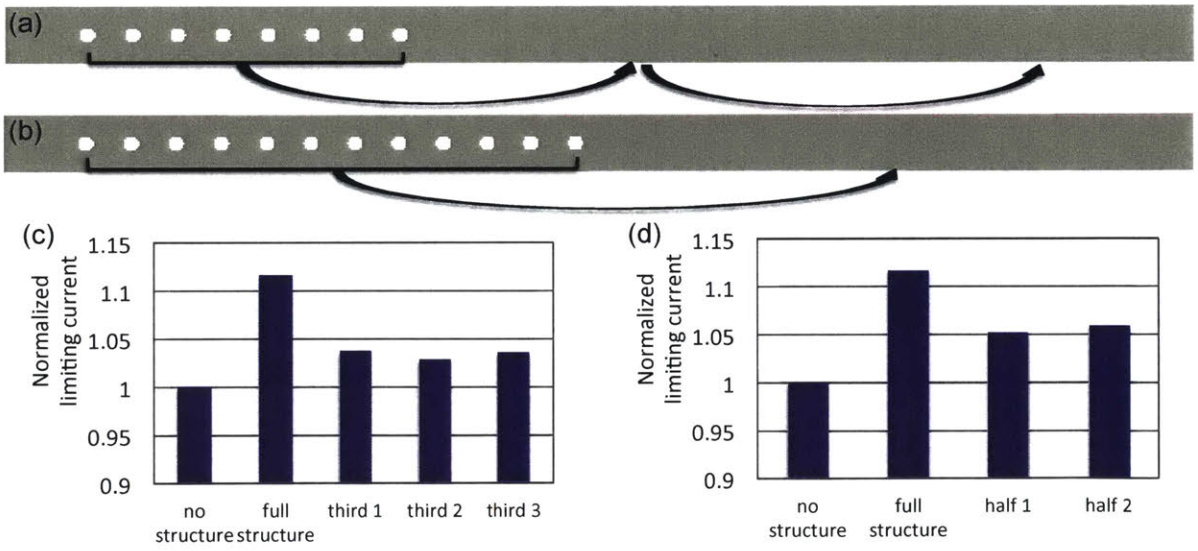

Figure 3.4 (a) and (b) show the channels where 1/3 and 1/2 of the channel is filled with the posts. The arrows indicate that the posts were shifted to the indicated locations for each set of data. In (c) and (d), the limiting current for each design is normalized to the limiting current value of "no structure" case. "full structure" denotes that the posts were placed in the entire channel; "third x" or "half x" denotes that the structures were placed in a third or half of the

channel, with a lower x indicating structures closer to the inlet. The channel length is 20 times the width. The post diameter is 25% of the channel width. The solution used for the study is 1mM NaCl. The average velocity was kept constant for all cases.

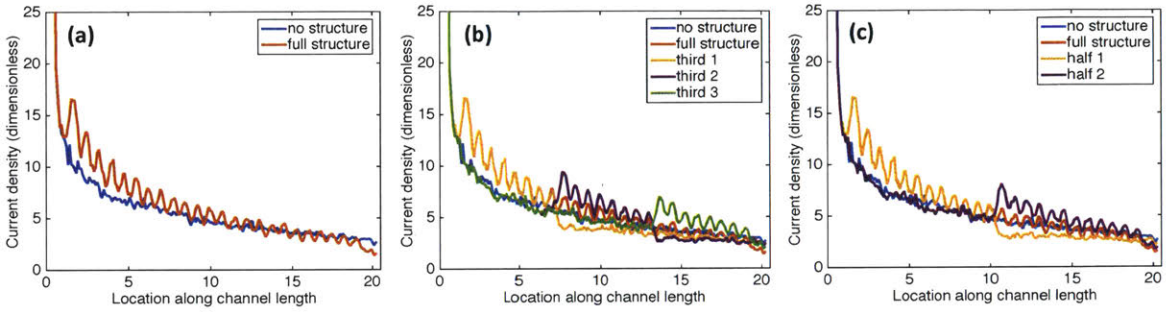

Figure 3.5 Current distribution over the channel length. Comparisons were made to show the effect of (a) full structure, (b) third-full structures, and (c) half-full structures. The data was taken for the same voltage drop in the late limiting regime.

3.5 Conclusion

In this work, we studied the effect of post size and partial posts on the ED performance. From the post size study, we found that the large posts increase the achievable salt removal in a given system by increasing the limiting current density. Yet, the increasing post size results in an increased hydrodynamic pressure and pumping power, which lead to an increase in the total energy consumption. In the case of extremely large posts, in addition to the lowered pumping energy efficiency, the electrical energy efficiency is worsened because the large posts hinder the ionic path. Therefore, the target salt removal should be considered when determining the optimal post size.

From the partial post study, we found that the current enhancement was generally proportional to the portion of the channel covered by the post, and the enhancement is less sensitive to the location of the partial posts. The results showed that posts near the inlet may be

more effective because majority of current is conducted in this region. The posts at the end of the channel may also be effective because the enhancement in this region does not negatively affect the mass transport in the earlier part, whereas the enhancement in the early part of channel is offset by the low current in the later part of the channel. Based on these findings, a channel design with posts near the inlet and the outlet should be studied in the following study. Furthermore, studies with larger posts or a faster flow can magnify the current enhancement by posts in general and making the difference between the post locations more pronounced.

3.6 References

[1] P. Długołęcki, P. Ogonowski, S.J. Metz, M. Saakes, K. Nijmeijer, M. Wessling, On the resistances of membrane, diffusion boundary layer and double layer in ion exchange membrane transport, J. Memb. Sci. 349 (2010) 369–379. doi:10.1016/j.memsci.2009.11.069.

[2] P. Długołęcki, A. Gambier, K. Nijmeijer, M. Wessling, Practical potential of reverse electrodialysis as process for sustainable energy generation, Environ. Sci. Technol. 43 (2009) 6888–6894. doi:10.1021/es9009635.

[3] H. Strathmann, Electrodialysis, a mature technology with a multitude of new applications, Desalination. 264 (2010) 268–288. doi:10.1016/j.desal.2010.04.069.

[4] A.A. Sonin, M.S. Isaacson, Optimization of flow design in forced flow electrochemical systems, with special application to electrodialysis, Ind. Eng. Chem. Process Des. Dev. 13 (1974) 241–248. doi:10.1021/i260051a009.

[5] J. Balster, I. Pünt, D.F. Stamatialis, M. Wessling, Multi-layer spacer geometries with improved mass transport, J. Memb. Sci. 282 (2006) 351–361. doi:10.1016/j.memsci.2006.05.039.

[6] In Seok Kang, Ho Nam Chang, The effect of turbulence promoters on mass transfer—numerical analysis and flow visualization, Int. J. Heat Mass Transf. 25 (1982) 1167–1181. doi:10.1016/0017-9310(82)90211-3.

[7] V.I. Vasil'eva, V.A. Shaposhnik, O. V Grigorchuk, Local mass transfer during electrodialysis with ion-exchange membranes and spacers, Russ. J. Electrochem. 37 (2001) 1164–1171.

[8] J.G.D. Tadimeti, V. Kurian, A. Chandra, S. Chattopadhyay, Corrugated membrane surfaces for effective ion transport in electrodialysis, J. Memb. Sci. 499 (2016) 418–428. doi:10.1016/j.memsci.2015.11.001.

[9] D.H. Kim, I.H. Kim, H.N. Chang, Experimental study of mass transfer around a turbulence promoter by the limiting current method, Int. J. Heat Mass Transf. 26 (1983) 1007–1016. doi:10.1016/S0017-9310(83)80125-2.

[10] D.S. FISCHL, K.J. HANSON, R.H. MULLER, C.W. TOBIAS, Mass Transfer Enhancement By Small Flow Obstacles in Electrochemical Cells, Chem. Eng. Commun. 38 (1985) 191–207. doi:10.1080/00986448508911306.

[11] J. Balster, D.F. Stamatialis, M. Wessling, Membrane with integrated spacer, J. Memb. Sci. 360 (2010) 185–189. doi:10.1016/j.memsci.2010.05.011.

[12] O.V. Grigorchuk, V.I. Vasil'eva, V.A. Shaposhnik, Local characteristics of mass transfer under electrodialysis demineralization, Desalination. 184 (2005) 431–438. doi:10.1016/j.desal.2005.03.048.

[13] J.M. Ortiz, E. Expósito, F. Gallud, V. García-García, V. Montiel, A. Aldaz, Desalination of underground brackish waters using an electrodialysis system powered directly by photovoltaic energy, Sol. Energy Mater. Sol. Cells. 92 (2008) 1677–1688. doi:10.1016/j.solmat.2008.07.020.

[14] N.A. Mishchuk, L.K. Koopal, F. Gonzalez-Caballero, Intensification of electrodialysis by applying a non-stationary electric field, Colloids Surfaces A Physicochem. Eng. Asp. 176 (2001) 195–212. doi:10.1016/S0927-7757(00)00568-9.

[15] J. Balster, D.F. Stamatialis, M. Wessling, Towards spacer free electrodialysis, J. Memb. Sci. 341 (2009) 131–138. doi:10.1016/j.memsci.2009.05.048.

4. TECHNO-ECONOMIC ANALYSIS OF ION CONCENTRATION POLARIZATION DESLAINATION FOR HIGH SALINITY DESALINATION APPLICATIONS

4.1 Introduction

Desalination of saline water in the range of brackish and seawater has advanced greatly over the past few decades with the development of membrane desalination technologies. Reverse osmosis (RO), the state-of-the-art membrane desalination technology, has reached energy consumption (~2kWh/m^3) that is only twice of the theoretical minimum (1.06kWh/m^3) [1], [1][1and electrodialysis, an electromembrane desalination technology, has achieved the lowest energy consumption (1.65kWh/m^3) for seawater desalination [2]. While the brackish and seawater desalination has enjoyed a remarkable progress, desalination of high salinity brine with salinity above seawater level (35,000 ppm) has been a continuing challenge with few options for treatment. In fact, the need for highly saline brine desalination is growing as the volume of brine generation increases. Two major sources of the brine are concentrate from desalination processes and produced water from shale gas extraction. Increasing desalination capacity has resulted in large volume of brine generation [3–5]. Moreover, efficient desalination operation and higher recovery of product have created more concentrated brine (50,000 – 85,000 ppm) [6], which makes treatment more challenging. In shale gas industry, management of produced water (8000 – 360,000 ppm) is one of the biggest challenges for economical and environmental reasons [7–9].

Current methods of brine management include surface discharge, solar evaporation, underground injection, and internal reuse in hydraulic fracturing for the case of produced water. Surface discharge is the most rudimentary method of disposal with minimal costs involved. However, the discharged brine can disrupt the ecosystem by increasing the local salinity of the

surface water and by contaminating the surface water with toxic chemicals added during desalination or hydraulic fracturing (*e.g.*, anti-foulants, anti-scalants, surfactants, etc.) [10–13]. Solar evaporation involves evaporating brine from large, shallow ponds using natural solar energy and removing residual solid for disposal [14]. Evaporation ponds are easy to construct and to maintain but require large footprint, which raises capital cost, and may cause environmental issues in case of brine leakage [15,16]. Underground injection is the brine management practice employed to dispose majority of produced water from shale gas operation [17]. Underground injection is limited by the number of available disposal wells and the transportation from produced water generation sites to wells [18]. To reduce the brine volume in the shale gas industry, reuse of produced water has become increasingly popular [7]. Internal reuse of produced water can reduce the demand for injection wells and freshwater, but can hurt the efficiency of the hydraulic fracturing process due to the high concentration of dissolved ions and other chemicals [19,20]. Reuse needs to be accompanied with another disposal method, for the reused produce water will eventually need to be disposed when the reuse demand becomes low as the shale gas formations mature [7,9,19]. As reviewed here, the current brine management methods are not sustainable to treat an increasing volume of high salinity brine. Therefore, desalination should be employed to reduce the volume of brine that needs to be managed by solar evaporation or underground injection.

Current desalination technologies for potential treatment of high salinity brine include reverse osmosis, thermal desalination technologies, such as multi-stage flash, multi-effect distillation, and mechanical vapor compression, and membrane distillation. Reverse osmosis is the most cost efficient desalination technology to treat saline water with up to 35,000 ppm TDS [21,22]. However, for high salinity feed, the RO membrane modules cannot withstand the

hydraulic pressure needed to overcome the large osmotic pressure, which arises from the large salinity difference between the feed and the permeate [21,22]. For this reason, high salinity brine is typically treated with thermal technologies, such as multi-stage flash (MSF) and multi-effect distillation (MED). These thermal desalination technologies are energy intensive (8 – 30 kWh/m^3), and require relatively high investment cost and large footprint, compared to membrane desalination [23,24]. For efficient operation, thermal desalination plants are typically built next to power plants to utilize the heat generated from these plants, and thus these plants are less mobile and scalable [7]. Mechanical vapor compression (MVC) is the next generation thermal desalination technology that is more energy efficient than MSF and MED. The energy consumption for MVC is 10.4 – 13.6 kWh/m^3 for treatment of brine with salinity beyond seawater level (38,000 – 260,000 ppm) [25–28]. MVC is modular in design, and thus involve lower capital cost and more scalable, compared to MSF and MED [29]. Membrane distillation (MD) is a relatively new technology and is a thermally driven membrane desalination process. Its advantages are the use of low-grade heat source and the low sensitivity of performance to the feed salinity, which makes the process appealing for high salinity brine treatment [30,31]. An MD with heat recovery can achieve thermal energy consumption of 40 kWh/m^3 for seawater desalination [32].

Electromembrane desalination, such as electrodialysis (ED), exhibits characteristics that can be particularly appealing for high salinity brine desalination. Since these processes are electrically driven, highly saline water will increase the ion conductance, making the process more favorable [33,34]. In addition, electromembrane desalination enables partial desalination because salt removal in the product stream can be altered. Brine treatment by ED has been demonstrated in several studies [35–40]. Ion concentration polarization (ICP) desalination is an

electromembrane desalination technology that has been developed by Han Group our group [41,42]. Compared to electrodialysis, ICP desalination can remove salt (*i.e.*, sodium chloride) more efficiently at a given current [41]. The system was engineered to operate more energy efficiently, and its potential application was identified to be in partial desalination of high salinity brine [42,43].

In this work, we performed a techno-economic analysis to evaluate the economic feasibility of ICP desalination for seawater desalination and desalination brine management. Based on experimental data from a fixed device configuration, we built a model to estimate the energy consumption and the membrane area for a given set of operating parameters. Using this model, we optimized the operating conditions for the minimum water cost, given the feed and the product concentrations. We calculated the water cost for two applications: partial desalination of brine to seawater level, at which reverse osmosis can operate efficiently, and concentration of seawater desalination brine for salt production. The cost of water produced by ICP desalination was compared with the cost of water produced by other desalination technologies to help determine the competitiveness of ICP desalination.

4.2 Methods

4.2.1 Experimental

The experimental data was generated with a lab-scale ICP desalination device, whose configuration, fabrication, and operation were described and demonstrated in a previous work [43]. The channel dimensions were 2.5mm in depth (*i.e.*, effective intermembrane distance), 8mm in effective width, and 30cm in length. The flowrate ratio of diluate to concentrate to feed

stream was 1:1:2, and the overall recovery of the diluate was 50%. Varied parameters included feed salinity, salt removal ratio (SRR; defined below), and flow velocity.

$$SRR = \frac{C_{\text{feed}} - C_{\text{diluate}}}{C_{\text{feed}}}$$

Since high salinity desalination applications of ICP desalination were considered, the tested feed salinity ranged from 35,000 ppm to 100,000 ppm of sodium chloride. The ranges of salt removal and the flow velocity were 10% – 90% and 0.25 – 3 mm/s, respectively. The current and voltage for each experiment were consequently varied to achieve the target SRR for the given feed salinity and flow velocity.

4.2.2 Estimation of electrical energy consumption

In order to estimate electrical energy consumption for any given set of feed salinity, SRR, and flow velocity, a relation must be built based on the experimental data. From the measured current and voltage values, the power and the electrical energy consumption were calculated, and the relation between the current and the power consumption were fitted to an equation. To estimate current for a given set of feed salinity, SRR, and flow velocity, another fitting was done to first estimate current efficiency (CE) as a function of SRR and flow velocity; the current efficiency was then used to calculate the corresponding current. The relation between current and current efficiency is shown in the equation below.

$$CE = \frac{zFQ_{\text{diluate}}\left(C_{\text{feed}} - C_{\text{diluate}}\right)}{I}$$

4.2.3 Optimal water cost calculation

Water cost was calculated with a simple cost model that consists of operating and capital costs. This method is a well-established method for cost analysis of electrodialysis and ICP desalination [37,42–44]. Electricity and pumping energies were used to calculate the operating cost. Total membrane area was utilized to estimate the capital cost since the capital cost of electrodialysis, which is very similar to ICP desalination in configuration and operation, depends strongly on the total membrane area [45]. Equations below were used to calculate the electricity, pumping, and capital costs. The water cost was obtained by summing the operating and capital costs and expressed in US dollars per cubic meter of feed solution. Parameters used in the cost analysis are listed in Table 1. The value of capital cost per unit membrane area (K_Q) was approximated with the K_Q values for ED and ICP desalination as guides [43,44,46]. More specifically, the value of K_Q for ED were \$480/m^2-membrane in McGovern *et al.* [44] and \$600/m^2-membrane from an industry quote [47]; the value of K_Q for ICP desalination was assumed to be 25% – 50% higher than that for ED since ICP desalination is a new technology and thus requires more capital for development. To obtain the optimal water cost for a given set of feed and product salinities, the water cost was calculated over a range of flow velocity (and resulting current), and the optimal operating conditions that result in the minimum water cost were determined.

$$\text{Electricity Cost } (\$/\text{m}^3) = \frac{I \times V}{Q} \times K_E = \frac{P}{Q} \times K_E$$

$$\text{Pumping Cost}(\$/\text{m}^3) = \frac{\text{Pumping Power}}{\text{Feed Flowrate per Cell}} \times N_{cell} \times K_E = \frac{12\mu QL}{wd^3} \times \frac{Q_{total}}{Q_{cell}} \times K_E$$

$$\text{Capital Cost } (\$/\text{m}^3) = \frac{\text{Used Membrane Cost } (\$)}{\text{Output Flow Volume per Life } (\text{m}^3)} \times \text{Anualized Factor}$$

$$= \frac{A_\text{m} \times K_\text{Q}}{Q \times T} \frac{(1+R)^T - 1}{T \times R}$$

Table 4.1 Variables and parameters for cost analysis

Description	Symbol	Value
I	Current	
V	Voltage	
Q	Feed flowrate	
K_E	Electricity rate	10 ¢/kWh
μ	Dynamic viscosity	0.00972 g/cm·s
L	Cell length	30 cm
w	Cell width (effective)	8 mm
d	Cell depth (*i.e.*, intermembrane distance)	2.5 mm
Q_{total}	Total flowrate	
Q_{cell}	Flowrate per cell	
A_m	Total membrane area	
K_Q	Capital cost per unit membrane area	\$ 750 /m^2
R	Cost of capital	10%
T	Life time of equipment	20 years

4.2.4 RO cost model

The cost of reverse osmosis (RO) was calculated using a model and configuration that was described in previous works [27,48,49]. This section of the thesis was done in collaboration with Kishor Nayar (Department of Mechanical Engineering at Massachusetts Institute of Technology).

The RO configuration selected (shown in Figure 4.1) was a conventional 1-stage arrangement with a circulation pump, a high pressure pump, a pressure exchanger and a booster pump. The RO model used seawater thermophysical property correlations developed by Nayar *et al.* [50] to determine seawater osmotic pressure and density. The pinch pressure in the RO module (i.e. difference between hydraulic pressure and peak module osmotic pressure) was

assumed to be 10 bar with a pressure loss of 2 bar assumed in the RO module. The pumps were assumed to have an efficiency of 0.8 while the pressure exchanger was assumed to have an efficiency of 0.96 [49]. The energy requirements were determined by basic equations for pump work, described in Thiel *et al.* [27] and Nayar *et al.* [48]. The capital cost of the RO system was assumed to scale as \$1206 day/m^3 of RO water production. This value was an average value based on seawater RO plants from around the world, sourced from DesalData [51]. The capital cost was annualized using the same factor described in Section 4.2.3.

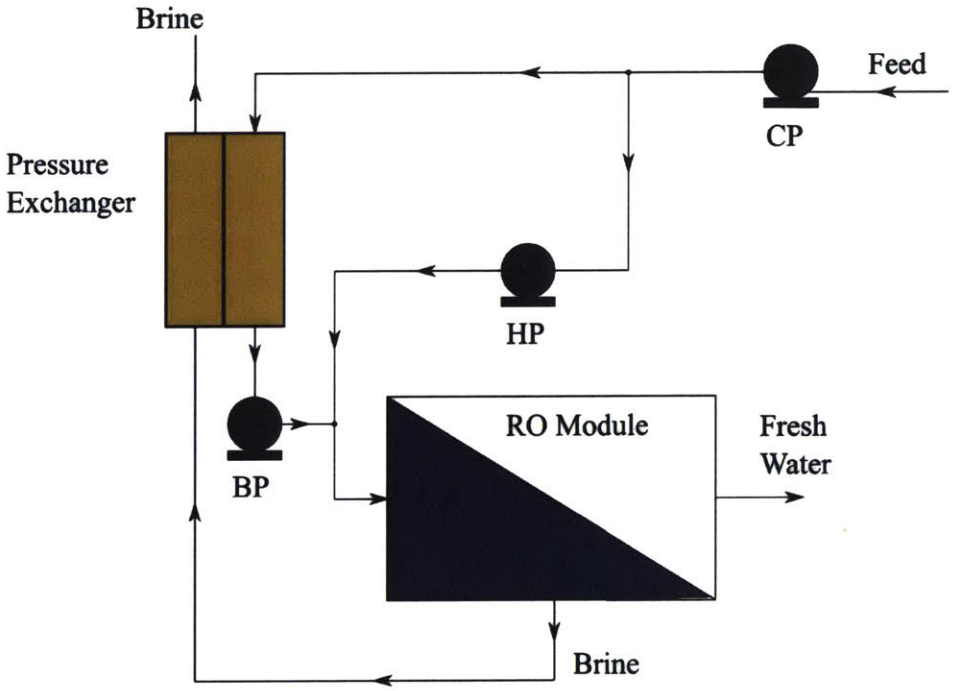

Figure 4.1 Configuration of single-stage seawater RO plant (CP – circulation pump, HP – high pressure pump and BP – booster pump)

4.3 Estimation of electrical energy consumption

ICP desalination with high salinity brine (salinity ≥ 35,000 ppm) was performed with a fixed device configuration (*i.e.*, fixed channel dimensions, cell numbers, and recovery ratio). Feed salinity, salt removal ratio, and flow velocity were varied, and the resulting current and potential drop, from which the power consumption was calculated, were measured. The power consumption was plotted as a function of the applied current over a variety of operating parameters. The results show a power relation between the current and the power consumption (Figure 4.2), which is described by $y = 0.416x^{1.86}$ with $r^2 = 0.985$, where y = power consumption in Watts and x = current in Ampere. The fitting equation indicates that the relation is similar to the Ohm's law ($P = I^2R$) with a constant resistance R in the system. The total electrical resistance in the ICP desalination system includes contributions from the membrane, the bulk solution, the diffusion boundary layer, and the electrical double layer [33]. At high salinity above seawater level, the solution is highly conducting, so the membrane resistance becomes the main contributor to the total resistance [33]. Therefore, the total resistance at high salinity is almost constant because the membrane resistance sets a lower limit for the resistance. The value of the resistance was calculated to be 12 Ωcm^2 from the fitting equation and falls in the same order of magnitude as the reported values for the membrane [43,52].

To estimate the electrical energy consumption from the power relation, the current must be calculated for the given operating conditions. The current is generally proportional to the rate of ion removal, but we must consider the current efficiency (CE), which represents how much of the total current is utilized for ion removal, as the CE varies with operating conditions. The expression for current efficiency is described as

$$CE = \frac{zFQ_{\text{diluate}}\left(C_{\text{feed}} - C_{\text{diluate}}\right)}{I}$$

where z is ion valence, F is Faraday's constant, Q_{diluate} is volumetric flowrate of product stream, C_{feed} and C_{diluate} are feed and product concentration, and I is total current. The *CE* trends as a function of the salt removal ratio and flow velocity are shown in Figure 4.3a and b, respectively. When other parameters are set constant, the *CE* decreases with the salt removal ratio because higher ion removal requires a higher current and thus thicker ion depletion layers, which increase the degree of back diffusion of ions from the concentrate to the diluate streams [53]. The *CE* exhibits a quadratic relation with linear flow velocity and peaks around 2 mm/s. This trend is a result of two effects: first, a high flow velocity reduces the thickness of ion depletion layers and enhances the current efficiency; second, a high flow velocity requires a high ion removal rate to achieve the same salt removal ratio, leading to a high current and increased back diffusion. At a low flow velocity, the suppression of depletion layer is the dominant effect, while the high current worsens the *CE* at a high flow velocity. The combined effect of the salt removal ratio and the flow velocity on the *CE* was considered to express the *CE* as a function of the *SRR* and the flow velocity. In Figure 4.3c, the fitted model was plotted as a surface, and the experimental data were plotted as dots. Using this model, we can estimate the *CE* for a given set of feed salinity, product salinity, and flow velocity. The *CE* was used to calculate the required current and the resulting power and energy consumption. The accuracy of the current estimation was evaluated by calculating the absolute percentage deviation (equation below) of the estimated current from the measured current for the data set (Figure 4.3d). The average absolute percentage deviation was 9.5%.

$$\text{Absolute percentage deviation} = \frac{|I_{\text{estimated}} - I_{\text{measured}}|}{I_{\text{measured}}} \times 100\%$$

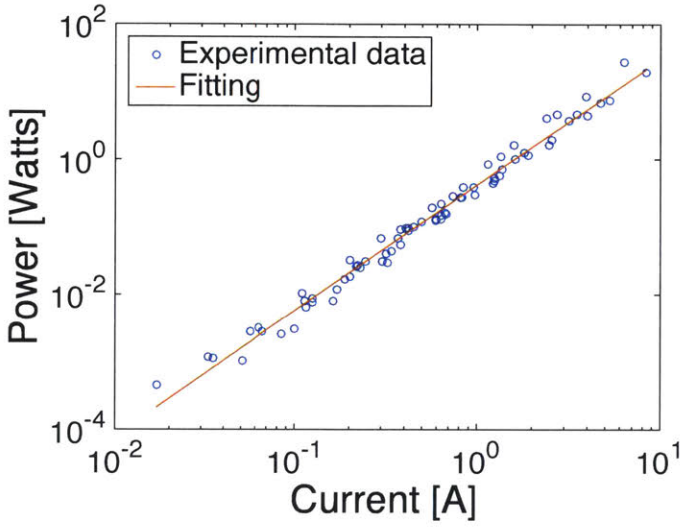

Figure 4.2 Power relation between power consumption and applied current in ICP desalination. The experimental data were generated with a fixed device configuration over various parameters (*e.g.*, feed salinity, salt removal ratio, and flow velocity). The fitted equation is in the form of $y = ax^b$.

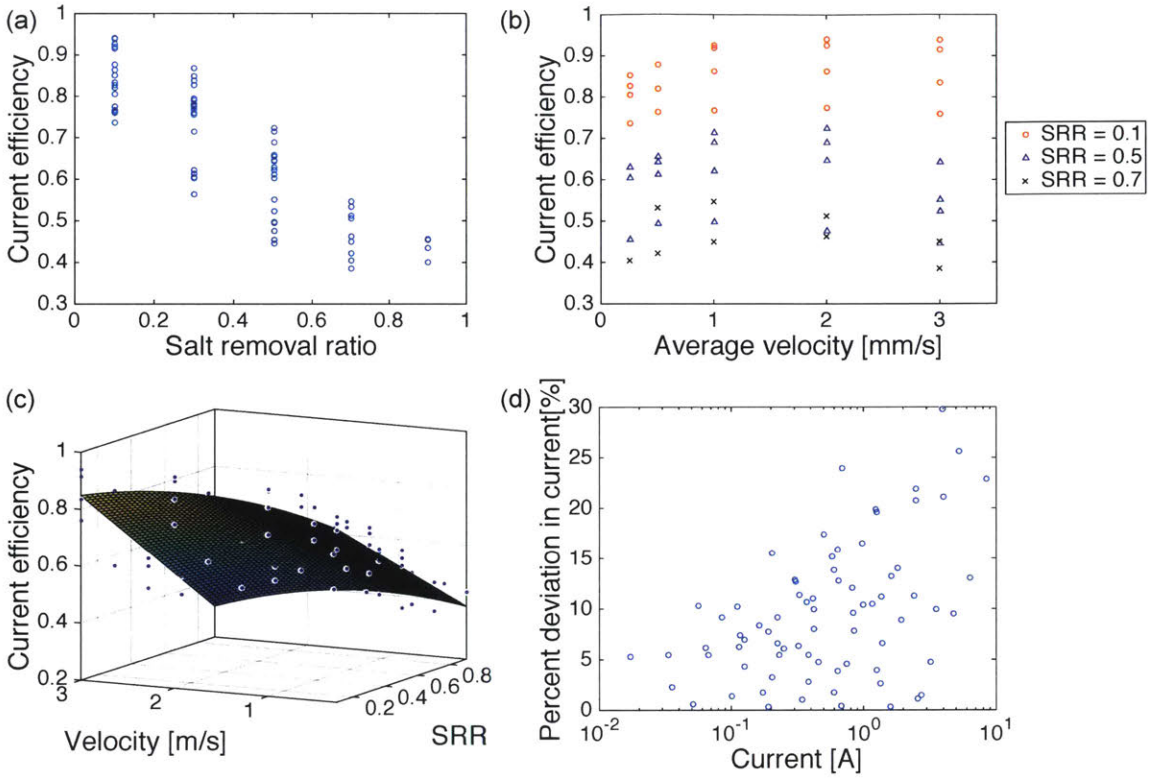

Figure 4.3 Current efficiency as a function of salt removal ratio (SRR) and average flow velocity. The experimental data were generated with a fixed device configuration. (a) Current efficiency as a function of SRR, for a range of feed salinity and flow velocity, follows a linear relation. (b) Current efficiency as a function of average flow velocity, for a range of SRR and flow velocity, follows a quadratic relation. Only the data for 10%, 50%, and 70% were plotted to easily show the quadratic trend. (c) Current efficiency was plotted as a function of SRR and flow velocity, and the data was fitted to a polynomial surface. (d) Using the CE fitting model, the current was estimated for given feed salinity, SRR, and flow velocity. The (absolute) percent deviation of the estimated current from the measured current was plotted.

4.4 Application 1: Partial desalination of high salinity brine to seawater level

The first application scenario of ICP desalination is partial desalination of high salinity brine to the typical seawater level (35,000 ppm). Various sources of brine have salinities higher than 35,000 ppm include: high salinity seawater in the the Arabian Gulf (~50,000 ppm), concentrate from RO/MSF desalination plants (~70,000 ppm), and produced water from oil/gas extraction processes. As discussed in the Introduction, there are limited options for treatment of this brine. Here, we performed a cost analysis to evaluate the economic feasibility of ICP desalination to bring down the salinity of these brine sources to 35,000 ppm, at which reverse osmosis technology is available to operate efficiently. Based on the experimental data, the electrical energy was estimated as described in Section 3.1, and the pumping energy was calculated to obtain the total energy consumption. For a given set of the feed and product salinity, the flow velocity, and hence the applied current, was varied to obtain the energy consumption as a function of the current density.

4.4.1 Stand-alone ICP system

In Figure 4.4, we show a case of partial desalination from the feed salinity of 50,000 ppm to the product salinity of 35,000 ppm. Figure 4.4a shows a typical relation between the electrical and the pumping energy and the current. A high current leads to a greater electrical power and energy consumption. It also requires an increased flow and volumetric flowrate for the same salt removal ratio. Consequently, the pumping energy increases with the current. However, the ICP desalination generally operates with a low flow velocity, which is much slower than in electrodialysis, leading to very low pressure drops and a negligible contribution of pumping power to the total energy consumption. The energy consumption was used to calculate the operating cost; combined with the capital cost based on the required membrane area, the total

water cost is plotted as a function of the current density in Figure 4.4b. At the fixed salt removal ratio, a high current results in a fast flow and reduces the membrane area required, shown by the decreasing capital cost in Figure 4.4b. Considering the contributions from the operating and the capital costs, the optimal current, electrical energy consumption, and water cost were determined to be 330 A/m^2, 6.5 kWh/m^3-ICP-diluate, and \$1.4/m^3-ICP-diluate, respectively.

We analyzed the water cost of the partial desalination for a range of feed salinity and a fixed product salinity of 35,000 ppm (Figure 4.5). The water cost increases with the feed salinity mainly because of the large amount of ion removal required. For similar reasons, the optimal current density increases with the feed salinity (Figure 4.5a), as a high ion removal rate per membrane area is more cost efficient at high salinity. Figure 4.5b shows the breakdown of water cost to the operating and the capital costs. As the feed salinity increases, the operating cost accounts a greater portion of the total water cost due to the increasing importance on high salt removal rate. For the feed salinity of 75,000 ppm, the optimal electrical energy consumption and the water cost were 26 kWh/m^3-ICP-diluate and \$4.60/m^3-ICP-diluate, respectively. These values are similar to a comparable electrodialysis performance (feed and product salinity of 90,000 ppm and 40,700 ppm, respectively), which resulted in the electrical energy consumption of 20 – 22 kWh/m^3 of diluate stream and the water cost of ~\$5.5/m^3 of diluate stream [37]. Currently, complete treatment of high salinity brine can be done relatively efficiently via MVC technology. The MVC cost for shale gas produced water treatment is \$22 – 39/m^3 of product water [54]. Based on our cost analysis, the ICP partial desalination in combination with reverse osmosis (< \$2/m^3 of pure water) shows potential to be economically competitive for high salinity produced water treatment when compared to the current MVC technology.

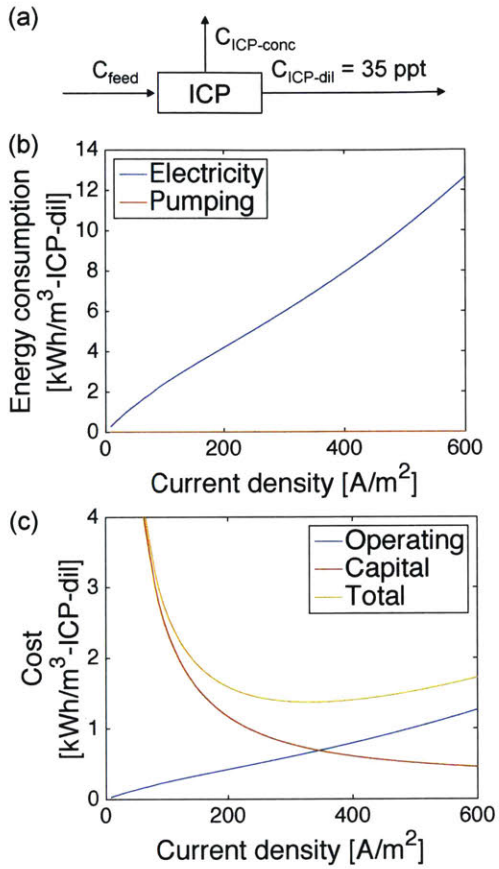

Figure 4.4 Water cost optimization for partial desalination from feed salinity of 50,000 ppm to diluate salinity of 35,000 ppm (= 35 ppt). Recovery ratio (RR) = 0.5. (a) Schematic of ICP partial desalination used in Figures 4.4 and 4.5. The diluate salinity is fixed to 35,000 ppm. (b) Electrical and pumping energy as a function of current. (c) Water cost as a function of current. Total cost is the sum of operating (electricity) cost and capital cost. All costs are expressed as U.S. dollar per diluate volume (m^3).

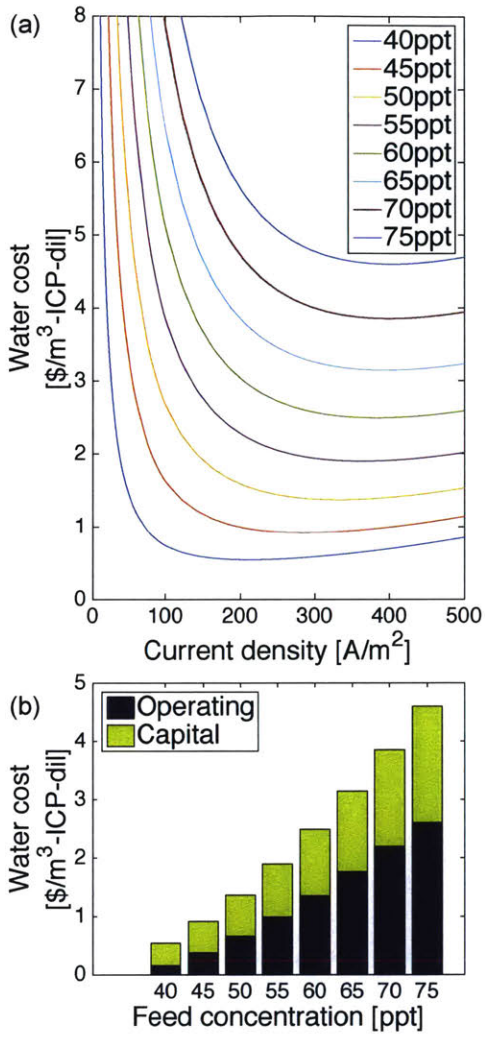

Figure 4.5 Water cost optimization for partial desalination for various feed salinity. Diluate salinity is fixed to 35,000ppm (seawater level). RR = 0.5. Total cost is the sum of electricity cost and capital cost. All costs are expressed as U.S. dollar per diluate volume (m^3) (a) Water cost as a function of current for various feed salinity. (b) Optimal water cost for a range of feed salinity, broken down into contribution from operating and capital costs.

4.4.2 ICP-RO hybrid

Next, the water cost from the ICP-RO hybrid process was analyzed. Here, partial desalination with ICP desalination is followed by complete desalination (*i.e.*, product salinity is 0 ppm) with RO (see Figure 4.6a). The feed and the product salinities were fixed; the feed salinity to the RO step, or the product salinity in the ICP desalination, was varied to determine the feed concentration for an optimal ICP-RO operation. The ICP recovery ratio was kept at 50%, while the RO recovery ratio was varied with the feed salinity to result in the concentrate stream concentration of 70,000 ppm. Figure 4.6 shows the ICP-RO water cost for the starting salinity (*i.e.*, the feed to the ICP-RO process) of and 50,000 ppm and 75,000 ppm. The starting salinity of 50,000 ppm represents the highest seawater salinities practically encountered in the northern parts of the Arabian Gulf while the choice of 75,000 ppm reflects a typical salinity of brine from seawater desalination plants. When the RO feed concentration equals the starting salinity, the ICP desalination step was omitted, and the water cost was calculated for the sole RO treatment. Figure 4.6b shows that the total water cost decreases with a higher RO feed concentration and reaches a minimum for the sole RO operation. This is because the increase in the RO cost increase is much smaller than the reduction in the ICP cost reduction as the ICP/RO transition concentration increases. Furthermore, since the recovery of ICP desalination is 50%, the total volume of desalinated water was reduced to half, raising the water cost per volume of desalinated water. From our cost analysis, the RO-only desalination is more efficient than the ICP-RO hybrid for feed salinity up to 50,000 ppm. However, practically seawater RO systems are used to treat feeds with salinities up to around 50,000 ppm with the maximum operating pressure for the systems being around 68 bar, which corresponds to concentrate side concentration of 73,000 – 74,000 ppm [22]. The pressure limit is dictated by material limits on conventional seawater RO

membranes, which in turn limit the brine and feed salinity levels. For treating feed salinities greater than 50,000 ppm, the ICP-RO hybrid can be a cost efficient solution.

We analyzed the ICP-RO water cost for a starting salinity of 75,000 ppm, which can represent a concentrate stream from desalination seawater plants. As shown in Figure 4.6c, the water cost follows a similar trend as in Figure 4.6b, but the minimum cost is obtained when the ICP/RO transition concentration is 50,000 ppm. This is because at a very high RO feed concentration, the RO recovery is reduced drastically, hence greatly increasing the specific cost of both ICP and RO. The water cost of \$8-9 per m^3 of the pure product is much lower than the water cost of \$22-39 per m^3 of product water for MVC, which is the current technology for treating brine at this concentration. The relatively low water cost of ICP-RO hybrid indicates that this technology may be an economically viable method for treatment of brine at 75,000 ppm.

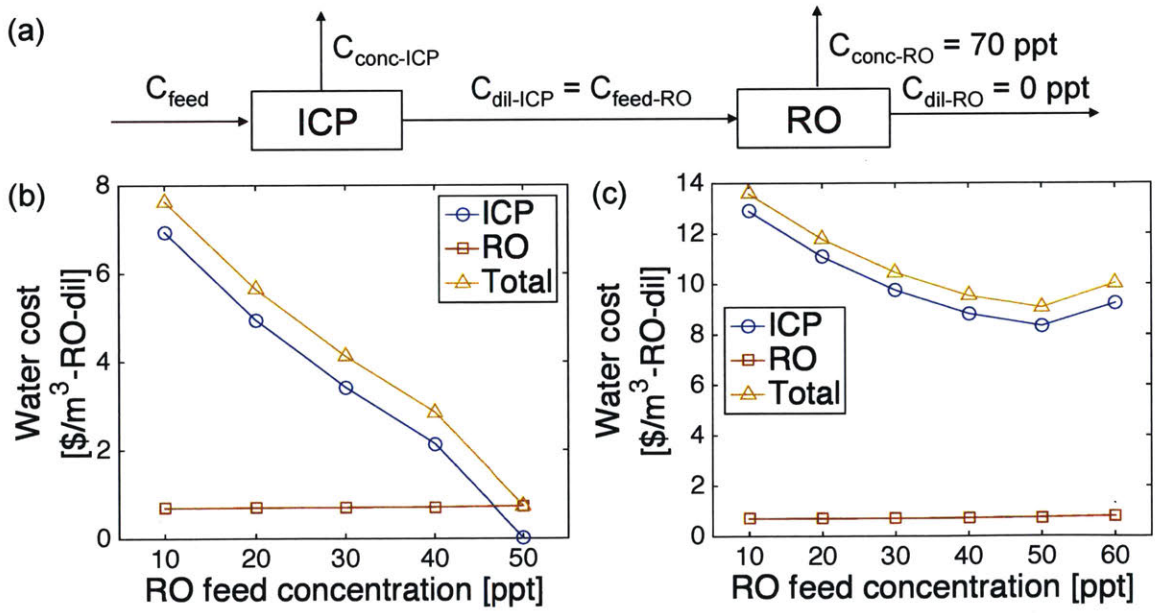

Figure 4.6 ICP-RO cost analysis. (a) Schematic of the ICP-RO hybrid. ICP desalination was performed on a feed salinity of 50 ppt (b) and 75 ppt (c), and its diluate stream was taken for complete desalination by RO. Hence, the RO feed concentration is equal to the diluate concentration of ICP. In all cases, the recovery in ICP was 50%, and the recovery of RO was

varied to give a fixed concentrate stream concentration of 70 ppt. When the RO feed concentration equals the overall feed salinity, the water cost is for a RO-only process, whose recovery is double of the ICP-RO hybrid.

4.5 Application 2: Brine concentration for salt production

The second application is the concentration of brine for salt production. In most brine management practices, the diluate stream is considered the useful product. However, the concentrate stream can also be a useful product. For salt production applications, the concentrated brine stream is fed in to a crystallizer where salt is crystallized out [40]. Crystallizers are expensive and so typically, seawater is concentrated first using desalination technologies to reduce the load of the crystallizer in salt production and reduce the overall cost [28]. Chung *et al.* had compared the performance of state-of-the-art crystallizers to state-of-the-art brine concentrators and found that there was a greater scope for improving the energy efficiency of brine concentration [28]. This led us to investigate the potential of ICP desalination for use as brine concentrator.

Figure 4.7a describes a multi-stage ICP desalination for brine concentration. The starting salinity of 70,000 ppm represents a typical brine concentration from seawater desalination plants, and the final salinity of 200,000 ppm represents a typical feed to crystallizer in salt production plants. Since the ICP desalination has a maximum recovery of 50%, a single-stage ICP process can achieve a maximum of twofold concentration, and the concentration from 70,000 ppm to 200,000 ppm needs to be performed in multiple stages. In the multi-stage ICP desalination scheme, the concentrate stream from each stage is fed to the next stage for further concentration, with the recovery of 50% at each stage. The salt removal ratios at all stages in a system were about the same. The water cost is expressed as cost per final concentrate volume. In the three-

stage ICP process shown in Figure 4.7b, the water cost for an earlier stage is higher than the following stage. Although the earlier stage is working at a lower concentration, the treatment volume for the earlier stage that is required to generate the final concentrate is twice the next stage volume. This difference in the treatment volume resulted in the high water cost in the early stages. Since each additional stage increases water cost by doubling the starting treatment volume, the water cost may be minimized when minimum number of stages is employed. The results in Figure 4.7c show that the minimum water cost is indeed obtained for the two-stage system, which consists of the minimum number of stages, and the water cost increases with the increasing number of stages. The optimal water cost is $\$25/m^3$, which is equivalent to \$109/tonne salt produced. Adding the crystallization cost of approximately \$40/tonne of salt [47], the total salt production cost from the ICP-crystallizer is \$149/tonne salt. The cost of brine concentration by multi-stage ICP desalination is about twice of the brine concentration cost by electrodialysis (concentration from 35,000 ppm to 200,000 ppm), which is around \$60/tonne salt [47]. The large gap in the cost from the two processes is most likely to stem from that the recovery in ICP desalination is limited to 50% at each stage, whereas the recovery in ED is much higher. Furthermore, the ED cost is obtained from a working salt production plant, where the process is well engineered and optimized, and thus the cost may be further lowered.

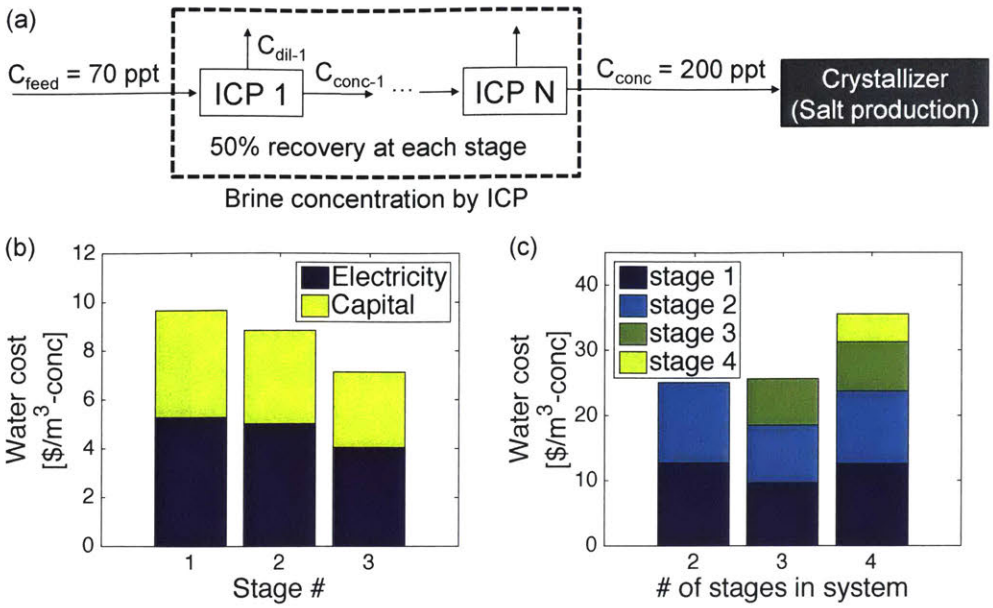

Figure 4.7 ICP desalination for brine concentration. (a) Schematic of multi-stage ICP desalination for brine concentration. N is the number of stages. In all cases, the salt removal ratios for all stages in a system were about the same. (b) Water cost for 3-stage system, broken down by stage. (c) Water cost for systems with various stage numbers.

4.6 Conclusion

In this work, we utilized a set of experimental data from a lab-scale ICP desalination device to build a model that estimates the electrical energy consumption in ICP desalination at high salinity. This model was then used to calculate the operating cost, and the capital cost was calculated based on the effective membrane area required to reach the throughput. For a fixed feed and product salinity, the total water cost was calculated over a range of current, and the optimal operating conditions and water cost were obtained. This water cost analysis was performed for two potential applications of ICP desalination in high salinity brine treatment.

The first application was partial desalination to seawater salinity (35,000 ppm) so that the product can be treated by seawater reverse osmosis. The cost analysis showed that the ICP partial desalination cost with feed salinity of 75,000 ppm was comparable to an electrodialysis

performance at similar feed and product salinity. This cost is much lower than the complete desalination by MVC, a current desalination method for produced water. Therefore, brine treatment by ICP desalination in combination with seawater RO can become an economically competitive option for high salinity brine desalination. The cost analysis of ICP-RO hybrid shows that for the feed salinity range, at which RO is technically available, the ICP-RO hybrid is not economically feasible mainly due to the reduced recovery in ICP-RO and the insensitivity of RO cost with increasing feed salinity, but the ICP-RO hybrid can be an economically viable solution for treatment of brine from seawater desalination plants (~75,000 ppm), which is at the concentration above the limit of RO.

The second application was concentration of brine (to 200,000 ppm), by multi-stage ICP process, for salt production. We varied the number of stages and found that the operation becomes more efficient when the number of stages is minimized. The optimal two-stage system resulted in the water cost of $109/tonne salt produced. This cost is about twice the cost of brine concentration by ED. The high ICP cost can be contributed to the large volume of treatment required in early stages due to the ICP recovery limit of 50% per stage. To reduce the ICP cost for brine concentration, the salt retention in the concentrate stream should be enhanced, and the distribution of salt concentration (or salt removal) ratio at the stages can be optimized.

4.7 References

[1] M. Elimelech, W.A. Phillip, The Future of Seawater Desalination: Energy, Technology, and the Environment, Science (80-.). 333 (2011). http://science.sciencemag.org/content/333/6043/712 (accessed April 13, 2017).

[2] PROGRESS TOWARDS COMMERCIALIZATION OF A NOVEL LOW-ENERGY DESALINATION SYSTEM, (2014). http://www.siww.com.sg/sites/default/files/DES_Mr-Rodney-Aulick.pdf (accessed April 13, 2017).

[3] R.K. Mcgovern, S.M. Zubair, J.H. Lienhard, V. Presenter, : Ronan, K. Mcgovern, DESIGN AND OPTIMIZATION OF HYBRID ED-RO SYSTEMS FOR THE TREATMENT OF HIGHLY SALINE BRINES, (2013) 13–370. http://web.mit.edu/lienhard/www/papers/conf/MCGOVERN_IDA_Tianjin_2013.pdf (accessed April 13, 2017).

[4] J. Morillo, J. Usero, D. Rosado, H. El Bakouri, A. Riaza, F.-J. Bernaola, Comparative study of brine management technologies for desalination plants, Desalination. 336 (2014) 32–49. doi:10.1016/j.desal.2013.12.038.

[5] J.M. Arnal, M. Sancho, I. Iborra, J.M. Gozálvez, A. Santafé, J. Lora, Concentration of brines from RO desalination plants by natural evaporation, Desalination. 182 (2005) 435–439. doi:10.1016/j.desal.2005.02.036.

[6] S. Lattemann, T. Höpner, Environmental impact and impact assessment of seawater desalination, Desalination. 220 (2008) 1–15. doi:10.1016/j.desal.2007.03.009.

[7] D.L. Shaffer, L.H. Arias Chavez, M. Ben-Sasson, S. Romero-Vargas Castrillón, N.Y. Yip, M. Elimelech, Desalination and Reuse of High-Salinity Shale Gas Produced Water: Drivers, Technologies, and Future Directions, Environ. Sci. Technol. 47 (2013) 9569–9583. doi:10.1021/es401966e.

[8] K.B. Gregory, R.D. Vidic, D. a. Dzombak, Water Management Challenges Associated with the Production of Shale Gas by Hydraulic Fracturing, Elements. 7 (2011) 181–186. doi:10.2113/gselements.7.3.181.

[9] R.D. Vidic, S.L. Brantley, J.M. Vandenbossche, D. Yoxtheimer, J.D. Abad, Impact of Shale Gas Development on Regional Water Quality, Science (80-.). 340 (2013). http://science.sciencemag.org/content/340/6134/1235009 (accessed April 13, 2017).

[10] D.A. Roberts, E.L. Johnston, N.A. Knott, Impacts of desalination plant discharges on the marine environment: A critical review of published studies, Water Res. 44 (2010) 5117–5128. doi:10.1016/j.watres.2010.04.036.

[11] E. Gacia, O. Invers, M. Manzanera, E. Ballesteros, J. Romero, Impact of the brine from a desalination plant on a shallow seagrass (Posidonia oceanica) meadow, Estuar. Coast. Shelf Sci. 72 (2007) 579–590. doi:10.1016/j.ecss.2006.11.021.

[12] S. Uddin, A.N. Al Ghadban, A. Khabbaz, Localized hyper saline waters in Arabian Gulf from desalination activity—an example from South Kuwait, Environ. Monit. Assess. 181 (2011) 587–594. doi:10.1007/s10661-010-1853-1.

[13] J.V. Del Bene, G. Jirka, J. Largier, Ocean brine disposal, Desalination. 97 (1994) 365–372. doi:10.1016/0011-9164(94)00100-6.

[14] L. Katzir, Y. Volkmann, N. Daltrophe, E. Korngold, R. Mesalem, Y. Oren, J. Gilron, WAIV - Wind aided intensified evaporation for brine volume reduction and generating mineral byproducts, Desalin. Water Treat. 13 (2010) 63–73. doi:10.5004/dwt.2010.772.

[15] M. Ahmed, W.H. Shayya, D. Hoey, A. Mahendran, R. Morris, J. Al-Handaly, Use of evaporation ponds for brine disposal in desalination plants, Desalination. 130 (2000) 155–168. doi:10.1016/S0011-9164(00)00083-7.
[16] J. Gilron, Y. Folkman, R. Savliev, M. Waisman, O. Kedem, WAIV — wind aided intensified evaporation for reduction of desalination brine volume, Desalination. 158 (2003) 205–214. doi:10.1016/S0011-9164(03)00453-3.
[17] C.E. Clark, J.A. Veil, Produced water volumes and management practices in the United States., Argonne, IL (United States), 2009. doi:10.2172/1007397.
[18] S. Rassenfoss, From Flowback to Fracturing: Water Recycling Grows in the Marcellus Shale, J. Pet. Technol. 63 (2011) 48–51. doi:10.2118/0711-0048-JPT.
[19] B.D. Lutz, A.N. Lewis, M.W. Doyle, Generation, transport, and disposal of wastewater associated with Marcellus Shale gas development, Water Resour. Res. 49 (2013) 647–656. doi:10.1002/wrcr.20096.
[20] J.-P. Nicot, B.R. Scanlon, Water Use for Shale-Gas Production in Texas, U.S., Environ. Sci. Technol. 46 (2012) 3580–3586. doi:10.1021/es204602t.
[21] L.F. Greenlee, D.F. Lawler, B.D. Freeman, B. Marrot, P. Moulin, Reverse osmosis desalination: Water sources, technology, and today's challenges, Water Res. 43 (2009) 2317–2348. doi:10.1016/j.watres.2009.03.010.
[22] C. Fritzmann, J. Löwenberg, T. Wintgens, T. Melin, State-of-the-art of reverse osmosis desalination, Desalination. 216 (2007) 1–76. doi:10.1016/j.desal.2006.12.009.
[23] M.A. Darwish, F. Al Asfour, N. Al-Najem, Energy consumption in equivalent work by different desalting methods: case study for Kuwait, Desalination. 152 (2003) 83–92. doi:10.1016/S0011-9164(02)01051-2.
[24] N. Ghaffour, T.M. Missimer, G.L. Amy, Technical review and evaluation of the economics of water desalination: Current and future challenges for better water supply sustainability, Desalination. 309 (2013) 197–207. doi:10.1016/j.desal.2012.10.015.
[25] A. Koren, N. Nadav, Mechanical vapour compression to treat oil field produced water, Desalination. 98 (1994) 41–48. doi:10.1016/0011-9164(94)00130-8.
[26] J. Veza, Mechanical vapour compression desalination plants — A case study, Desalination. 101 (1995) 1–10. doi:10.1016/0011-9164(95)00002-J.
[27] G.P. Thiel, E.W. Tow, L.D. Banchik, H.W. Chung, J.H. Lienhard, Energy consumption in desalinating produced water from shale oil and gas extraction, Desalination. 366 (2015) 94–112. doi:10.1016/j.desal.2014.12.038.
[28] H.W. Chung, K.G. Nayar, J. Swaminathan, K.M. Chehayeb, J.H. Lienhard V, Thermodynamic analysis of brine management methods: Zero-discharge desalination and salinity-gradient power production, Desalination. 404 (2017) 291–303. doi:10.1016/j.desal.2016.11.022.
[29] W.F. Heins, Is a Paradigm Shift in Produced Water Treatment Technology Occurring at SAGD Facilities?, J. Can. Pet. Technol. 49 (2010) 10–15. doi:10.2118/132804-PA.
[30] A. Alkhudhiri, N. Darwish, N. Hilal, Membrane distillation: A comprehensive review, Desalination. 287 (2012) 2–18. doi:10.1016/j.desal.2011.08.027.
[31] G.W. Meindersma, C.M. Guijt, A.B. de Haan, Desalination and water recycling by air gap membrane distillation, Desalination. 187 (2006) 291–301. doi:10.1016/j.desal.2005.04.088.
[32] S. Al-Obaidani, E. Curcio, F. Macedonio, G. Di Profio, H. Al-Hinai, E. Drioli, Potential of membrane distillation in seawater desalination: Thermal efficiency, sensitivity study and

cost estimation, J. Memb. Sci. 323 (2008) 85–98. doi:10.1016/j.memsci.2008.06.006.
[33] P. Długołęcki, P. Ogonowski, S.J. Metz, M. Saakes, K. Nijmeijer, M. Wessling, On the resistances of membrane, diffusion boundary layer and double layer in ion exchange membrane transport, J. Memb. Sci. 349 (2010) 369–379. doi:10.1016/j.memsci.2009.11.069.
[34] K.M. Chehayeb, D.M. Farhat, K.G. Nayar, J.H. Lienhard V, Optimal design and operation of electrodialysis for brackish-water desalination and for high-salinity brine concentration, Desalin. (under Rev. (2017).
[35] H. Strathmann, Electrodialysis, a mature technology with a multitude of new applications, Desalination. 264 (2010) 268–288. doi:10.1016/j.desal.2010.04.069.
[36] V. V. Nikonenko, A. V. Kovalenko, M.K. Urtenov, N.D. Pismenskaya, J. Han, P. Sistat, G. Pourcelly, Desalination at overlimiting currents: State-of-the-art and perspectives, Desalination. 342 (2014) 85–106. doi:10.1016/j.desal.2014.01.008.
[37] R.K. McGovern, A.M. Weiner, L. Sun, C.G. Chambers, S.M. Zubair, J.H. Lienhard V, On the cost of electrodialysis for the desalination of high salinity feeds, Appl. Energy. 136 (2014) 649–661. doi:10.1016/j.apenergy.2014.09.050.
[38] E. Korngold, L. Aronov, N. Daltrophe, Electrodialysis of brine solutions discharged from an RO plant, Desalination. 242 (2009) 215–227. doi:10.1016/j.desal.2008.04.008.
[39] Y. Oren, E. Korngold, N. Daltrophe, R. Messalem, Y. Volkman, L. Aronov, M. Weismann, N. Bouriakov, P. Glueckstern, J. Gilron, Pilot studies on high recovery BWRO-EDR for near zero liquid discharge approach, Desalination. 261 (2010) 321–330. doi:10.1016/j.desal.2010.06.010.
[40] M. Turek, Dual-purpose desalination-salt production electrodialysis, Desalination. 153 (2003) 377–381. doi:10.1016/S0011-9164(02)01131-1.
[41] R. Kwak, V.S. Pham, B. Kim, L. Chen, J. Han, Enhanced Salt Removal by Unipolar Ion Conduction in Ion Concentration Polarization Desalination., Sci. Rep. 6 (2016) 25349. doi:10.1038/srep25349.
[42] B. Kim, R. Kwak, H.J. Kwon, V.S. Pham, M. Kim, B. Al-Anzi, G. Lim, J. Han, Purification of High Salinity Brine by Multi-Stage Ion Concentration Polarization Desalination., Sci. Rep. 6 (2016) 31850. doi:10.1038/srep31850.
[43] B. Kim, H. Kwon, S.H. Ko, G. Lim, J. Han, Partial desalination of hypersaline brine by lab-scale ion concentration polarization device, Desalination. 412 (2017) 20–31. doi:10.1016/j.desal.2017.02.018.
[44] R.K. McGovern, S.M. Zubair, J.H. Lienhard V, The benefits of hybridising electrodialysis with reverse osmosis, J. Memb. Sci. 469 (2014) 326–335. doi:10.1016/j.memsci.2014.06.040.
[45] H. Strathmann, Design and Cost Estimates, in: Membr. Handb., Springer US, Boston, MA, 1992: pp. 246–254. doi:10.1007/978-1-4615-3548-5_19.
[46] E.T. Sajtar, D.M. Bagley, Electrodialysis reversal: Process and cost approximations for treating coal-bed methane waters, Desalin. Water Treat. 2 (2009) 284–294. doi:10.5004/dwt.2009.259.
[47] Asahi Glass and Chemicals Co., Personal Communication to Kishor Nayar, (n.d.).
[48] K.G. Nayar, J. Fernandes, R.K. McGovern, K.P. Dominguez, B. Al-Anzi, J.H. Lienhard V, COSTS AND ENERGY NEEDS OF RO-ED HYBRID SYSTEMS FOR ZERO BRINE DISCHARGE SEAWATER DESALINATION, in: Int. Desalin. Assoc. World Congr. 2017, Sao Paulo, Brazil (under Rev., 2017.

[49] K.H. Mistry, R.K. McGovern, G.P. Thiel, E.K. Summers, S.M. Zubair, J.H. Lienhard V, Entropy Generation Analysis of Desalination Technologies, Entropy. 13 (2011) 1829–1864. doi:10.3390/e13101829.
[50] K.G. Nayar, M.H. Sharqawy, L.D. Banchik, J.H. Lienhard V, Thermophysical properties of seawater: A review and new correlations that include pressure dependence, Desalination. 390 (2016) 1–24. doi:10.1016/j.desal.2016.02.024.
[51] DesalData, DesalData Cost Estimator, (2017).
[52] Comparison table for detailed specifications of Cation/Anion Exchange Membranes, ASTOM Corp. (n.d.). http://www.astom-corp.jp/en/product/10.html (accessed April 14, 2017).
[53] B. Kim, S. Choi, V.S. Pham, R. Kwak, J. Han, Energy efficiency enhancement of electromembrane desalination systems by local flow redistribution optimized for the asymmetry of cation/anion diffusivity, J. Memb. Sci. 524 (2017) 280–287. doi:10.1016/j.memsci.2016.11.046.
[54] J.A. Slutz, J.A. Anderson, R. Broderick, P.H. Horner, Key Shale Gas Water Management Strategies: An Economic Assessment, in: Int. Conf. Heal. Saf. Environ. Oil Gas Explor. Prod., Society of Petroleum Engineers, 2012. doi:10.2118/157532-MS.

5. SINGLE-DEVICE WATER PURIFICATION: ELECTROCOAGULATION (EC) – ION CONCENTRATION POLARIZATION (ICP) HYBRID FOR REMOVAL OF NON-SALT AND SALT CONTAMINANTS

The published journal paper (S. Choi, B. Kim, and J. Han, Lab on a Chip, 2017, DOI: 10.1039/C7LC00258K) was used in its entirety for Chapter 5, with minor updates and modifications. S. C. and J. H. conceived the idea and designed the study. S. C. carried out the experiments and analyzed the data. S. C. and B. K. and J. H. wrote the manuscript. J. H. supervised the study.

5.1 Introduction

Typical water treatment system consists of multiple stages of pre- and post-treatment to remove various non-salt contaminants (*e.g.*, suspended particles, organics, and biologics) and a desalination step to remove dissolved ions. Among these, desalination is the most energy- and capital-intensive step, but in some cases, the pre-treatment can be expensive, accounting for 10%-20% of the total capital cost.[1] Complicated pre-treatment requires a larger footprint as well as an increased cost of water treatment. These are especially important considerations when developing small-scale portable water treatment devices, for disaster relief or for places where water and energy resources are scarce. In this work, we prototyped a system that performs pretreatment and desalination in a single device by combining two electrochemical water treatment technologies, namely, electrocoagulation (EC) and ion concentration polarization (ICP) desalination.

Electrocoagulation is a separation technology that utilizes the electrolysis of a sacrificial metal anode that releases metal coagulants and causes destabilization and flocculation of target materials in the solution. EC has been demonstrated to remove various contaminants including

bacteria[2,3], viruses[4,5], silica[6], suspended particles[7,8], heavy metals[9–11], organic dyes[12–17], oil wastes[18,19], and fluorides[20,21]. Recently, there has been a growing interest in EC for water treatment because it can address a wide range of contaminants, can be automated, is portable and scalable, and eliminates the use of chemical coagulants. For these reasons, EC is well-suited as a low-cost, localized water treatment technology.[22,23] For example, a bench-scale EC has been developed and tested as a pretreatment for seawater treatment by ultrafiltration (UF) for pilot testing of EC-UF in military water purification systems.[24]

Ion concentration polarization desalination, or ICP desalination, is a relatively new electromembrane desalination technology.[25–27] In an ICP desalination system, an electrolytic cell is divided by one type of ion exchange membranes (either anion or cation exchange membranes). When electric current is applied, the selective ion transport through the ion exchange membranes creates an ion concentrated region and an ion depleted region in a channel, and desalted water is obtained by extracting the desalted stream from the bifurcated channel outlet (see Figure 5.1b). ICP desalination is similar to electrodialysis, which is a well-known electromembrane desalination technology, in design and operation, but it enjoys several important advantages over electrodialysis. ICP desalination can remove suspended particles as well as dissolved ions from the desalted stream, and thus it is more resistant to fouling. Compared to electrodialysis, the salt removal in ICP desalination can also be more effective in terms of current utilization.[28] Moreover, electromembrane desalination systems, such as electrodialysis and ICP desalination, are modular in design and thus can be implemented in small scale. Several groups investigated the feasibility of small/medium-scale electrodialysis powered

by renewable energies, including a recent study that showed the economic feasibility of a village-scale, solar-powered electrodialysis desalination systems for rural areas of India.[29,30]

Since ICP desalination and EC are both viable for small-scale water treatment and electrically driven, we decided to integrate the two processes into a single electrochemical system. Through this hybridization, we aimed to reduce unnecessary voltage drop, electrical energy consumption, and the footprint. The EC-ICP hybrid system was demonstrated on a microfluidic platform. This microfluidic EC-ICP platform is, to our knowledge, the first demonstration of electrocoagulation in micro-scale. The microfluidic system enables us to visualize both EC and ICP desalination processes in small scale and facilitates a systematic optimization of various parameters, which then can be used to build a scaled-up system with useful flowrates. In fact, similar strategy has been used for the initial development of ICP desalination,[25,26] which was then recently scaled up successfully.[27]

5.2 Methods

5.2.1 Description of electrocoagulation (EC) – ion concentration polarization (ICP hybrid

The schematics of EC, ICP desalination, and the EC-ICP hybrid are shown in Figure 5.1. Figure 5.1a depicts a single-cell, continuous EC operation, where the feed solution is continuously flowed through an electrolytic cell with a sacrificial metal anode, and the metal coagulants are released to destabilize the contaminants. In Figure 5.1b, a single-cell ICP desalination with cation exchange membranes (CEMs) is described. In both ICP desalination and electrodialysis, the side channels in contact with the electrodes are not used for desalination because the solution is used to wash away the products from the electrode reactions. To combine

EC and ICP desalination in a single electrochemical cell, a metal anode is placed in an ICP desalination cell (see Figure 5.1c). The feed solution is first run through the anode rinsing channel, where the non-salt contaminants are coagulated and removed via EC. Then, the solution with the remaining dissolved ions is run through the ICP desalination cells, where the solution is split into desalted and concentrated streams. A single device can have multiple ICP cells in parallel to increase the throughput. By adjusting the number of the ICP cells, the operating conditions of EC and ICP operations can be controlled independently.

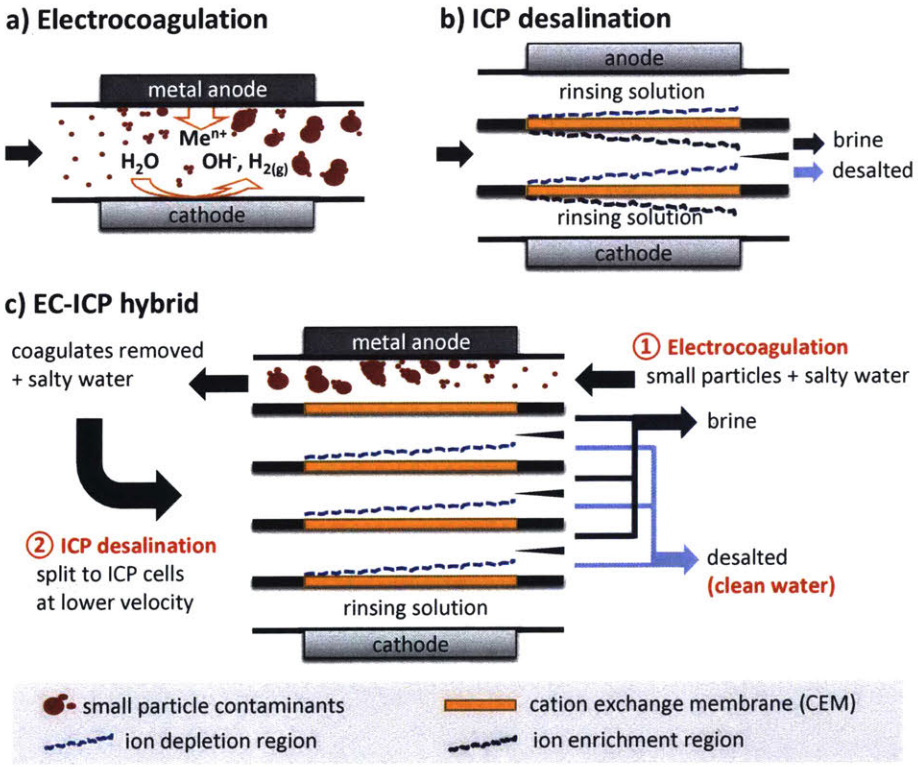

Figure 5.1 Schematics of a) electrocoagulation (EC), b) ion concentration polarization (ICP) desalination, and c) EC-ICP hybrid. Various components in the schematics are defined in the box at the bottom of the figure. Black arrows indicate the direction of the flow. a) In an EC cell, the anode material needs to be a metal. The reactants and products of the reactions on the electrodes are specified. c) All solution undergoes EC treatment first, where small particulates are coagulated and removed. The product of EC is split into multiple ICP cells because ICP desalination requires much slower flow for sufficient salt removal.

5.2.2 Microfluidic EC-ICP device

Fabrication of microfluidic desalination devices has previously been developed, and the detailed fabrication process is described in Kwak *et al.*[31,32] Briefly, a microfluidic EC-ICP device consists of two rinsing channels in contact with the electrodes and one or more ICP desalination channels. As depicted in Figure 5.2a, the device is fabricated by assembling the top and bottom parts, each with matching slots for membranes and electrodes and gaps between the two parts, which become the channels. The slots for the membranes and the electrodes are much deeper than the channels, in order to prevent inter-channel leakages. Polydimethylsiloxane (PDMS) was selected as the device material for its optical transparency and flexibility. The negative mold for the device was fabricated by a 3D printer (Accura SL 5530, 3D systems Inc., USA), and the PDMS device parts were casted from this mold. The top and bottom parts were bonded by air plasma treatment of the bonding surfaces. The membranes were assembled dry as they came, and swelled in deionized (DI) water for 24 hours after the boding, during which any gaps between the structure and the membranes were sealed to prevent from inter-channel ion leakage. An image of the assembled EC-ICP device is shown in Figure 5.2b. Before the experiment, electrically conducting wires (Titanium wires, McMaster-Carr, Inc, Atlanta, GA) were connected to the electrodes to apply the current from the source measurement unit.

The electrode was composed of an aluminum plate with a thickness of 0.4mm (McMaster-Carr, Inc, Atlanta, GA). Fumasep® FTCM-E (FuMa-Tech GmbH, Germany) was used as cation exchange membrane. PDMS used as the device material was Sylgard 184 (Dow Corning Corporation, Michigan).

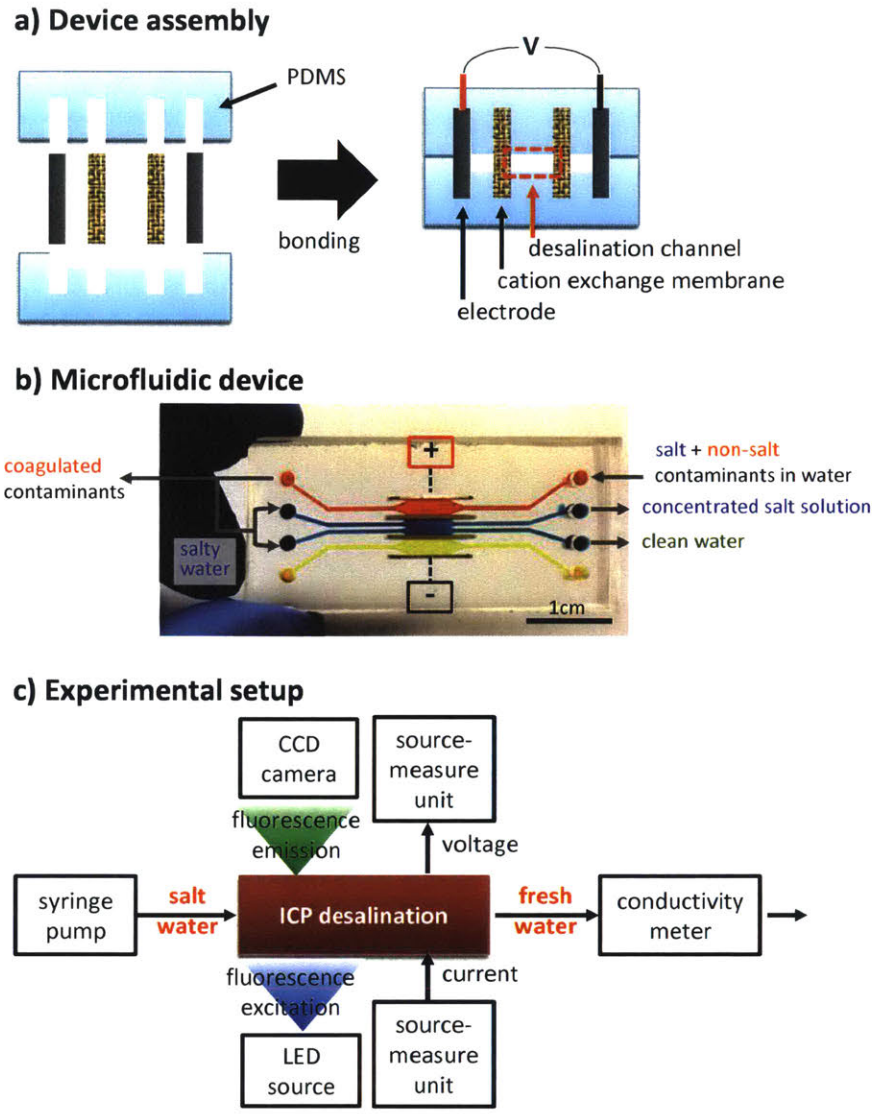

Figure 5.2 a) Schematic view of device fabrication. Cross-sectional view of a device with a single ICP channel is shown. The red boxed area is the cross section of an ICP desalination channel. The horizontal and vertical distances represent the width and the depth of the channel, respectively. b) An image of microfluidic device with a single ICP desalination cell. The red, blue, and yellow channels represent EC pre-treatment, ICP desalination, and cathode rinsing channels. c) Schematic view of experimental setup. A microfluidic device was connected to various equipment and the water purification process was observed under a microscope. All experiments were done with a constant current source, and the corresponding voltage was monitored.

5.2.3 Microfluidic experiments

The experimental setup is shown in Figure 5.2c. The fabricated device was connected to the feed solution and the outlet with tubing. The device was placed under a microscope for visualization of the process throughout the experiment. The feed solution was introduced to the device with syringe pumps (PHD 2200, Harvard Apparatus). Charged fluorescent dye (Alexa 488 Fluor®, Invitrogen) was added to qualitatively visualize the ion concentration profile within the channel, which was observed under a fluorescent microscope (IX-71, Olympus) with a thermoelectrically cooled charge-coupled device (CCD) camera (Hamamatsu Co., Japan). The fluorescent dye concentration was relatively low (~1μM), compared to the total ion concentration (10mM-1.7M), and thus the dye did not affect the current conduction. Moreover, Alexa 488 is known to be pH-insensitive over a wide range (pH= 4-9) and highly photostable.[33] A constant current was applied across the entire cell using a current-voltage source measurement unit (Keithley 236, Keithley Instruments, Inc., USA), and the corresponding voltage drop was measured with the same equipment. For the EC-ICP experiments, the bulk concentration of the center product stream was monitored with a conductivity meter (VWR symphony conductivity meter, VWR International, LLC, USA) connected to a flow-through conductivity microelectrode (Microelectrode, Inc., USA).

The salinity of the solutions in the experiments was 10mM-1.7M sodium chloride (Sigma-Aldrich) in DI water. The operating current across the device ranged between 0mA to 1.6mA. In all experiments, the cathode rinsing solution was composed of NaCl in DI water, with the same salinity as the EC and/or ICP feed. Depending on the presence of EC process, the anode solution contained other contaminants (silica or bacteria).

Since the removal profile by EC is different for each contaminant, the device used in the experiment was optimized for each contaminant. Especially for the continuous, multi-cell EC-ICP experiment, the system needed to be optimized for sufficient silica removal and salinity reduction. Regarding device length (transverse), the EC experiments used devices with a shorter length (L=5mm) because EC requires a relatively short residence time, whereas ICP desalination requires a relatively long residence time for sufficient ion removal. Regarding the device depth, the EC channels were generally deep (d = 800μm) and ICP channels were shallow because 1) the flowrates of EC and ICP steps should be matched, 2) ICP desalination requires more current per treatment volume, and 3) the shallow channels help to observe depletion boundary layer in ICP desalination. The channel dimensions in the devices used for the experiments are specified in the experimental section of each experiment.

5.2.4 Silica EC experiments

For the silica removal experiments, the feed solution consisted of 1000 mg/L colloidal silica nanoparticles (LUDOX® TM-40, Sigma-Aldrich) in various salinities. After EC treatment, the product was left undisturbed for > 30 min for coagulates to grow into flocs and to sediment. The supernatant was taken to analyze the silica concentration by the silicomolybdate method with bicarbonate digestion.[34] To quantify the concentration using this method, a reference curve was generated with standard solutions of the same silica particles and background salinity. The recovery was 90% of the feed in all silica EC experiments.

The device used in the silica EC experiment had EC channel dimensions of 1mm width (distance between adjacent membrane/electrode), 800μm depth, and 5mm length. The flowrate was 800μL/min in the EC channel, corresponding to an average flow velocity of 1m/min.

5.2.5 *E. coli* EC experiment

The feed solution consisted of $6.5x10^8$ cells/mL *Escherichia coli* (*E. coli*) BL21 in 20mM NaCl. The *E. coli* were obtained from Yi Group at Tufts University. The *E. coli* concentration was quantified by optical density measurements at λ=600nm (OD600) using ultraviolet-visible spectroscopy (Shimadzu UV-3101PC). To quantify the concentration of *E. coli*, a reference curve was generated with standard solutions of the *E. coli* and the same background salinity (reliable measurement between $2.7x10^7$ cells/mL and $1.35x10^9$ cells/mL). The recovery of the product was 45% of the feed in all *E. Coli* EC experiments. Samples were collected from the product stream, let for coagulation reaction to happen for 20min, and centrifuged for 30sec; the supernatant was then taken for OD600 measurement.

The device in the *E. coli* EC experiment had EC channel dimensions of 2mm width (distance between adjacent membrane/electrode), 200μm depth, and 5mm length. The outlet in the EC channel was bifurcated, and the product from the outlet near the anode was analyzed for *E. coli* removal. The flowrates were 200μL/min in each outlet, corresponding to an average flow velocity of 1m/min.

5.2.6 EC-ICP experiment

For the voltage drop comparison between EC-ICP hybrid and ICP desalination, an EC-ICP device with a single ICP channel was used. The dimensions of the EC channel were 1mm width, 800μm depth, and 5mm length; the dimensions of the ICP channels were 1.5mm width, 800μm depth, and 5mm length. The flowrates were 800μL/min in the EC channel and 300μL/min in each ICP channel, corresponding to average flow velocities of 1m/min and 0.25m/min, respectively. These flowrates were set to match the flow velocities in the continuous,

multi-cell EC-ICP experiment. The background salinity in all solutions used in this experiment was 10mM NaCl.

For the continuous, multi-cell EC-ICP experiments, the feed solution consisted of 1000 mg/L colloidal silica nanoparticles in 20mM NaCl. A coagulation reservoir was added between EC and ICP steps to allow sufficient time (20min residence time in the reservoir) for complete coagulation and sedimentation of silica particles. The recovery from the EC step was 90% of the feed. There were three ICP channels in the EC-ICP device, each with a bifurcated outlet to separate the concentrated and desalted streams. The recovery from the ICP step was 50% of the ICP feed. The final product (*i.e.*, desalting stream in the ICP channels) was connected to an in-line conductivity probe for real-time monitoring, and samples from this stream was analyzed for silica concentration with the method described in the previous section.

The dimensions of the EC channel were 1mm width (distance between adjacent membrane/electrode), 800μm depth, and 20mm length; the dimensions of the ICP channels were 1.5mm width, 200μm depth, and 20mm length. The ICP channels were much shallower than the EC channel. The flowrates were 800μL/min in the EC channel and 75μL/min in each ICP channel, corresponding to average flow velocities of 1m/min and 0.25m/min, respectively. In this EC-ICP experiment, the flowrate in the EC channel was much higher than the total flowrate in the ICP channels, and thus not all of the EC product underwent the desalination step. To increase the desalination capacity, more ICP channels can be added to match the EC flowrate.

5.3 Visualization of EC-ICP process

For demonstration purposes, a single-cell EC-ICP device was employed, and the anode channel was observed to visualize the simultaneous EC and ICP desalination processes, as shown in Figure 5.3. Although the anode channel is not utilized for desalination in the actual EC-ICP system (Figure 5.1c), an ion depletion region is formed due to the selective ion transport through the CEM. The feed solution containing suspended silica particles with background salinity was run through the device while a constant current was applied. A charged fluorescent dye was added to visualize the depletion (white region) and enrichment (dark region) of ionic species under fluorescence microscopy. However, some dye molecules were trapped in the flocs of suspended particles, and thus coagulates could be visualized as the white spots. Coagulation of suspended particles occurred mostly after the solution exited the device, but a small portion of coagulates started to form in the EC cell. These coagulates fouled the channel wall near the sacrificial metal anode, where the metal coagulant was concentrated. The fouling was observed as white lumps and streaks in Figure 5.3. The fouling can potentially become problematic if the coagulates adhere to the anode, create additional resistance, and hinder the release of metal coagulants to the solution. To prevent the fouling, the flow velocity in the EC channel was kept relatively high (v_{avg} = 1m/min). This condition of fast flow in the electrode channel is also used in electrodialysis to minimize effects (*e.g.,* bubbles) from electrolysis. The ion depletion layer near the CEM was relatively thin in this figure because the fast flow allowed only a small portion of the salt ions to be transported through the CEM. In the multi-cell EC-ICP system, as described in Figure 5.1c, the ICP cells have a much longer residence time for substantial salt removal.

The demonstration of EC on a microfluidic platform enabled real-time visualization of the process. The direct observation allowed us to identify a potential issue with the process and provided insights on how to tune the operating parameters.

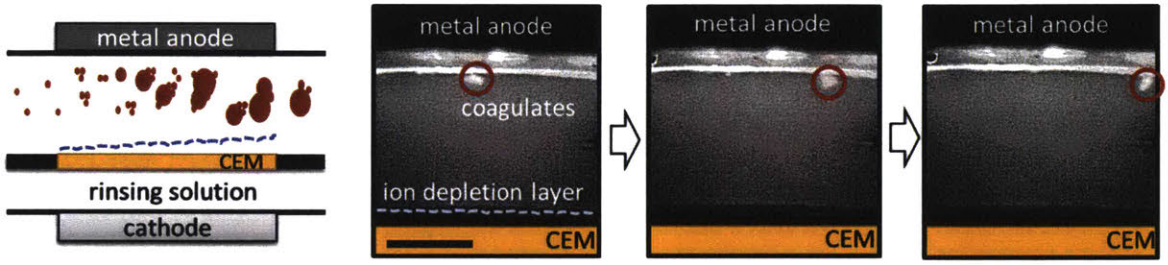

Figure 5.3 Visualization of EC-ICP hybrid. The hybrid system was visualized using fluorescence microscopy. For ease of visualization, the system was simplified to a single cell, consisting of a metal (Aluminum) electrode and a CEM on each side of the cell. A coagulate layer in white and a dark depletion layer are shown near the surface of the anode and on the CEM, respectively. The three microscopic images are time-lapsed (tlapse = 0.15sec). The black line on the left side of CEM in the first image represents a scale bar (1mm). The feed solution consisted of 10,000 mg/L silica particles in 10 mM NaCl. The various components in the schematic represent the same components as defined in Figure 5.1. The EC channel dimensions were 2mm width, 200μm depth, and 5mm length. The flowrate was 100μL/min in the EC channel (v_{avg} = 0.25m/min).

5.4 Removal of contaminants by EC

Since our system is the first demonstration of micro-scale EC, we examined its EC performance for the removal of contaminants, namely bacteria (*E. coli*) and suspended solids (silica). *E. coli* is a harmful biological contaminant, which is one of the causes of diarrheal disease, and commonly present in water sources in developing countries, such as India and Bangladesh.[35,36] Silica was used as model suspended solids, which are a common constituent in various water sources. A small amount of silica in water can be tolerated, but a high level of silica affects the taste and physical appearance of water. In the EC experiments, we focused on the EC performance of the microfluidic EC system, and thus a device with no ICP channels was

used (same configuration as device in Figure 5.3). Although there was no desalination, a CEM was inserted to separate the anode reaction, which was utilized for EC, from the cathode reaction.

The *E. coli* removal profile is shown in Figure 5.4a. The removal of *E. coli* increased with an increasing current. In this experiment, the flowrate was kept constant, so the applied current was proportional to the amount of metal coagulant released. In another study, a batch EC was performed to remove *E. coli*, and the removal increased with an increasing EC treatment time at a fixed current.[2] Since the EC treatment time in this study was proportional to the amount of metal coagulant, we can say that our results agree with this previous study in that the bacteria removal increases with an increasing amount of metal coagulant.

The silica removal experiment was conducted at three different salinities, representing various conditions where the EC technology can be used: 10mM (brackish water), 500mM (seawater), and 1.7M (produced water from hydraulic fracturing) of NaCl. The silica removal profile was similar to the *E. coli* removal in that silica removal increases with an increasing current. But silica was completely removed at a much lower current, which could be due to the difference in their inherent characteristics (*i.e.,* zeta potential). A removal profile similar to that in Figure 5.4b had been observed in a previous study with a batch EC.[37] As shown in Figure 5.4b, silica removal at 500mM and 1.7M were similar, with an almost complete removal above 75A/m^2, which was slightly lower than the required current level of 100A/m^2 at 10 mM. At around 100A/m^2, most of silica was removed (~95% removal), and the removal efficiency plateaued. The small portion of silica remaining in water was within the margin of error from the measurement technique.

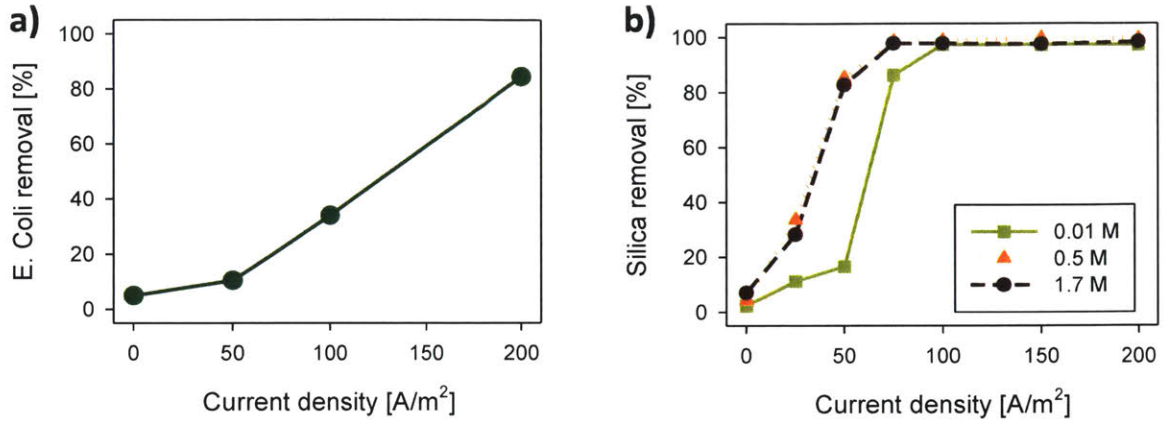

Figure 5.4 Micro-scale electrocoagulation performance. a) Bacteria (*E. Coli*) removal. The bacteria concentration was $6.5x10^8$ cells/mL, and the salinity was 20 mM NaCl. The device used in bacteria EC experiment had EC channel dimensions of 2mm width, 200μm depth, and 5mm length. The product flowrate was 200μL/min (v_{avg} = 1m/min). b) Silica removal at various salinities. The feed solution consisted of 1000 mg/L silica and NaCl at various concentrations. The device used in silica EC experiment had EC channel dimensions of 1mm width, 800μm depth, and 5mm length. The flowrate was 800μL/min in the EC channel (v_{avg} = 1m/min).

5.5 Comparison of voltage drop in ICP and EC-ICP hybrid

Our hybrid system makes use of the unavoidable Faradaic reaction near the anode to remove small particles, while desalting by ICP desalination. Here, we investigated the effect of the additional EC process on the electrical energy of the system. We compared the performance of the same EC-ICP device with different solutions running in the anode channel. When a salt-only solution was run in the anode channel (See Figure 5.5a), no EC occurred because there were no particles to be coagulated. When the anode solution contained silica nanoparticles and has the same salinity as the salt solution (See Figure 5.5b), the silica particles were coagulated by EC. In both cases, the voltage drop of the system at the same current densities was almost the same, which indicated that the addition of EC process to the ICP desalination does not incur any additional energy as shown in Figure 5.5c. Therefore, it can come 'for free' in a given ICP

desalination system, or to be more exact, EC process can be run with the energy already wasted as the integral part of the ICP desalination process (or any other electro-membrane desalination system such as electrodialysis). But, in a long-term operation, if the particles keep accumulating and initiate fouling on the anode, the voltage drop in the device may increase, incurring additional electrical energy consumption. Moreover, the periodic replacement of sacrificial metal anode could also contribute to the additional cost from EC operation. These factors should be considered in further investigation of EC-ICP process.

While the approximate energy consumption of a basic EC unit without CEM (See Figure 5.1a) is experimentally calculated to be 0.01-0.2 kWh/m^3 for pretreatment, EC-ICP hybrid system does not have to require this additional energy consumption for EC operation. Since the dominant energy consumption in the EC-ICP hybrid occurs in the desalination process (*e.g.*, resistance of the desalted stream and the CEM itself) as shown in Figure 5.5c, one can consider the energy consumption of ICP desalination as an estimation of energy consumption in the EC-ICP hybrid.

Our group has already examined the energy consumption in ICP desalination with a wide range of feed salinity from brackish to hypersaline brine feed water (10mM to 1.7M NaCl solution) in the previous works.[25–27] Based on the previous studies, ICP desalination requires 1-2 kWh/m^3 for brackish feed water treatment (10-20mM NaCl solution), and these energy values are comparable to those in similar water treatment studies in literature: 0.05-0.27 kWh/m^3 for silica removal by EC[38] and 0.6-2kWh/m^3 for brackish water desalination by electrodialysis.[30,39,40]

However, it has to be mentioned that energy consumption of the EC-ICP hybrid can be varied depending on the system configuration (*e.g.*, number of CEMs, channel dimensions, more importantly, flowrates, or production rates, as well as current used). In a practical electrodialysis system, 200 to 1000 ion exchange membranes are installed in parallel to form a complete electrodialysis stack mainly for reduction of energy consumption.[41] In other words, EC-ICP hybrid with a single ICP cell (Figure 5.5b) would have the highest energy consumption since two CEMs are used only for one desalting stream, whereas the average number of CEMs in an industrial-scale system would be nearly one.

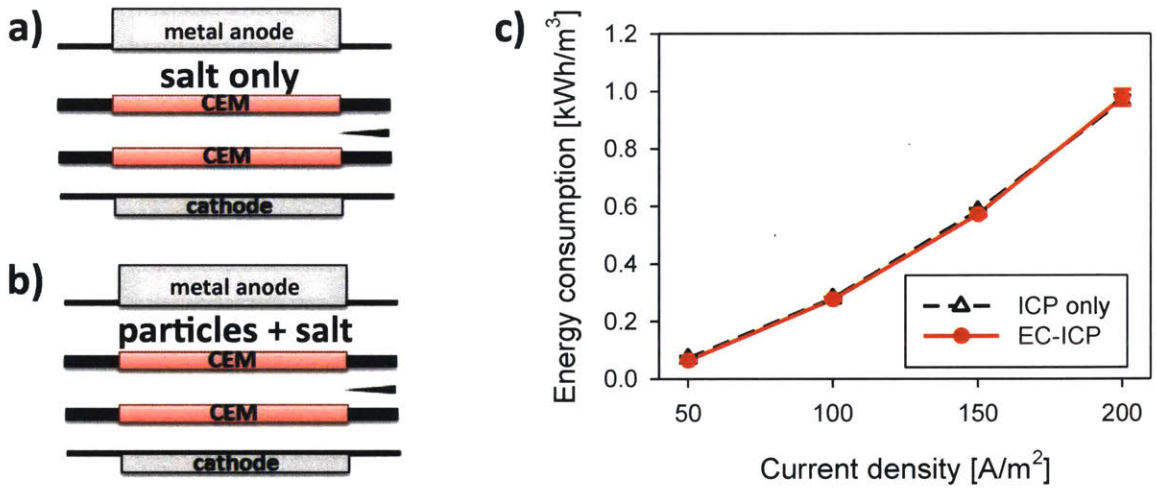

Figure 5.5 Energy comparison between ICP desalination and EC-ICP. The two processes were run on the same device at the same conditions, but with different solutions in anode rinsing channel: a) salt-only solution in ICP desalination, and b) silica particles and salt solution in EC-ICP). Salinity in all experiments was 10mM NaCl, and the silica concentration in silica-containing solution was 1000 mg/L. c) Electrical energy consumption as a function of current density. The y-axis represents the average voltage drop, and the error bars represent the standard deviation over the measurement period. The dimensions of the EC channel were 1mm width, 800μm depth, and 5mm length; the dimensions of the ICP channels were 1.5mm width, 800μm depth, and 5mm length. The flowrates were 800μL/min in the EC channel and 300μL/min in each ICP channel (v_{avg} = 1m/min in EC; v_{avg} = 0.25m/min in ICP)

5.6 Continuous, multi-cell EC-ICP system for removal of particles and salts

As described in System description, the multi-cell EC-ICP system (Figure 5.1c) enhances the quality and throughput of the treated water. In the continuous multi-cell EC-ICP operation with three ICP channels, shown in Figure 5.6, the feed water was first treated with EC, where the non-salt particles were removed from the solution; the product of EC, which contained mostly salt ions, was then treated by ICP desalination. In designing of the EC-ICP device, the given conditions were feed flowrate, feed salinity, and target salinity of product. For a given flowrate, the current was set to achieve a complete removal of the suspended solids, and the flowrate of each ICP cell was determined to achieve the desired salinity of the product stream. The number of the ICP cells can be determined to accommodate the entire solution. In this proof-of-concept experiment, we chose silica to model suspended solids in 20mM NaCl, which is in brackish range. As shown in Figure 5.6b, with enough current applied, most of silica particles (>95%) were removed, and the salinity of the product water was brought down to a drinkable level (<500ppm total dissolved solid,[42] corresponding to 8.6mM NaCl). Through this experiment, we demonstrated that our EC-ICP hybrid can successfully remove suspended particles and reduce the salinity to produce clean water. We utilized the inevitable voltage drop in the anode rinsing channel to a useful separation step by adding the EC pretreatment step to the ICP desalination process.

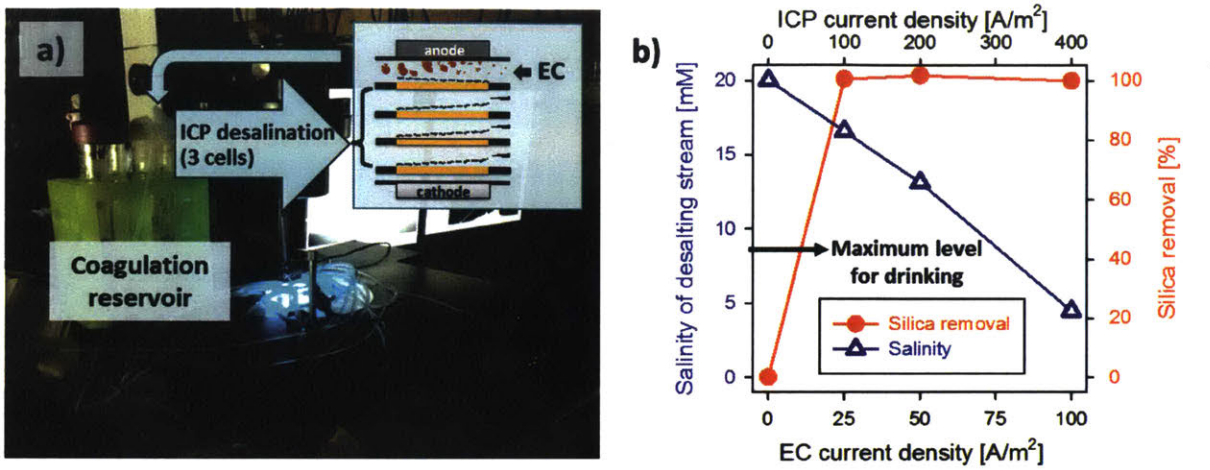

Figure 5.6 Results of EC-ICP hybrid system. The feed to the device consists of 1000 mg/L silica nanoparticles (model suspended solids) and 20 mM sodium chloride. The flowrates in EC and ICP cells are 800μL/min and 75μL/min/cell, respectively (v_{avg} = 1m/min in EC; v_{avg} = 0.25m/min in ICP). The dimensions of the EC channel were 1mm width, 800μm depth, and 20mm length; the dimensions of the ICP channels were 1.5mm width, 200μm depth, and 20mm length. The device had three ICP cells. The recoveries to EC and ICP are ~90% and 50%, respectively. a) Microfluidic setup of the EC-ICP process. The blue-lighted area is the location of the device. The process was monitored using a microscope through the computer screen. After EC process, the solution goes through the coagulation reservoir, where the coagulates form and settle and the supernatant is fed to the ICP channels. b) Analysis of final product.

5.7 Conclusion

In this study, we developed an electrocoagulation – ion concentration polarization desalination hybrid system that integrates desalination and its pretreatment into a single device and demonstrated its operation in a microfluidic device. This microfluidic EC-ICP platform is, to our knowledge, the first demonstration of electrocoagulation in micro-scale. The microfluidic system enables us to visualize the EC process in small scale and facilitates a systematic optimization of various parameters. By combining two different electrochemical processes in the same system, we may eliminate unnecessary voltage drop and achieve both seamless integration and energy efficiency enhancement. We showed that our system can effectively remove colloidal particles, such as suspended solids and bacteria, and salt content. More importantly, our hybrid

system is flexible because it can treat a wide range of wastewater with various particles and salt by simply adjusting the operating parameters and it is scalable owing to its modular design. From this, we can see that our system can find many applications, especially where a small footprint is advantageous, including disaster relief, military uses, and river water treatment for domestic water usage in developing countries.

5.8 References

[1] I. Sutzkover-Gutman, D. Hasson, Feed water pretreatment for desalination plants, Desalination. 264 (2010) 289–296. doi:10.1016/j.desal.2010.07.014.

[2] D. Ghernaout, A. Badis, A. Kellil, B. Ghernaout, Application of electrocoagulation in Escherichia coli culture and two surface waters, Desalination. 219 (2008) 118–125. doi:10.1016/j.desal.2007.05.010.

[3] C. Delaire, C.M. van Genuchten, K.L. Nelson, S.E. Amrose, A.J. Gadgil, *Escherichia coli* Attenuation by Fe Electrocoagulation in Synthetic Bengal Groundwater: Effect of pH and Natural Organic Matter, Environ. Sci. Technol. 49 (2015) 9945–9953. doi:10.1021/acs.est.5b01696.

[4] B. Zhu, D.A. Clifford, S. Chellam, Comparison of electrocoagulation and chemical coagulation pretreatment for enhanced virus removal using microfiltration membranes, Water Res. 39 (2005) 3098–3108. doi:10.1016/j.watres.2005.05.020.

[5] C.T. Tanneru, J.D. Rimer, S. Chellam, Sweep Flocculation and Adsorption of Viruses on Aluminum Flocs during Electrochemical Treatment Prior to Surface Water Microfiltration, Environ. Sci. Technol. 47 (2013) 4612–4618. doi:10.1021/es400291e.

[6] W. Den, C. Huang, H.-C. Ke, Mechanistic Study on the Continuous Flow Electrocoagulation of Silica Nanoparticles from Polishing Wastewater, Ind. Eng. Chem. Res. 45 (2006) 3644–3651. doi:10.1021/ie0514410.

[7] N.S. Abuzaid, A.A. Bukhari, Z.M. Al-Hamouz, Ground water coagulation using soluble stainless steel electrodes, Adv. Environ. Res. 6 (2002) 325–333. doi:10.1016/S1093-0191(01)00065-X.

[8] B. Merzouk, B. Gourich, A. Sekki, K. Madani, M. Chibane, Removal turbidity and separation of heavy metals using electrocoagulation–electroflotation technique: A case study, J. Hazard. Mater. 164 (2009) 215–222. doi:10.1016/j.jhazmat.2008.07.144.

[9] A. Neumann, R. Kaegi, A. Voegelin, A. Hussam, A.K.M. Munir, S.J. Hug, Arsenic Removal with Composite Iron Matrix Filters in Bangladesh: A Field and Laboratory Study, Environ. Sci. Technol. 47 (2013) 4544–4554. doi:10.1021/es305176x.

[10] L. Li, C.M. van Genuchten, S.E.A. Addy, J. Yao, N. Gao, A.J. Gadgil, Modeling As(III) Oxidation and Removal with Iron Electrocoagulation in Groundwater, Environ. Sci. Technol. 46 (2012) 12038–12045. doi:10.1021/es302456b.

[11] M. Tong, S. Yuan, P. Zhang, P. Liao, A.N. Alshawabkeh, X. Xie, Y. Wang, Electrochemically Induced Oxidative Precipitation of Fe(II) for As(III) Oxidation and Removal in Synthetic Groundwater, Environ. Sci. Technol. 48 (2014) 5145–5153. doi:10.1021/es500409m.

[12] P. Cañizares, F. Martínez, C. Jiménez, J. Lobato, M.A. Rodrigo, Coagulation and Electrocoagulation of Wastes Polluted with Dyes, Environ. Sci. Technol. 40 (2006) 6418–6424. doi:10.1021/es0608390.

[13] S. Zodi, O. Potier, F. Lapicque, J.-P. Leclerc, Treatment of the industrial wastewaters by electrocoagulation: Optimization of coupled electrochemical and sedimentation processes, Desalination. 261 (2010) 186–190. doi:10.1016/j.desal.2010.04.024.

[14] C. Phalakornkule, P. Sukkasem, C. Mutchimsattha, Hydrogen recovery from the electrocoagulation treatment of dye-containing wastewater, Int. J. Hydrogen Energy. 35 (2010) 10934–10943. doi:10.1016/j.ijhydene.2010.06.100.

[15] P. Durango-Usuga, F. Guzmán-Duque, R. Mosteo, M. V. Vazquez, G. Peñuela, R.A.

Torres-Palma, Experimental design approach applied to the elimination of crystal violet in water by electrocoagulation with Fe or Al electrodes., J. Hazard. Mater. 179 (2010) 120–6. doi:10.1016/j.jhazmat.2010.02.067.

[16] E.-S.Z. el-Ashtoukhy, N.K. Amin, Removal of acid green dye 50 from wastewater by anodic oxidation and electrocoagulation--a comparative study., J. Hazard. Mater. 179 (2010) 113–9. doi:10.1016/j.jhazmat.2010.02.066.

[17] J.B. Parsa, H.R. Vahidian, a. R. Soleymani, M. Abbasi, Removal of Acid Brown 14 in aqueous media by electrocoagulation: Optimization parameters and minimizing of energy consumption, Desalination. 278 (2011) 295–302. doi:10.1016/j.desal.2011.05.040.

[18] N. Biswas, G. Lazarescu, Removal of oil from emulsions using electrocoagulation, Int. J. Environ. Stud. 38 (1991) 65–75. doi:10.1080/00207239108710650.

[19] Ü.B. Öğütveren, S. Koparal, Electrocoagulation for oil-water emulsion treatment, J. Environ. Sci. Heal. . Part A Environ. Sci. Eng. Toxicol. 32 (1997) 2507–2520. doi:10.1080/10934529709376699.

[20] C.Y. Hu, S.L. Lo, W.H. Kuan, Effects of the molar ratio of hydroxide and fluoride to Al(III) on fluoride removal by coagulation and electrocoagulation., J. Colloid Interface Sci. 283 (2005) 472–6. doi:10.1016/j.jcis.2004.09.045.

[21] N. Mameri, A.R. Yeddou, H. Lounici, D. Belhocine, H. Grib, B. Bariou, Defluoridation of septentrional Sahara water of north Africa by electrocoagulation process using bipolar aluminium electrodes, Water Res. 32 (1998) 1604–1612. doi:10.1016/S0043-1354(97)00357-6.

[22] P.K. Holt, G.W. Barton, C. a Mitchell, The future for electrocoagulation as a localised water treatment technology., Chemosphere. 59 (2005) 355–67. doi:10.1016/j.chemosphere.2004.10.023.

[23] C.T. Tanneru, J. N., V.R. Hill, S. Chellam, Relative Insignificance of Virus Inactivation during Aluminum Electrocoagulation of Saline Waters, Environ. Sci. Technol. 48 (2014) 14590–14598. doi:10.1021/es504381f.

[24] T.C. Timmes, H.-C. Kim, B.A. Dempsey, Electrocoagulation pretreatment of seawater prior to ultrafiltration: Pilot-scale applications for military water purification systems, Desalination. 250 (2010) 6–13. doi:10.1016/j.desal.2009.03.021.

[25] R. Kwak, V.S. Pham, B. Kim, L. Chen, J. Han, Enhanced Salt Removal by Unipolar Ion Conduction in Ion Concentration Polarization Desalination., Sci. Rep. 6 (2016) 25349. doi:10.1038/srep25349.

[26] B. Kim, R. Kwak, H.J. Kwon, V.S. Pham, M. Kim, B. Al-Anzi, G. Lim, J. Han, Purification of High Salinity Brine by Multi-Stage Ion Concentration Polarization Desalination., Sci. Rep. 6 (2016) 31850. doi:10.1038/srep31850.

[27] B. Kim, H. Kwon, S.H. Ko, G. Lim, J. Han, Partial desalination of hypersaline brine by lab-scale ion concentration polarization device, Desalination. 412 (2017) 20–31. doi:10.1016/j.desal.2017.02.018.

[28] R. Kwak, V.S. Pham, B. Kim, L. Chen, J. Han, Enhanced Salt Removal by Unipolar Ion Conduction in Ion Concentration Polarization Desalination., Sci. Rep. 6 (2016) 25349. doi:10.1038/srep25349.

[29] C. Charcosset, A review of membrane processes and renewable energies for desalination, Desalination. 245 (2009) 214–231. doi:10.1016/j.desal.2008.06.020.

[30] N.C. Wright, A.G. Winter, Justification for community-scale photovoltaic-powered electrodialysis desalination systems for inland rural villages in India, Desalination. 352

(2014) 82–91. doi:10.1016/j.desal.2014.07.035.
[31] R. Kwak, G. Guan, W.K. Peng, J. Han, Microscale electrodialysis: Concentration profiling and vortex visualization, Desalination. 308 (2013) 138–146. doi:10.1016/j.desal.2012.07.017.
[32] B. Kim, S. Choi, V.S. Pham, R. Kwak, J. Han, Energy efficiency enhancement of electromembrane desalination systems by local flow redistribution optimized for the asymmetry of cation/anion diffusivity, J. Memb. Sci. 524 (2017) 280–287. doi:10.1016/j.memsci.2016.11.046.
[33] J.E. Berlier, A. Rothe, G. Buller, J. Bradford, D.R. Gray, B.J. Filanoski, W.G. Telford, S. Yue, J. Liu, C.-Y. Cheung, W. Chang, J.D. Hirsch, J.M. Beechem Rosaria P. Haugland, R.P. Haugland, Quantitative Comparison of Long-wavelength Alexa Fluor Dyes to Cy Dyes: Fluorescence of the Dyes and Their Bioconjugates, J. Histochem. Cytochem. 51 (2003) 1699–1712. doi:10.1177/002215540305101214.
[34] American Public Health Association., American Water Works Association., Water Environment Federation., Standard methods for the examination of water and wastewater., 22nd ed., American Public Health Association, 2012.
[35] A.S. Ferguson, A.C. Layton, B.J. Mailloux, P.J. Culligan, D.E. Williams, A.E. Smartt, G.S. Sayler, J. Feighery, L.D. McKay, P.S.K. Knappett, E. Alexandrova, T. Arbit, M. Emch, V. Escamilla, K.M. Ahmed, M.J. Alam, P.K. Streatfield, M. Yunus, A. van Geen, Comparison of fecal indicators with pathogenic bacteria and rotavirus in groundwater, Sci. Total Environ. 431 (2012) 314–322. doi:10.1016/j.scitotenv.2012.05.060.
[36] Status of Water Quality in India 2011, 2011.
[37] W. Den, C. Huang, H.-C. Ke, Mechanistic Study on the Continuous Flow Electrocoagulation of Silica Nanoparticles from Polishing Wastewater, Ind. Eng. Chem. Res. 45 (2006) 3644–3651. doi:10.1021/ie0514410.
[38] Z. Liao, Z. Gu, M.C. Schulz, J.R. Davis, J.C. Baygents, J. Farrell, Treatment of cooling tower blowdown water containing silica, calcium and magnesium by electrocoagulation, Water Sci. Technol. 60 (2009) 2345–2352.
[39] J.M. Ortiz, E. Expósito, F. Gallud, V. García-García, V. Montiel, A. Aldaz, Desalination of underground brackish waters using an electrodialysis system powered directly by photovoltaic energy, Sol. Energy Mater. Sol. Cells. 92 (2008) 1677–1688. doi:10.1016/j.solmat.2008.07.020.
[40] F. Valero, A. Barcelo, R. Arbos, Electrodialysis Technology - Theory and Applications, in: Desalination, Trends Technol., InTech, 2011: pp. 3–22. doi:10.5772/14297.
[41] H. Strathmann, Ion-Exchange Membrane Separation Processes (Google eBook), Elsevier, 2004. http://books.google.com/books?hl=en&lr=&id=pcNF7HWbFPIC&pgis=1 (accessed April 20, 2014).
[42] US EPA, Secondary Drinking Water Standards: Guidance for Nuisance Chemicals, n.d. https://www.epa.gov/dwstandardsregulations/secondary-drinking-water-standards-guidance-nuisance-chemicals#table (accessed May 7, 2017).

6. SUMMARY AND FUTURE WORK

6.1 Thesis Summary

In this thesis, the overarching goal was to expand the applications of electromembrane desalination through engineering based on microfluidic experiments and numerical modeling. Specifically, the study focused on three aspects: (1) improving electrodialysis performance for brackish water desalination by optimizing the design of structures, commonly known as spacers, to reduce concentration polarization effect and enhance mass transport; (2) evaluating techno-economic feasibility of ICP desalination for high salinity brine treatment, for which electromembrane desalination is conventionally considered to be inefficient, and which does not currently have a sustainable solution; (3) developing a total water purification system, namely EC-ICP hybrid, that integrate pretreatment and desalination into a single electrochemical device by utilizing the unavoidable, otherwise wasted Faradaic reaction on the anode to a useful work of particle removal.

In Chapter 2, we demonstrated that the mass transport in electromembrane systems can be enhanced by increasing the local flow velocity in the concentration polarization region. Using a microfluidic ED platform, we modulated the local flow near the membranes (AEM or CEM) by placing a row of post structures with a varying distance to the membrane (d'), which results in a redistribution of the hydrodynamic resistance inside the diluate channel. Our study is differentiated from previous efforts for ED spacers in that our study reveals that ion transport can be enhanced or reduced not only by an average flow velocity, but also by an asymmetric distribution of flow velocity inside a diluate channel. When the electrolyte is composed of sodium chloride, which is the major constituent of natural saline water, it is known that the thickness of CP boundary near the membranes (AEM or CEM) should be differentiated by the

relative difference of co-ion diffusivities (D_{Na+} =1.33x10^{-9}m^2/s: co-ion on the AEM side, D_{Cl-} =2.03x10^{-9}m^2/s: co-ion on the CEM side). We found that the maximum mass transport enhancement occurs when the CP boundary layer thickness from AEM and CEM are comparable, which, for sodium chloride solution, occurs when the local flow velocity is slightly higher on the CEM side than on the AEM side. As a result, the optimal mass transport in an electromembrane system with sodium chloride feed can be obtained when the post structures are placed slightly closer to the AEM than to the CEM. By optimizing the position of the post structures in our experimental and numerical studies, the electrical energy was enhanced up to 30 – 40%, while the effect of increased hydrodynamic resistance to the total energy was negligible. The findings from the experiments and the numerical modeling support this previously unexplored effect of asymmetric diffusivity. The concentration and flow profiling through the simulation was used to corroborate the reasoning. Because asymmetry of cation/anion diffusivity is a property of ions in the solution and independent of flow characteristics, the diffusivity-based engineering of the structures can be applied to designing of conventional spacers and mixing promoters in a system with a higher flow. Our work employed electrodialysis as a model system, but the findings from this study is pertinent to a larger field of study in many other electromembrane systems, such as reverse electrodialysis and (membrane) capacitive deionization.

In Chapter 3, we continued the parametric study of the structures (or spacer) in ED with the numerical modeling tools for systematic optimization of the structure design. We selected two parameters for the study: the horizontal location (partial implementation) and the size of the cylindrical posts. First, the partial post study was conducted to find whether posts at specific locations (along the channel length) enhance the mass transport more efficiently than those

placed in other locations. The results show that difference between various locations is minimal, and in general the extent of current enhancement is proportional to the post coverage. The current distributions along the channel length revealed that the peaks of the local current for the channel with structures coincide with the location of the posts as the posts suppress the depletion boundary layer, reduce the electrical resistance, and thus enhance the local mass transport. In the second parameter study, the diameter of cylindrical posts was optimized for minimum energy consumption. The structures (or spacers) modulate, and often enhance, the degree of mass transport by modifying the local flow and ion concentration profiles; as a result, they reduce the electrical energy to achieve the same salt removal. On the other hand, structures inside the channel create additional fluidic resistance and thus increase the pumping energy required for a given flowrate. We showed that larger posts result in a greater current enhancement by creating a faster flow near the membranes and further suppressing the depletion boundary layer. However, the larger posts also create more fluidic resistance, evidenced by the higher pressure drop. In order to quantify the effects on mass transport and fluidic resistance, the electrical ($EPIR_e$) and pumping ($EPIR_p$) energy per each ion removal was calculated. The total energy per ion removal ($EPIR_{total}$), which can be obtained by summing these two energy terms, is used to find the optimal post size. In general, as the post diameter increases, the maximum achievable salt removal increases before reaching a sharp energy increase. However, for very large posts (D = 0.75 - 0.9), both electrical energy and total energy is worsened due to shadow effect and large pumping power. Therefore, the optimal post size should be around D = 50% - 75% of the channel width, depending on the target salt removal.

In Chapter 4, we utilized a set of experimental data from a medium throughput ICP desalination device to build a model that estimates the electrical energy consumption in ICP

desalination at high salinity. Based on the energy model and the experimental data, the operating and the capital cost were calculated, and the water cost was optimized for a fixed feed and product salinity. This method of water cost calculation was applied to evaluate techno-economic feasibility of ICP desalination for two potential applications in high salinity brine management. The first application was partial desalination to seawater salinity (35,000 ppm) so that the product can be treated by seawater reverse osmosis. The cost analysis showed that the ICP partial desalination cost with feed salinity of 75,000 ppm was comparable to an electrodialysis performance at similar feed and product salinity. This cost is much lower than the complete desalination by MVR, a current desalination method for produced water. Combined with seawater RO, partial desalination by ICP desalination can become an economically competitive option for high salinity brine desalination. The cost analysis of ICP-RO hybrid shows that for the feed salinity range, at which RO is technically available, the ICP-RO hybrid is not economically feasible, but it may be more promising for the feed concentration above the limit of RO. The second application was concentration of brine (to 200,000 ppm), by multi-stage ICP process, for salt production. We found that an optimal two-stage system resulted in the water cost of $117/ton salt produced, which is about twice the cost of brine concentration by ED. The high ICP cost can be contributed to the large volume of treatment required in early stages due to the ICP recovery limit of 50% per stage.

In Chapter 5, we incorporated electrocoagulation, a water treatment technology for removal of non-ionic contaminants, into an ICP desalination system by replacing the anode with a sacrificial metal anode and created an EC-ICP hybrid system that can address virtually all type of contaminants in water. In EC-ICP hybrid, the feed water is first treated with EC, where small, colloidal particles are removed from the solution; the product of EC, which contains mostly salt

ions, is then desalinated by ICP desalination. In the proof-of-concept experiment, a synthetic solution containing silica, which models suspended solids, with brackish water salinity (20mM sodium chloride) was treated in a microfluidic EC-ICP device. The recovery of clean water was 45% of the initial feed. The results showed that silica removal was >99% and the product salinity was reduced to a drinking level (500ppm) with an appropriate current density. This microfluidic EC-ICP platform is, to our knowledge, the first demonstration of electrocoagulation in micro scale. The microfluidic system enables us to visualize the EC process in small scale and facilitates a systematic optimization of various parameters. By combining two different electrochemical processes in the same system, we may eliminate unnecessary voltage drop and achieve both seamless integration and energy efficiency enhancement. We showed that our system can effectively remove colloidal particles, such as suspended solids and bacteria (results in a previous report), and salt content. More importantly, this hybrid system is flexible because it can treat a wide range of wastewater with various particles and salt by simply adjusting the operating parameters. From this, we can see that our system can be used in many applications, including river water treatment for domestic water usage in developing countries and further water treatment for irrigation.

6.2 Future Research Directions

In this thesis, we endeavored to achieve improvements in several aspects of electromembrane desalination through experiments on microfluidic platforms and numerical modeling. Our study has demonstrated that with appropriate engineering, electromembrane desalination can become more energy efficient in brackish water desalination and may be economically viable for high salinity brine treatment. For electromembrane desalination to have such competitiveness in desalination industry, continuous efforts for engineering will be needed.

In the first topic of spacer engineering in electrodialysis, the current study was done in microfluidic platform with a low Reynolds number, compared to the flow regime of the commercial ED systems. The effect of the studied parameters (*i.e.*, relative distance between structures and membranes, size of cylindrical structure, location of partially implemented spacers) in a system with high Reynolds numbers, matching the commercial ED Reynolds number, can be a subject of future studies. Moreover, our microfluidic platform with shallow channels (channel depth = $O(10^{-1}mm)$) may show different fluidic behavior from the commercial, large-scale systems (channel depth = $O(10^{1}mm)$) due to the increased interaction with the channel walls. Therefore, the implementation of the optimized parameters in a scaled-up device should follow to validate the applicability of our findings to a large-scale system. Another direction of further study is to construct a nondimensionalized relation among the spacer parameters, channel dimensions, flow property, and current that can generalize the findings to all ED systems.

In the second topic of ICP desalination for high salinity applications, two main improvements should be made for the technology to demonstrate its competitiveness. The first is further engineering of ICP desalination at system level. As discussed in Chapter 4, the main source of increased ICP desalination cost is that the recovery is limited 50% at each stage. Due to this recovery limit, a large feed volume is required to achieve a target throughput for multi-stage ICP process. To reduce the ICP desalination cost for a multi-stage process, *e.g.*, brine concentration, the salt retention in the concentrate stream should be enhanced. An example of a potential solution would be to recycle the diluate stream from later stages, which contain a high concentration of salt. The other direction for further study is more detailed economic analysis. The current cost analysis is based on the two main cost drivers: electrical energy consumption

and required membrane area. To enhance the accuracy of the water cost, other costs, such as pretreatment, transportation, and concentrate disposal should be accounted. In order to estimate the cost contribution from these various processes, a pilot scale system may be required.

In the development of the EC-ICP hybrid, the ultimate goal is to build a portable, continuous device that does not require human intervention. The current device involves a coagulation tank that operates in a semi-batch mode and requires periodic disposal of coagulates between EC pretreatment and ICP desalination steps. Development of a continuous coagulate separation process will enable a completely automatic operation, and packaging the whole system, including the pumping and power supply as well as the EC-ICP devise, into a single box can make the system portable. Furthermore, EC-ICP operation with a renewable energy source should be pursued to demonstrate its feasibility as a localized water treatment technology for remote areas that lack on-grid water and energy resources.